AD-777 817

STUDY OF ELECTRONIC TRANSPORT AND BREAKDOWN IN THIN INSULATING FILMS

Murray A. Lampert, et al

Princeton University

Prepared for:

Air Force Cambridge Research Laboratories
Advanced Research Projects Agency

July 1973

DISTRIBUTED BY:

NTIS

National Technical Information Service
U. S. DEPARTMENT OF COMMERCE
5285 Port Royal Road, Springfield Va. 22151

ARPA Order No. 2180

Program Code No. 4D10

Contractor: Princeton University

Effective date of contract: 1 July 1972

Contract No. F19628-72-C-0298

Principal Investigator and phone no.
Prof. Walter C. Johnson/609 452-4621

AFCRL Project Scientist and phone no.
Dr. John C. Garth/617 861-4051

Contract expiration date: 30 June 1975

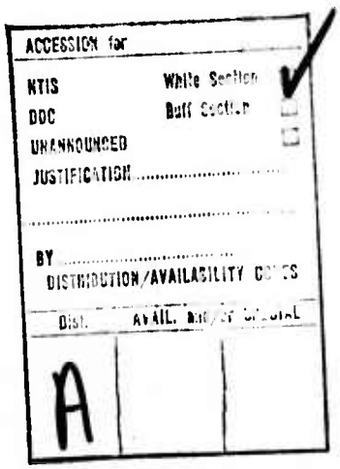

Qualified requestors may obtain additional copies from the Defense Documentation Center. All others should apply to the National Technical Information Service.

ic

Unclassified

Security Classification

AD 777 817

DOCUMENT CONTROL DATA - R & D

(Security classification of title, body of abstract and indexing annotation must be entered when the overall report is classified)

1. ORIGINATING ACTIVITY *(Corporate author)*

Princeton University
Department of Electrical Engineering
Princeton, New Jersey 08540

2a. REPORT SECURITY CLASSIFICATION

Unclassified

2b. GROUP

3. REPORT TITLE

STUDY OF ELECTRONIC TRANSPORT AND BREAKDOWN IN THIN INSULATING FILMS

4. DESCRIPTIVE NOTES *(Type of report and inclusive dates)*

Scientific. Interim.

5. AUTHOR(S) *(First name, middle initial, last name)*

Murray A. Lampert
Walter C. Johnson
Wilmer R. Bottoms

6. REPORT DATE

July 1973

7a. TOTAL NO. OF PAGES

~~125~~ 127

7b. NO. OF REFS

29

8a. CONTRACT OR GRANT NO.

F19628-72-C-0298 ARPA Order No. 2180

b. PROJECT NO.

Project Task, Work Unit Nos.
2180 n/a n/a

c. DoD Element 61101D

d. DoD Subelement n/a

9a. ORIGINATOR'S REPORT NUMBER(S)

PU-DPL-Tech. Rpt. No. 26

Semi-Annual Technical Report No. 2

9b. OTHER REPORT NO(S) *(Any other numbers that may be assigned this report)*

AFCRL-TR-74-0076

10. DISTRIBUTION STATEMENT

A - Approved for public release; distribution unlimited

Reproduced by
NATIONAL TECHNICAL
INFORMATION SERVICE
U S Department of Commerce
Springfield VA 22151

11. SUPPLEMENTARY NOTES

This research was sponsored by the Defense Advanced Research Projects Agency

12. SPONSORING MILITARY ACTIVITY

Air Force Cambridge Research Laboratories (LQ)
L.G. Hanscom Field
Bedford, Massachusetts 01730

13. ABSTRACT

Progress is reported in the characterization of electronic transport and dielectric breakdown properties of technologically important, thin insulating films on Si, namely SiO_2, Al_2O_3, Si_3N_4 and their composites.

New corona-charging techniques have been developed for the study of non-destructive breakdown of un-metallized SiO_2 films, enabling the measurement of I-V characteristics in the steady-state discharge, the identification of the current-carrier in the oxide, an accurate study of electron tunneling from the Si substrate, and producing strong evidence against avalanching in the oxide.

Locally destructive, self-quenching breakdown of Au-Al_2O_3-Si and Al-SiO_2-Si structures has been studied. The time scale for breakdown is hundreds of nanoseconds for the Si in inversion, and tens of nanoseconds in accumulation. Pre-breakdown C-V (charge storage) measurements suggest breakdown of the Al_2O_3 structure at the Si interface, and of the SiO_2 structure at the Al interface. A silicon-oxide interface under a thin film has been successfully probed in the SEM with high lateral resolution.

Strong electron-trapping in Al-implanted SiO_2 films has been verified by charge-discharge techniques, using optical charging and optical or thermal discharging, and has been successfully modelled theoretically. C-V measurements have confirmed strong electron-trapping in SiO_2 films previously exposed to kilovolt electron-beam injection.

Theoretical modeling of self-quenching breakdown is under study with tunneling, joule-heating and their interaction (feedback) as the key ingredients. The dynamical behavior of runaway, hot-electron distributions has been extensively studied by graphical and computer techniques.

DD FORM 1 NOV 68 1473 (PAGE 1)

S/N 0102-014-6600

Unclassified

Security Classification

14. KEY WORDS	LINK A		LINK B		LINK C	
	ROLE	WT	ROLE	WT	ROLE	WT
Electronic transport	8	2				
Dielectric breakdown	8	3				
Insulating films	9	3				
Corona charging			10	3		
Nondestructive breakdown			9	3		
Tunneling into oxide			7	2		
Insulator breakdown			8	2		
Self-quenching breakdown					8	3
Scanning electron microscopy					10	2
Electron trapping in silicon dioxide					8	3
Aluminum Implantation into silicon dioxide					10	3
Hot electrons in insulators					8	3

Abstract

Progress is reported in the characterization of electronic transport and dielectric breakdown properties of technologically important, thin insulating films on Si, namely SiO_2, Al_2O_3, Si_3N_4 and their composites.

New corona-charging techniques have been developed for the study of non-destructive breakdown of un-metallized SiO_2 films, enabling the measurement of I-V characteristics in the steady-state, the identification of the current-carrier in the oxide, and the accurate study of electron tunneling from the Si substrate. Evidence is adduced against avalanching in the oxide.

Locally desctructive, self-quenching breakdown of $Au-Al_2O_3-Si$ and $Al-SiO_2-Si$ structures has been studied. The time scale for breakdown is hundreds of nanoseconds for the Si in inversion, and tens of nanoseconds in accumulation. Pre-breakdown C-V (charge storage) measurements suggest breakdown of the Al_2O_3 structure at the Si interface, and of the SiO_2 structure at the Al interface. A silicon-oxide interface under a thin film has been successfully probed in the SEM with high lateral resolution.

Strong electron trapping in Al-implanted SiO_2 films has been verified by charge-discharge techniques, using optical injection of charge carriers into the films for charging of the traps and optical or thermal discharge of the trapped carriers. The trapping has been successfully modeled theoretically.

Theoretical modeling of self-quenching breakdown is under study with tunneling, joule-heating and their interaction (feedback) as the key ingredients. The dynamical behavior of runaway, hot-electron distributions has been extensively studied by graphical and computer techniques.

Table of Contents

	Page
1. Introduction	1
A. Non-Destructive Breakdown	1
B. Locally Destructive, Self-Quenching Breakdown	2
C. Secondary-Electron Spectroscopy	3
D. Charge-Discharge Studies	4
E. Electron-Beam Injection Studies	4
F. Theoretical Modeling of Local Breakdown	5
G. Tunneling Calculations	6
H. Hot-Electron, Monte-Carlo Calculations	6
2. Non-Destructive Breakdown and Transport in Un-Metallized Films	7
A. Background Discussion and Summary	7
B. The Corona Discharge	8
C. The Basic Electronic Processes	9
D. The Basic Experiment	11
E. Steady-State Potential Measurements	13
F. C-V Measurements	16
G. The P-N Junction-Diode Substrate-Detector Experiments	17
H. Preliminary Results with Dry Nitrogen	21
I. Steady-State I-V Characteristics	21
J. Thickness Dependence of the Breakdown Field	24
K. Electron Tunneling Induced by Positive Corona	24
L. Positive Charging Induced by Negative Corona	32
3. Locally Destructive, Self-Quenching Breakdown in MIS Capacitor Structures	39
A. Summary	39
B. The Breakdown Voltage vs Time Behavior for Al_2O_3 Structures	39
C. C-V Measurements and Optical Photomicrography of Al_2O_3 Structures	47
D. The Breakdown Voltage vs Time Behavior for SiO_2 Structures	51
E. C-V Measurements on SiO_2 Structures	51
F. SEM Topographic Studies of SiO_2 Structures	57
4. Electron-Beam Techniques for Probing the Solid-Solid Interface	60
A. Background Discussion	60
B. Differential Detection-Volume Spectroscopy	62
5. Charge-Discharge Studies of Electron-Trapping in Al-Implanted SiO_2	68
A. Background Discussion and Summary	68
B. Experimental Procedure and Results	70
C. Analysis and Numerical Results	74
i) Steady-State Analysis	75
ii) Transient Analysis	78

	Page
6. Electron-Beam Injection and Damage Studies	83
A. Background Discussion	83
B. Charge-Storage Studies: C-V and Internal Photoemission Measurements	85
C. Summary	97
7. Theory of Electron-Tunneling from Si into SiO_2 - Triangular Well Approximation	98
A. Background Discussion	98
B. The Mathematical Calculation	99
C. Application of the Theory	105
8. Monte-Carlo Studies of Hot-Electron Behavior in Insulating Films at High Fields	106
A. Background Discussion	106
B. New Results	106
9. Theoretical Modeling of Local Breakdown	117
References	119

I. Introduction

This report details progress in a comprehensive experimental and theoretical research program for the characterization of electronic transport and dielectric breakdown properties of thin insulating films on silicon which are technologically important (SiO_2, Al_2O_3, Si_3N_4, and their composites).

The experimental approaches being used are:

i) Completely non-destructive breakdown of the insulating film achieved by contacting the exposed surface of the film by a corona discharge in a suitable gas,

ii) locally destructive, self-quenching breakdown of the film, achieved with thin metallization,

iii) optical injection of charge into the film and optical or thermal discharge of trapped carriers in the film,

iv) electron-beam injection of kilovolt electrons stopped inside the film under a thin metallization,

v) elemental analysis and topographic imaging of breakdown-induced damage in the film,

vi) electron-beam studies of the solid-solid interface between the silicon substrate and the film.

The theoretical studies which are being carried out are:

i) Monte-Carlo calculations of hot-electron distributions produced by high electric fields in the film,

ii) modeling studies directed toward identification of those physical mechanisms critical to the electrical breakdown of the film,

iii) tunneling of electrons out of a triangular potential well in the Si, produced by strong band-bending at the interface into the film.

Highlights of the current report are:

A. Non-Destructive Breakdown

In the non-destructive breakdown of SiO_2 films thermally grown on Si, the sign of the current-carrier in the oxide has been determined by use of a shallow P-N junction diode as the substrate. For both positive and negative coronas, electrons

are the current carrier. With negative corona it has been directly verified that each electron entering the silicon from the oxide generates approximately one electron-hole pair in thermalizing to the bottom of the silicon conduction band.

A direct-comparison technique has been developed for measuring the surface potential of the exposed film under steady-state charging by the corona. With this technique it has been shown that there are no significant differences in the I-V characteristics for n-and p-type substrates.

The vibrating Kelvin-probe technique for measuring surface-potential decay rates, after charging, has been developed into an accurate and reliable vehicle for studying tunneling of electrons from Si into SiO_2. This technique yields an electron effective mass in the oxide of $m_n/m = 0.39$, in agreement with previously reported values.

Under negative corona charging, at fields above 1.1×10^7 V/cm, positive charge is found in the oxide through C-V measurements with a mercury probe. Arguments are adduced that the positive charge is the result of injection of hot holes from the Si into the SiO_2, the holes being created by the incoming electron (the primary current-carrier in the oxide).

Two independent experiments negate avalanching in the SiO_2 film as a likely significant factor in local film breakdown. The shallow-junction diode experiment with negative corona establishes that a significant fraction of electrons in the oxide cannot have as much as even 2 ev excess energy. Further, the complete absence of oxide charging with positive corona establishes that a negligible number of electron-hole pairs can have been created in the breakdown.

B. Locally Destructive, Self-Quenching Breakdown

Locally destructive, self-quenching breakdown has now been studied on Au-Al_2O_3-Si and Al-SiO_2-Si structures, where the Al_2O_3 is pyrolytically deposited and the SiO_2 thermally grown. A result common to both structures is an order-of-magnitude difference in the time scales for breakdown between those

situations where the Si substrate is in accumulation at the interface (tens of nanoseconds) and where the substrate is in inversion (hundreds of nanoseconds). The corresponding equivalent resistances in the discharge path are roughly one hundred ohms (Si in accumulation) and a few kilohms (Si in inversion). In the case of Al_2O_3, at high fields at pre-breakdown, positive gate (Au) voltage charges the film negatively and negative gate voltage charges the film positively, as determined by C-V measurements. These results are consistent with breakdown always initiated at the silicon interface. The results for SiO_2 are the opposite: at high fields at pre-breakdown, positive gate (Al) voltage charges the film positively (up to $10^{17}/cm^3$ volume density of charge) and negative gate voltage produces relatively little charging (C-V flat-band shift less than 5 volts). These results are consistent with breakdown always initiated at the Al interface. Electrons are not strongly trapped in a clean SiO_2 film and therefore do not charge up the film, whereas holes are always strongly trapped at the $Si-SiO_2$ interface and therefore charge up the film. With positive gate bias the breakdown was sensitive to scratches on the gate; with negative gate bias it was insensitive. With positive gate bias, optical and SEM photography of the exposed breakdown area revealed it to be round, smooth-edged, with $\sim$ 20μ diameter, and a distinct inner region $\sim$ 0.5μ diameter; further the overall size of the breakdown region appears to be independent of whether the silicon substrate is n-type or p-type. With negative gate bias the exposed breakdown area appears round, rough-edged, with $\sim$ 5-6μ diameter, and a distinct inner region $\sim$ 1.2μ diameter. Only p-type substrates have to-date been studied in this polarity. The exposed area of breakdown has been probed for elemental composition in the SEM using x-ray fluorescence.

C. Secondary-Electron Spectroscopy

With relatively thin films ($\lesssim$ 1000Å thickness) the

SEM has been used to image the silicon-oxide interface. The technique employed sweeps the detection volume through the interface region, comparing the absorbed current images during the sweep. Up to the present, lateral resolution of 200A has been achieved, and depth resolution sufficient to image detail at the interface but remaining to be determined quantitatively.

D. Charge-Discharge Studies

Electron traps in aluminum-implanted SiO_2 films have been studied by electron injection induced by internal photoemission, followed by optical or thermal de-trapping. The optical de-trapping required $h\nu > 4.6$ev. Thermal de-trapping was achieved at temperatures below 350°C. Thermal annealing at 600°C substantially reduced the concentration of electron traps, suggesting that the traps are located at defect centers created by the implantation process. A model of electron trapping has been formulated which illustrates the dynamic features of the trapping process and correctly predicts the time dependence of the flat-band voltage and photocurrent during electron photoinjection; both analytical and numerical calculations have been made. Application of the model to the experimental results indicates that all photoinjected electrons are trapped in the oxide. Also, the analysis yields a numerical value for the centroid of the resulting space-charge distribution.

E. Electron-Beam Injection Studies

A square-law portion of the steady-state I-V characteristic obtained in the electron-beam injection experiment has previously been interpreted in terms of electron-trapping in the oxide in equilibrium with photon de-trapping, the photons being generated by the incident (primary) electron beam in stopping. The presence of electron traps in the electron-bombarded oxide has now been independently confirmed by internal photoemission experiments. C-V measurements have yielded flat-band voltage shifts on the order of 25 volts corresponding to negative charge in the oxide. The electron traps are not present in oxide films

which have not been bombarded by the kilovolt electron beam. Further work will concentrate on obtaining a quantitative picture of the production of traps by the beam. Toward this end, an improved, more uniform beam, available from a tungsten cathode, is under design.

F. Theoretical Modeling of Local Breakdown

On the theoretical side, the major effort has been spent on identifying those physical mechanisms which appear to be basic for electrical breakdown of the films. Two ingredients are essential for any model of breakdown: 1) injection of carriers into the film from the substrate or gate, and 2) joule heating in the film. Generally, models of breakdown attempt also to identify positive feedback mechanisms. In SiO_2, breakdown is certainly initiated by Fowler-Nordheim tunneling into the film from the substrate or gate, though at a later stage thermionic emission may be significant. It is likely that the significant tunneling occurs at sites of irregular structure (deviation from flatness) at the cathode surface where there is field enhancement. A simple statistical model is given for estimating the distribution of protuberance sizes. Current initially flows in filaments in the film inside which there is rapid heating to exceedingly high temperatures. (Because of the small filament radius, radiative transfer of heat out of the filament is insignificant and the filament temperature can get very high.) The spreading resistance of the silicon substrate is an important element in the evolution of the breakdown in that, at some current level, it brakes the runaway in the filament. The fields are high enough ($\gtrsim 1 \times 10^7$ V/cm) that ionic conductivity (e.g., of Na^+ ions) may be appreciable even at room temperature. Feedback mechanisms which have been considered are: 1) thermal runaway in the silicon substrate, which may entirely reverse the braking action of the spreading resistance of the silicon; 2) a thermionic instability in which the thermionic current from the cathode is high enough to sustain the cathode at high temperature, and which provides a

mechanism for substantial radial growth of a filament; 3) growth of a conducting protuberance with consequent increase of the field enhancement which was initially determined, at room temperature, by the pure topography; 4) ion-induced field enhancement following ion motion in the high fields at elevated temperatures. This effect has recently been demonstrated experimentally. It is a very powerful mechanism in lowering the breakdown field. Impact ionization, historically a very popular mechanism in the theoretical literature, is shown to be highly unlikely in large bandgap insulators. This mechanism is also not supported by the available experiments (see A).

G. Tunneling Calculations

Theoretical work has also been done, in support of the non-destructive, corona-induced breakdown experiments, on the problem of tunneling of electrons out of the triangular potential well produced inside the silicon at the $Si-SiO_2$ interface by strong band-bending. This problem, which is an extension of the previously solved problem of space quantization inside the triangular well, also has a complete analytical solution, in terms of Airy functions. The calculations indicate that tunneling is mostly out of the lowest sub-band of energy levels in the well.

H. Hot-Electron, Monte-Carlo Calculations

Some further hot-electron, Monte-Carlo calculations have been carried out with available programs. The scaling law for the constant mean-free-path problem has been more extensively studied for large scattering anisotropies in the one-dimensional random-walk simulation. Also, a more systematic exploration of the distribution runaway associated with energy-dependent mean-free-paths has been carried out. (Only rudimentary results on this problem were available in the previous report.) In terms of a simple graphical analysis we now have a good picture of how the distribution function runs away.

2. Non-Destructive Breakdown and Transport in Un-Metallized Films

(Z. Weinberg collaborating)

A. Background Discussion and Summary

Recent progress has been successful in firmly establishing the corona discharge as a powerful research tool for the study of thin insulating films. This discharge provides a simple means for charging , positively or negatively, the exposed, unmetallized surface of the film. The film is easily charged up to breakdown, which is totally non-destructive because of the absence of lateral conductivity along the film surface. Thus, true steady-state and quasi-steady-state currents can be drawn through the film (the latter if there are slow charging effects in the film). There are several unique advantages to the corona discharge technique: 1) the experiments are done at approximately atmospheric pressure so that the charging of the surface takes place at negligible ion kinetic energies ($\lesssim 1$ ev); thus damage to the film produced by ion kinetic energy[1] is avoided, 2) film breakdown is reached at $\lesssim 1 \times 10^7$ V/cm, corresponding roughly to a surface ion density of $10^{13}/cm^2$. Thus, the effective gate associated with the ion deposition is at most a few percent of one monolayer, and 3) because of the absence of lateral conductivity along the film surface, 'weak' spots play a negligible role in the (non-destructive) breakdown of the film. If the film is metallized, the stored energy in the film capacitor discharges through a 'weak' spot, producing severe local destruction.

The results obtained to-date have established that the non-destructive breakdown of SiO_2 films induced by either positive or negative coronas in dry air is due to the tunneling of electrons from either the silicon (positive corona) or from surface electron traps (negative corona) into the film. This has been established by use of a shallow-junction P-N diode for the substrate. The breakdown field strength of the film is constant over the range of thicknesses studied to-date, namely 600 to 2700Å, and the value of the breakdown field is

6×10^6 V/cm. for positive corona (electrons tunneling from the silicon) and 1.3×10^7 V/cm. for negative corona (electrons tunneling out of surface traps). With the positive corona an unusually accurate study of tunneling from the silicon into the oxide has been possible using a vibrating Kelvin probe to monitor the decaying surface potential (after corona charging). With negative corona, C-V measurements with a mercury probe have established the build-up of positive charge in the oxide near the interface. At present, the available data on this point to the tunneling of hot holes from the silicon, these holes being created by electron-hole pair generation by the incoming electrons during their thermalization (these electrons enter the silicon from the oxide with at least 3 ev kinetic energy).

B. The Corona Discharge

A corona discharge in a gas ambient is produced by field intensification at sharp points or thin wires under application of high voltage. It is a well-known phenomenon in the electric power industry, in that the corona generated around a high-voltage transmission line is an undesirable loss mechanism - in fact, the corona losses determine the upper limit of voltage usable for electric power transmission. More recently the corona discharge has played a more benevolent role in technology; it is a standard component in electro-copying equipment, being used to charge up the photo-sensitive paper. In general, the corona is a convenient source of electrostatic charge in a gas ambient. It has been, and is being, used by R. Williams[2] for the study of SiO_2 films, but not as far-reachingly as in the present work.

Shahin[3] has carried out a mass-spectroscopic analysis of the ionic constituents produced by a corona discharge in room air at various humidities. He found that the dominant ions are the following:

For positive corona,

$(H_2O)_nH^+$	with	$n = 4, 5, 6$
Estimated ionization energy:		3.8, 3.2, 2.6 ev

For negative corona, CO_3^- , with an estimated electron affinity of 3.8 $\pm$ 1 ev.

The above positive ions are far too shallow to inject holes into the valence band of SiO_2, whose maximum lies approximately 10 ev below the vacuum. (Only a handful of positive ions are deep enough to inject holes directly into the valence band of SiO_2; these include He^+,Ar^+,Ne^+,N_2^+, etc.). Likewise, the above negative ions are far too deep to inject electrons into the conduction band of SiO_2, whose minimum lies approximately 1 ev below the vacuum. Thus, ions of either sign can only charge up the surface of the exposed oxide, until non-destructive breakdown sets in. In the terminology of energy bands, these ions constitute surface states lying inside the oxide bandgap. Very high fields, $\gtrsim 5 \times 10^6$ V/cm. are required to allow charge to tunnel from these states into the corresponding band of the oxide.

C. The Basic Electronic Processes

The basic electronic processes by which conduction current can flow through the oxide in the corona experiments are schematically illustrated in Fig. 1(a) and (b). With the corona positive, Fig. 1(a), the silicon substrate will be in electron degeneracy at the interface because of the very high field. Thus, n-type Si will be in heavy accumulation at the interface, and p-type Si will be in deep inversion. Possible injection modes are: 1) electrons tunneling into the oxide conduction band from the degenerate electron gas in the conduction band of the silicon at the interface, 2) electrons tunneling into the oxide conduction band from the valence band of the silicon, or 3) holes tunneling from the positively charged surface states (adsorbed positive ions) at the exposed surface into the valence band of the oxide. At any one field, one of these three injection modes will be dominant. At a higher field another mode may take over. (Note that for the sake of

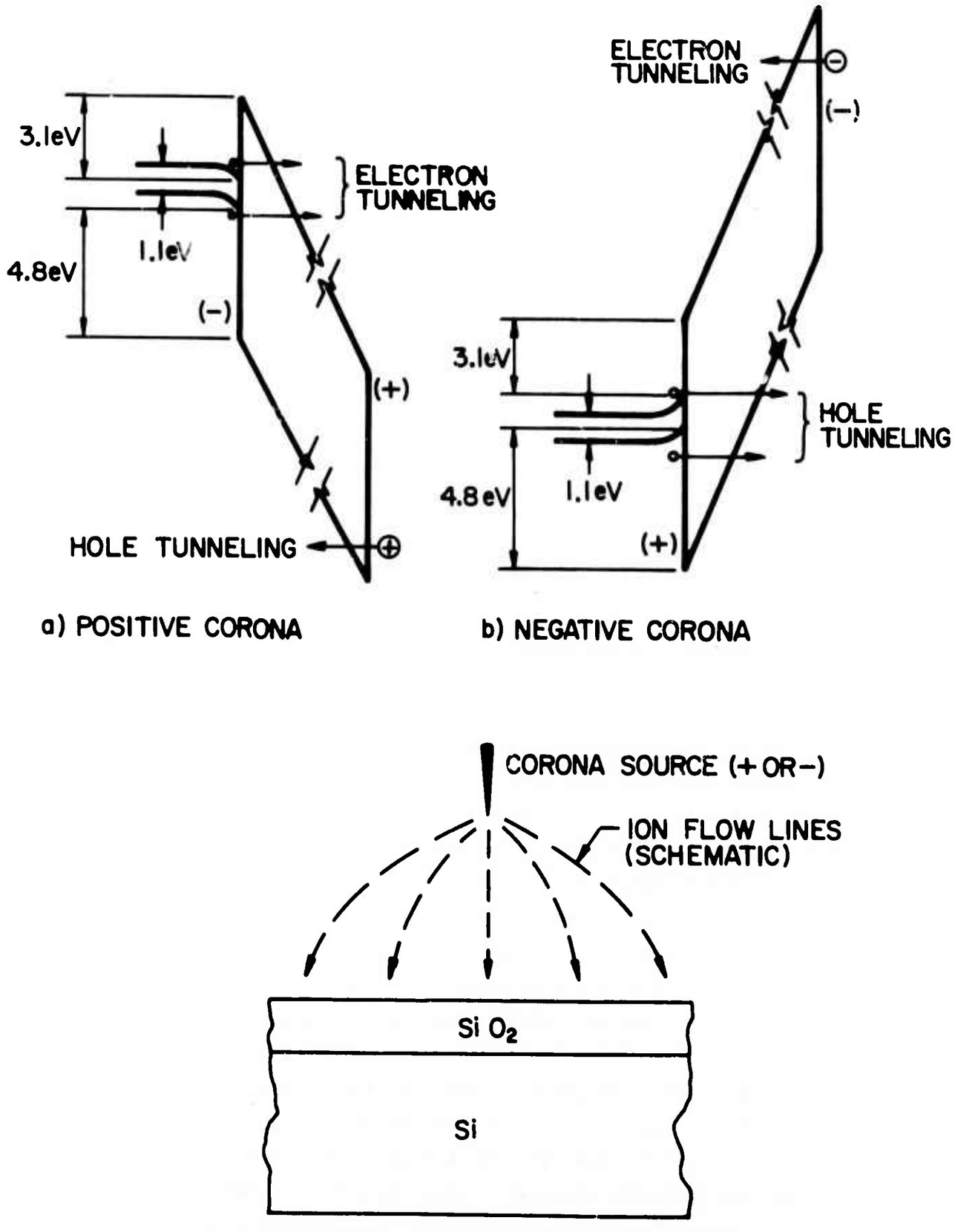

SCHEMATIC DIAGRAMS OF BASIC ELECTRONIC PROCESSES AND EXPERIMENT FIGURE 1

simplicity we have drawn a single energy level of positively charged surface states; in practice there may be several energy levels corresponding to different adsorbed ions, and further, each ' single' level may in fact be somewhat smeared out into a surface band due to various interaction effects. At present very little is known about adsorbed ionic levels on the surface of SiO_2. Figure 1(b), corresponding to negative corona, is the dual of Fig. 1(a). The silicon substrate will now be in hole degeneracy at the interface at the high fields. Hence, p-type Si will be in heavy accumulation and n-type Si in deep inversion at the interface. Holes may tunnel from either the valence band or the conduction band of the silicon, or electrons may tunnel from the negatively charged surface states (adsorbed negative ions).

From Figs. 1(a) and (b) it is clear that, with either polarity of corona, either sign of current-carrier may be dominant. A major result of the present work is, in fact, the determination of the sign of current-carrier - negative, for both polarities, for corona in dry air.

D. The Basic Experiment

A schematic of the basic corona experiment is shown in Fig. 1(c). The ions are produced in the immediate vicinity of the corona needle. The dominant element in the subsequent fate of the ions is their short mean free path λ for collisions with the neutral gas molecules; namely λ is on the order of 10^{-5} cm. at atmospheric pressure. As a result the ions remain thermalized at the ambient temperature, corresponding to a kinetic energy $\simeq$ 0.025 ev. This very low kinetic energy of impacting ions protects the oxide film from undesirable excitations which plague other methods of depositing charge on the film. A further consequence of the strongly collision-dominated motion is that the ions closely follow the electric field lines. This feature has provided the basis for measurement of the surface potential of the film during steady-state charging by the

corona, namely by a comparison method described below.

The corona-induced flux of ions serves as an ideal current-limited source. The exposed film surface serves as a perfect floating electrode which self-adjusts its potential, in the steady state, to accept the ion current which the bulk of the film can transport to the silicon substrate.

In a dry ambient there is negligible lateral conductivity along the exposed surface of the oxide. Thus, 'weak' spots in the film are unable to discharge the electrostatic energy stored throughout the film. Their sole effect is to create a highly localized, very small area of potential deviation from the average potential over the film surface. The total area of potential deviation is obviously proportional to the area of the weak spots; if the latter is small compared to the total exposed film area, the overall effect of the weak spots is correspondingly small. This unusual feature of the corona method is in startling contrast to the conventional MOS capacitor studies, where a single weak spot will lead to locally destructive breakdown, because of the high lateral conductivity of even the thinnest metallization.

The samples studied to-date have all been SiO_2 films thermally grown, in a dry ambient, on (100) wafers of silicon, both n- and p-type in the resistivity range 1-2 Ωcm.
Film thicknesses studied were

p-substrate : 581, 1027, 2570Å
n-substrate : 587, 1000, 2580Å ,

as measured by ellipsometry to an accuracy better than 1%. The index of refraction of the oxides is 1.46. Contact to the back of each wafer was made by Al evaporation following the appropriate shallow-dopant diffusion (boron into p-Si, phosphorus into n-Si) to provide a high-conductivity region of contact. The sample dimensions were 7.5 x 7.5 mm. All of the samples were provided by the RCA Laboratories in Princeton.

All experiments were done in an environmental chamber

which allows control of the gaseous ambient. The chamber is equipped with an air lock for transferring material in and out, and a pair of gloves for exterior manipulation of the interior equipment. The humidity inside the chamber is kept low by circulating the interior ambient through a desiccating system containing both silica-gel and a molecular sieve. The equipment includes provision for introducing a slow, controlled flow of dry N_2 or other gases. The unit can be completely covered to shield the experiment from exposure to ambient light, if necessary.

A schematic of the corona source is shown in Fig. 2. The source of the discharge is a gold plated needle of the type used as a microprobe for integrated circuitry. It proved to be a reliable and stable source, and provided better uniformity of charging over the small sample area than a thin wire.

The surface potential of the exposed film was measured under two conditions: transient decay, following charging, and steady-state charging. The transient decay was monitored by a vibrating Kelvin probe, as illustrated in Fig. 3(a). The vibrating metal plate generates an ac signal proportional to the difference in potential between the plate (known) and the film surface (unknown). A lock-in detector, sensitive only to the 400 hz frequency, monitors the ac signal. A precision voltage supply varies the potential of the vibrating plate until a null is obtained in the ac detector. The detection sensitivity is $\pm$ 0.05 V relative to an average film-surface potential of $\simeq$ 100 volts.

E. Steady-State Potential Measurements

The steady-state charging potential is measured by a comparison technique, as illustrated in Fig. 3(b). The sample and a metal reference plate of equal area are placed symmetrically in the corona field and the currents to both are monitored. If the surface potentials of the film and the metal plate are unequal then the two currents will also be unequal. Conversely, equal currents correspond to equal potentials. In the imple-

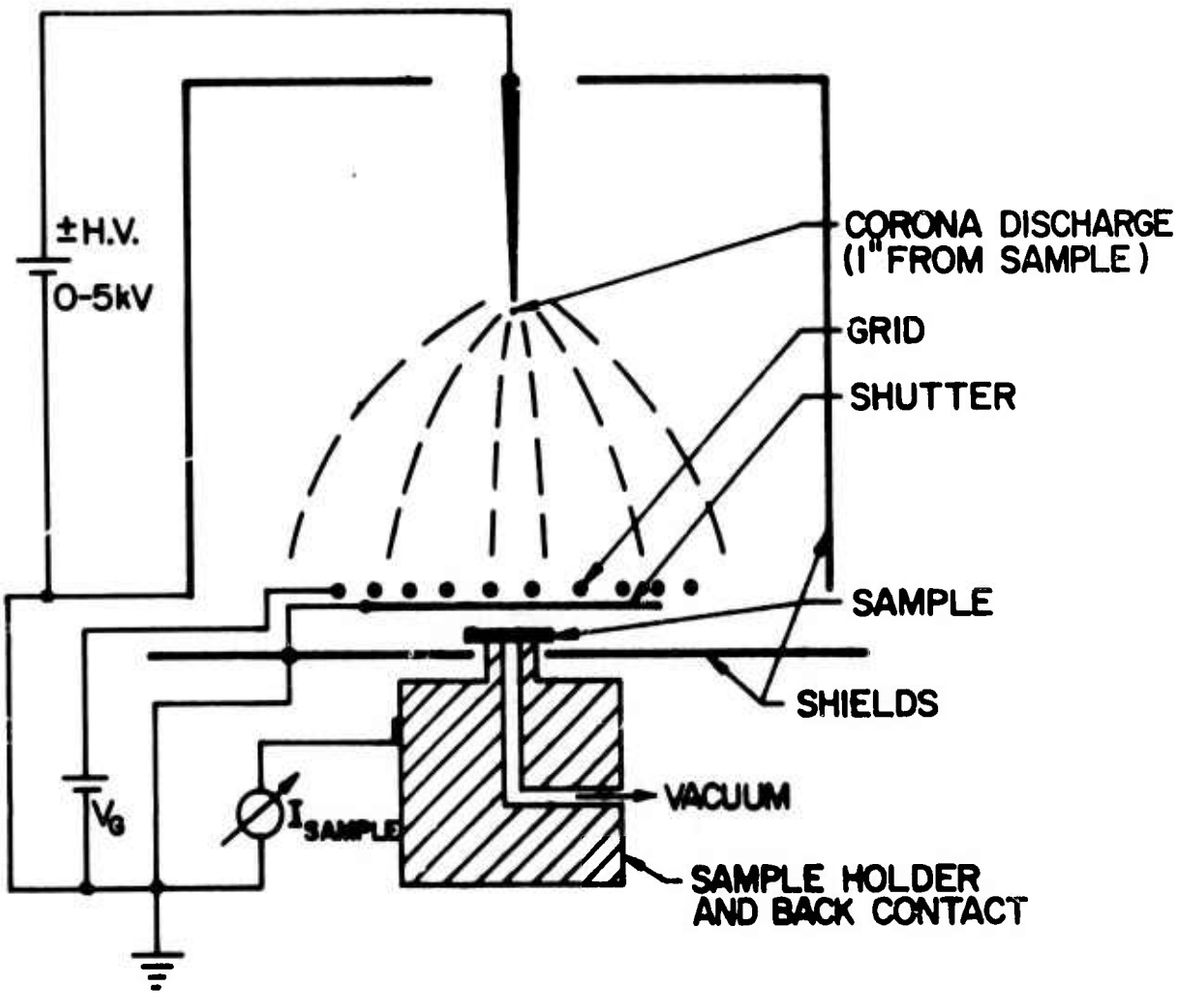

CORONA SOURCE

FIGURE 2

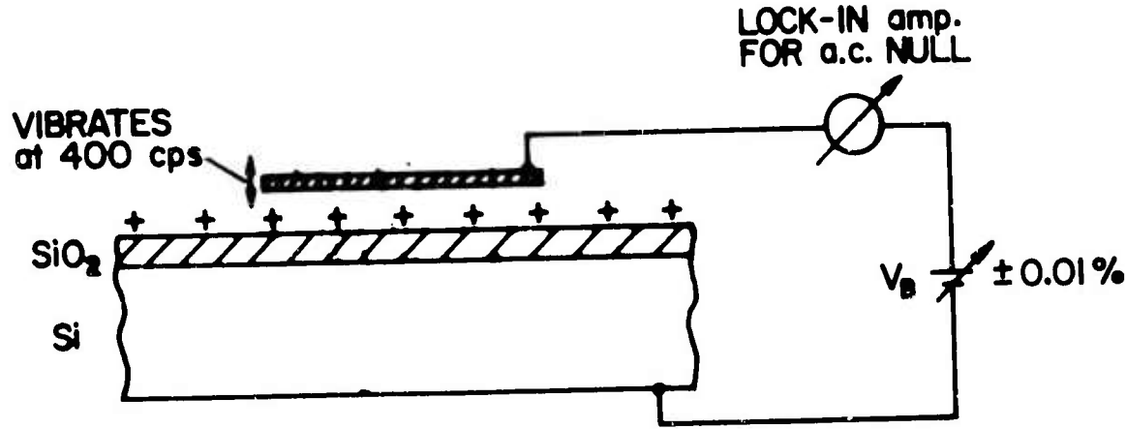

a) VIBRATING KELVIN-PROBE FOR MEASURING SURFACE POTENTIAL AND ITS DECAY AFTER CHARGING. (SENSITIVITY: 0.1 %)

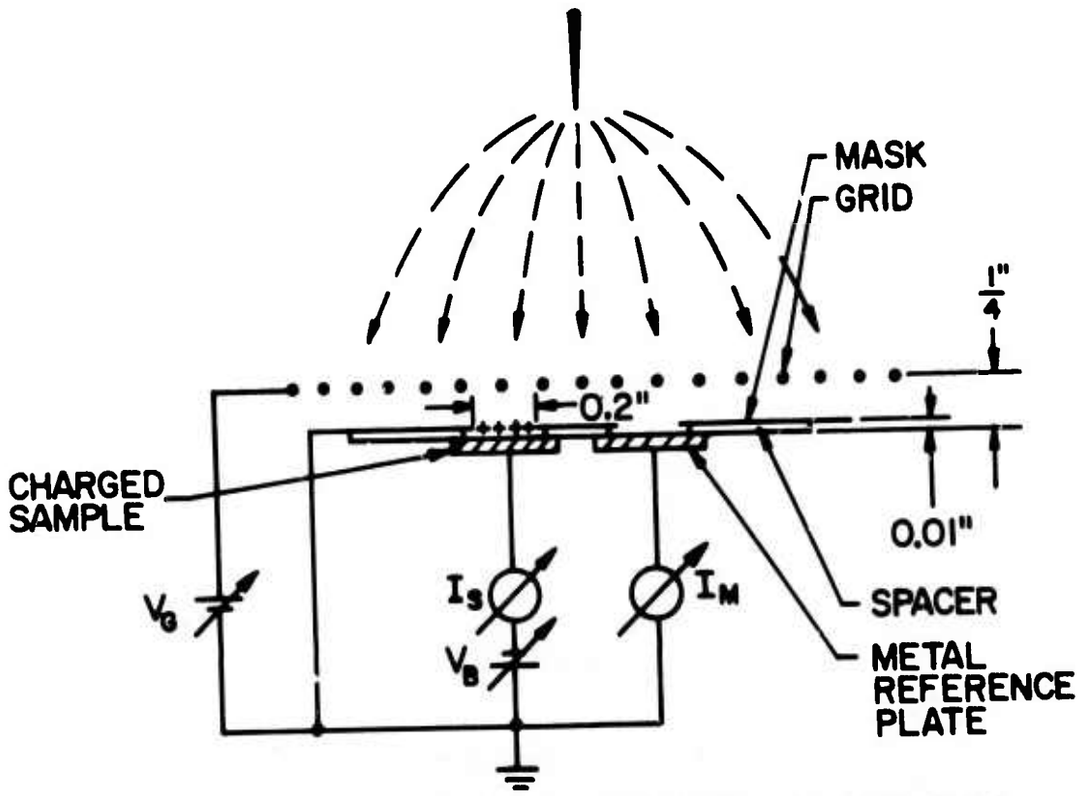

b) COMPARISON METHOD FOR MEASURING SURFACE POTENTIAL UNDER STEADY STATE CHARGING. (SENSITIVITY: 2 %)

SURFACE POTENTIAL MEASUREMENTS

FIGURE 3

mentation of this simple idea, the two surfaces are surrounded by a grounded mask, as shown in Fig. 3(b). The mask ensures equal exposed areas of the two surfaces and prevents ions from reaching the sides or back of the sample. The metal reference plate is also grounded, the current being controlled by a grid, as shown. The potential V_B of the silicon back plate is adjusted so that the sample current I_s is the same as the current I_m collected by the metal plate. At this point the exposed surface of the film must also be at ground potential, and the oxide voltage V_{ox} must cancel the applied voltage V_B: $V_{ox} = -V_B$. In practice, the sensitivity of this technique can be as good as $\pm$ 1 V. However, when the sample response is very slow, the uncertainty in the final balance hinders its reliability. In a regime of quick response the method is both accurate and convenient. In this respect the method is quite complementary to the vibrating probe method, which is rendered impractical by quick decay. In fact, development of the steady-state, comparative method was spurred by the problem of coping with deep-depletion in the silicon substrate. With the substrate in deep inversion, a sufficiently fast rate of tunneling of carriers out of the inversion layer into the oxide can drive the substrate into a steady-state deep depletion. Since a sizable voltage can be absorbed across the deep-depletion layer the measured total sample voltage and the oxide voltage can differ substantially, leading to large uncertainties in the latter quantity. Since deep-depletion in silicon decays to normal inversion on a time scale shorter than a second at room temperature, the Kelvin probe method would be ineffective in studying this important regime. The steady-state, comparative method, in contrast, is well suited to this purpose.

F. C-V Measurements

A standard technique for measuring the sign and quantity of charge stored in an insulating film is the C-V measurement, conveniently made at a frequency of 1 Mhz.

Contact to the insulator surface is made by a probe in the form of a small mercury ball held in a platinum container with a 20 mil diameter opening. The physical mechanics of the measurement are such that it can only be carried out after charging, i.e. during the decay period. As is well-known, the C-V measurement is most sensitive to charge stored at or near the substrate-film interface, and is least sensitive to charge stored at or near the exposed film surface. Note that the sign of the charge stored in the film after corona charging need not be the same as the sign of the dominant current-carrier either during charging or decay. Thus, it is a matter of common experience that good SiO_2 films have negligible electron trapping states so that electron currents leave behind negligible stored negative charge.

G. The P-N Junction-Diode Substrate-Detector Experiments

One of the goals of our research has been to identify the sign of the current-carrier in the oxide during breakdown. This goal has been achieved through the use of a shallow-junction P-N diode for the substrate, instead of a homogeneous wafer, as illustrated in Fig. 4. In addition to being a low-leakage junction, the main requirement on the junction is that it be shallow, i.e., sufficiently close to the interface that a minority carrier, injected into the diode from the oxide, will diffuse to the junction with negligible probability of recombination before reaching the junction. In effect, the total structure may be viewed as a transistor, with the oxide film serving as the emitter and the diode-proper furnishing the base and collector. In the polarity used for Fig. 4(b) (negative corona), if the dominant current carrier in the oxide during breakdown is holes, tunneling in from the p-region of the diode, then the only current observed in the external circuitry will be that in the circuit connected to the p-region (the current labelled I_p in Fig. 4(b)). Conversely, in terms of the transistor

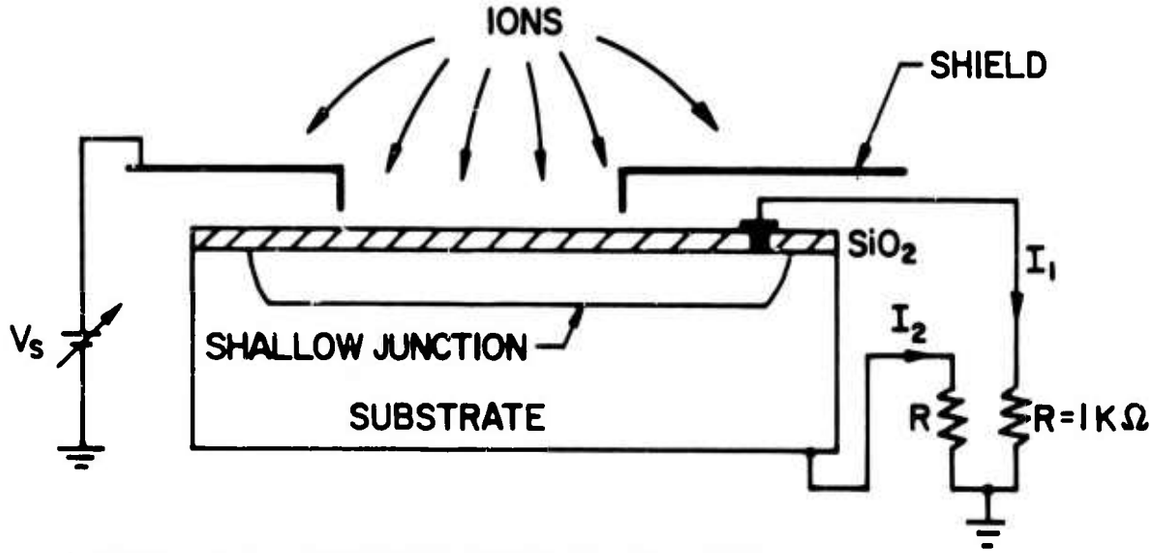

a) SHALLOW-JUNCTION DIODE EXPERIMENT

DIODE AREA : 4×7 mm , REVERSE DARK CURRENT ≈ 1×10^{-9}amp
JUNCTION DEPTH: 5000 Å ; DOPING DENSITY 10^{17}-10^{18} cm^{-3}
$\rho_{SUBSTRATE}$: 1 - 10 Ω-cm ; SiO_2 THICKNESS: 1000 Å OVER DIODE , 6000 Å ELSEWHERE.

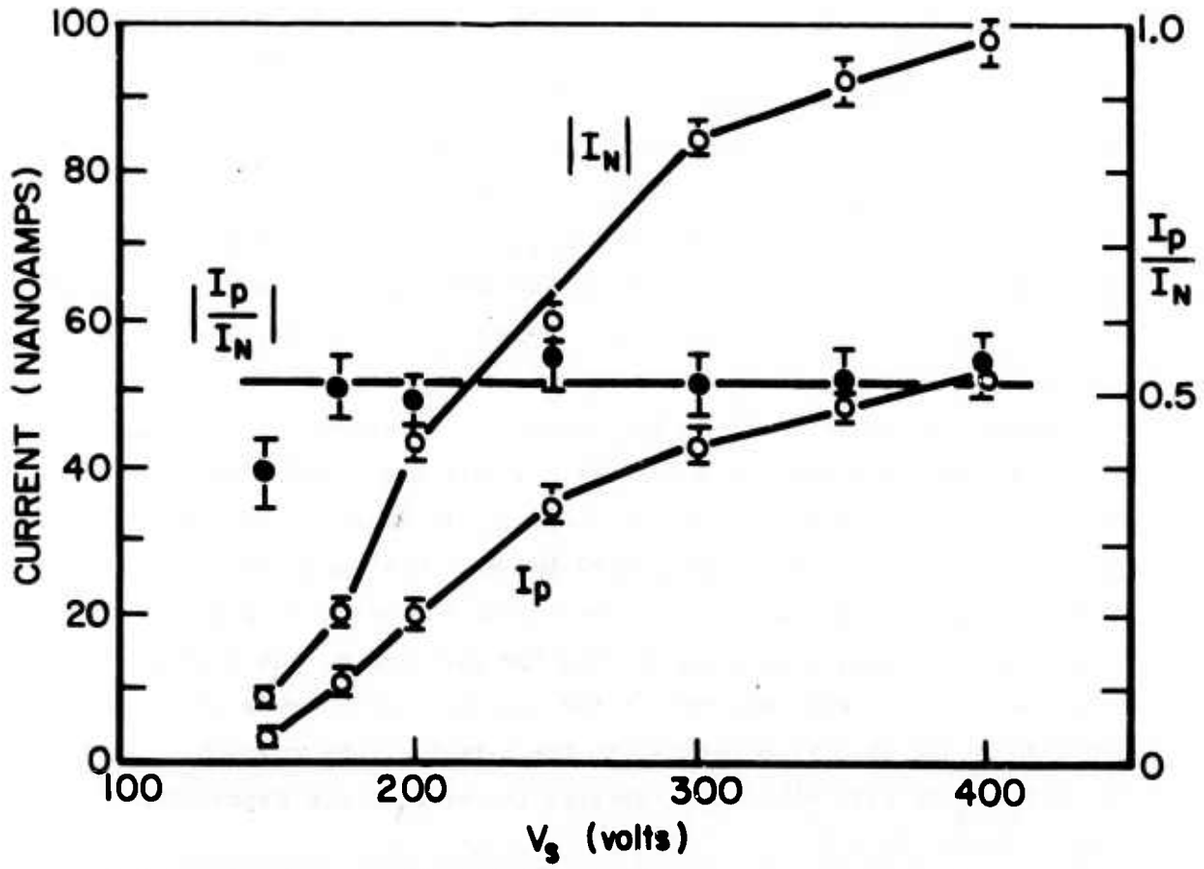

b) NEGATIVE-CORONA RESULTS : $I_p \equiv I_1$, $I_n \equiv I_2$ (SEE (A))

SHALLOW-JUNCTION DIODE EXPERIMENT ; RESULTS FOR NEGATIVE CORONA

FIGURE 4

analog cited above, if the dominant current in the oxide were electrons, tunneling in from the negatively charged states on the exposed surface of the oxide, then one might expect the only external current observed to be that flowing in the circuit connected to the n-region (the current labelled I_n in Fig. 4(b)), except for a very much smaller hole-circuit current I_p due to a small amount of recombination in the p-region. The actual measured currents, presented in the Fig., correspond to neither situation. In effect, sizable currents are observed in both circuits with $I_n \simeq -2\ I_p$. This result is readily explained in terms of the known energy-band structure of the $Si\text{-}SiO_2$ interface, as presented in Fig. 1. Electrons entering the silicon from the oxide are initially very hot; in fact, these electrons lie at least 3.1 ev above the conduction band minimum in the silicon - more, if the electrons are also hot in the oxide. Thus, the entering electrons have an excess energy at least three times the silicon bandgap. The mean free path for creation of an electron-hole pair on the silicon by such a hot electron is exceedingly short, probably less than 50Å. (Note that the emission of one or two optical, or acoustical, phonons by the hot electron, prior to the impact-ionization event, is of no consequence). Thus, with near-certainty the one hot electron quickly becomes two electrons and one hole. The two electrons are collected by the n-region, after diffusing to the junction, and the hole is ohmically relaxed out of the p-region. The current data in the Fig. quite accurately reflect this picture. Starting from 3 ev, the first-generation progeny (the first electron-hole pair) both have excess kinetic energy. However, on the average the parent electron and the two progeny will evenly divide up the total available excess of 2 ev leaving each of the three without sufficient energy for another impact-ionization event. Note that the rather accurate two-to-one ratio of $|I_n|/I_p$ is rather cogent evidence <u>against</u> hot electrons in the <u>oxide</u>, despite the high breakdown field $\simeq 1.3 \times 10^7$ V/cm.

If the electrons in the oxide had been heated to 2 or 3 ev before entering the silicon, the corresponding excess energy in the oxide would have been 4 or 5 ev (subtracting out the silicon bandgap) instead of 2 ev and subsequent electron-hole progeny would become almost a certainty, leading to $I_p / |I_n|$ values closer to unity than the 0.5 actually observed, and to $I_p / I_{ox} = I_p / (|I_n| - I_p) \gtrsim 2$, instead of the $\simeq 1$ actually observed.

We see that the shallow-junction diode experiment not only established that, for negative corona in dry air, the breakdown carriers in the oxide are tunneling electrons from the surface, but it has also furnished very strong evidence that the electrons in the oxide are not strongly heated up by the very high field, $\sim 1 \times 10^7$ V/cm. The direct demonstration of hole-creation in the silicon near the interface has important bearing on an interesting phenomenon to be discussed below, and that is the build-up of positive charge in the oxide above a certain current level ($\simeq 5 \times 10^{-9}$ amp/cm^2) with negative corona. It will be argued below that this build-up is probably due to the tunneling of the impact-generated hot holes from the Si into the oxide.

With positive corona in dry air the diode experiment yields only one circuit current, that in the circuit going to the base region of the analog transistor, i.e., the n-region of the diode. From this it is concluded that the breakdown carriers in the oxide are electrons which have tunneled in from the silicon. The C-V measurements after charging yield no flat-band shift, indicating negligible trapped charge in the oxide — completely consistent with the above interpretation. (A dominant hole current in SiO_2 will always yield trapped positive charge). Further evidence confirming electron current injection comes from a detailed study of the decaying surface potential after charging, as discussed below. These measurements, which are extremely accurate, are in excellent agreement with a theoretical model based on Fowler-Nordheim tunneling of electrons from the conduction band of Si into the SiO_2.

In addition to the above purposes which the junction-diodes have so usefully served, they can also be very useful in obtaining other kinds of valuable information. Virtually any source of electron-hole excitation in the silicon can be detected by the diodes. For example, we were able to demonstrate, using the diodes, that light emitted in the region of the corona discharge around the needle point and reaching the exposed insulator surface had a negligible effect on our measurements. (In this demonstration the shield was biased to cut off the ion current to the oxide).

H. Preliminary Results with Dry Nitrogen

The results discussed up to this point were obtained in the environmental chamber in a dry air ambient. Some preliminary experiments were carried out in a dry N_2 ambient in a bell jar. With positive corona the breakdown field in the oxide was the same as in the dry air experiment. However, with negative corona the breakdown field differed substantially from the dry-air value. These results are pre-eminently sensible in view of our interpretation of the dry-air experiments. So long as breakdown proceeds by tunnel-injection of electrons from the silicon into the oxide (positive corona) the breakdown field of the oxide will obviously be independent of the discharge ambient. On the other hand, if breakdown proceeds from tunneling of electrons out of surface states (adsorbed ions from the negative corona), it will be sensitive to the nature of the adsorbed ion, which may be expected to vary as the ambient is changed. A systematic exploration of the breakdown behavior of the oxide in a variety of gaseous ambients is expected to shed more light on these phenomena.

I. Steady-State I-V Characteristics

Current-voltage characteristics for the non-destructive breakdown of the oxide film induced by a corona (both + and -) in dry air are exhibited in Fig. 5. These characteristics were obtained under steady-state charging conditions using the comparison technique previously described. The lower levels of

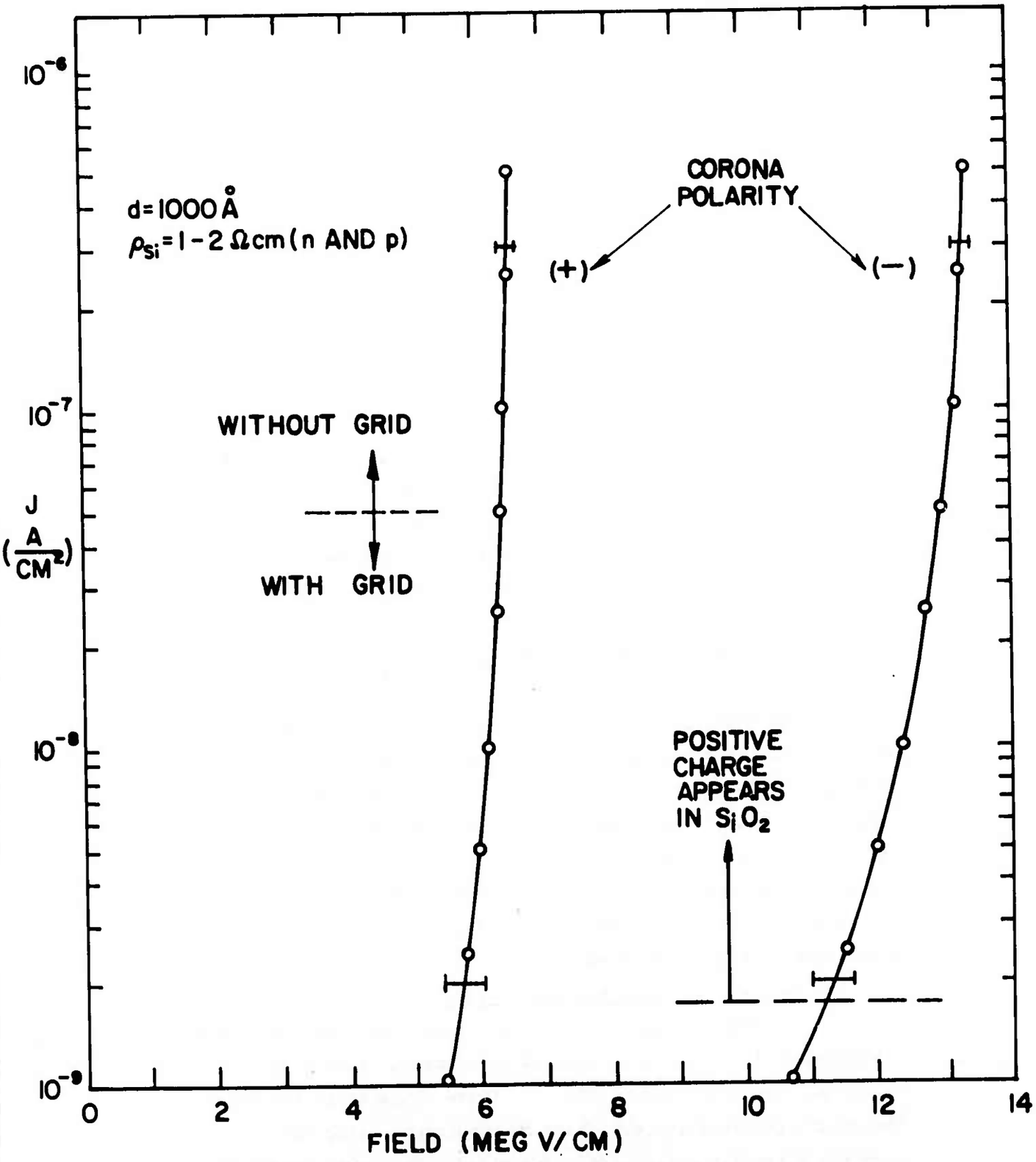

CURRENT-VOLTAGE CHARACTERISTICS FOR NON-DESTRUCTIVE BREAKDOWN OF SiO_2 ON Si (POSITIVE AND NEGATIVE CORONA IN DRY AIR)

FIGURE 5

current are controlled by a grid, as seen in Fig. 2, and the higher levels are controlled by varying the voltage on the corona needle. The relatively large error bars at the lower levels of current are a manifestation of the slow response of the insulator, as previously discussed. At higher current levels the error bars are narrower, but still there is not sufficient resolution to give truly quantitative results, i.e. results sufficiently precise to test a theoretical model for I vs V. However, the resolution is sufficient to define a 'breakdown field'. Further, there is a substantial overlap of this region with the same region of I vs V as measured for the decaying surface potential by the more precise Kelvin probe method, as previously discussed. The two methods give the same results.

Note that for a given sign of corona the same I vs V curve is obtained for both n- and p-silicon substrates. For the negative corona this is an expected result since the breakdown is initiated at the exposed, charged surface of the oxide (by tunneling of electrons out of the adsorbed ions into the oxide conduction band). For the positive corona the coincidence of I vs V curves for both n- and p-substrates conveys an interesting piece of information. The n-substrate is in strong accumulation and the p-substrate in deep inversion. Our results show that, at room temperature, the pair-generation rate in the p-Si (near or at the interface) is sufficient to supply the oxide current without widening of the depletion layer just behind the inversion region, i.e. without driving the p-silicon into deep depletion. By lowering the substrate temperature, the pair-generation rate can be made sufficiently slow (it is a thermally activated process which decreases exponentially with temperature as exp $(-E_o/kT)$) that the p-silicon must go into deep depletion. At sufficiently low temperature only steady-state avalanching in the deep-depletion region can supply the oxide current. These effects have already been observed, at room temperature, in analogous

experiments on MNOS structures (with very thin oxides).[4] We plan to look for them in corona experiments on pure SiO_2 films at lower substrate temperatures.

J. Thickness Dependence of the Breakdown Field

SiO_2 film breakdown fields have been obtained, through I vs V curves as in Fig. 5, for both + and - corona in dry air, over a range of oxide thicknesses between approximately 500 and 3000Å. The data points, plotted in Fig. 6, show a negligible thickness dependence over this thickness range. (The apparent small drop at 2700Å is attributed to a larger systematic error at higher voltages). This observed thickness independence is important for the theoretical modeling of the breakdown. Rather similar results (thickness independence) have been obtained for Al_2O_3 films on Si (the Al_2O_3 being deposited by pyrolysis), with Au electrodes, in an MOS capacitor configuration, by Carnes and Duffy[5], as seen in Fig. 7 (a), reproduced from Reference 5. Shown in Fig. 7(b)[6], reproduced from Reference 6, is a collection of breakdown data for Al_2O_3 films taken from a number of investigators. The most obvious thing about this Fig. is the state of confusion as regards the experimental breakdown situation for Al_2O_3 films. Most (possibly all) of this confusion must derive from the wide variety of deposition methods used in the preparation of the films.

K. Electron Tunneling Induced by Positive Corona

Careful measurements, using the vibrating Kelvin probe, were made of the decaying surface potential of the oxide, following charging by a positive corona. The decay was followed over a large time span, ranging from a few seconds to many hours, as shown in Fig. 8. The positive corona polarity is of particular interest because in this polarity the geometry of the experiment lends itself to detailed theoretical modeling, namely on the basis of Fowler-Nordheim tunneling from the conduction band of the silicon into the oxide. (In the negative corona polarity, as we have already seen from the shallow-junction diode experiments, we are dealing with electrons

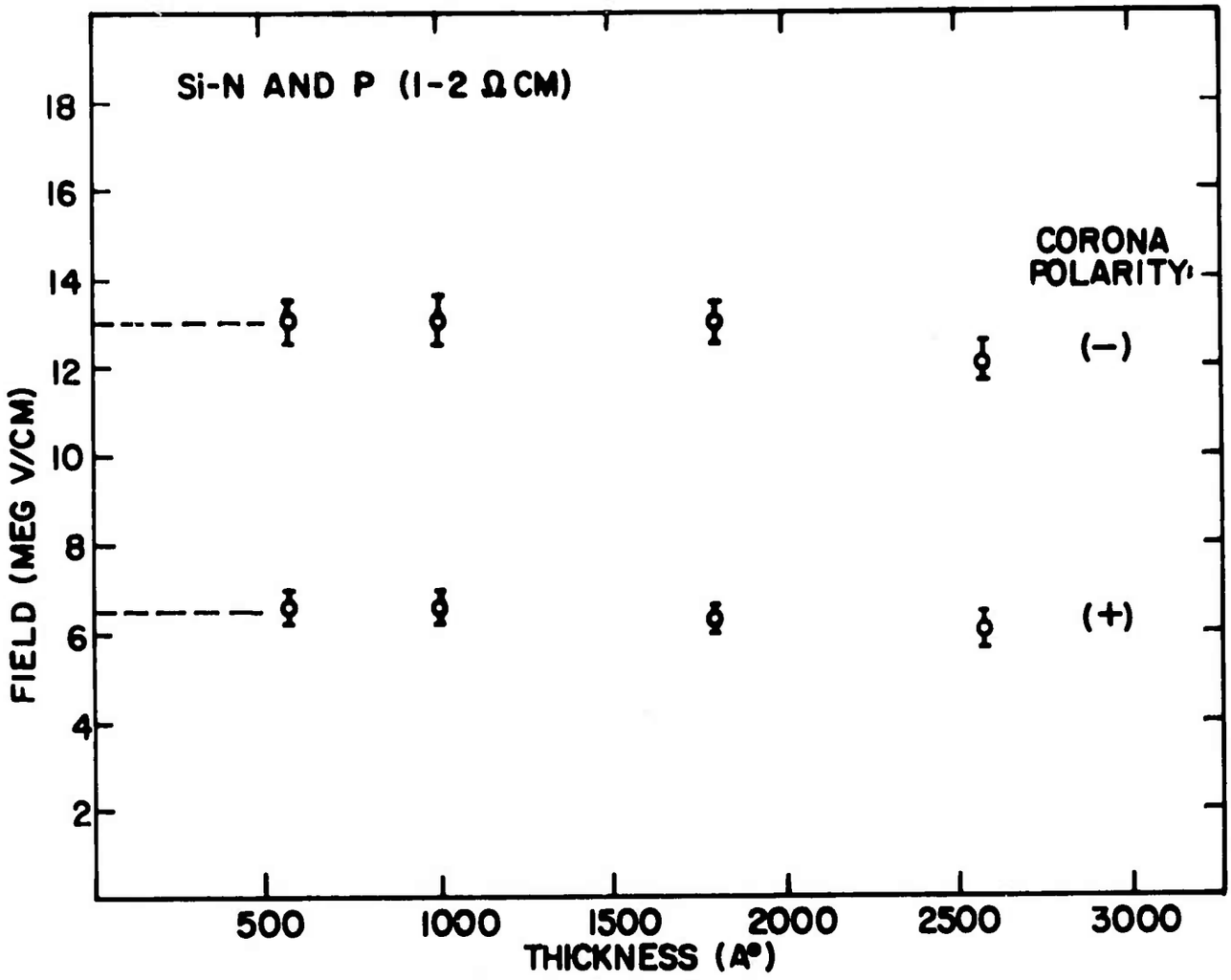

NON-DESTRUCTIVE BREAKDOWN FIELDS FOR BOTH POLARITIES OF CORONA IN DRY AIR

FIG. 6

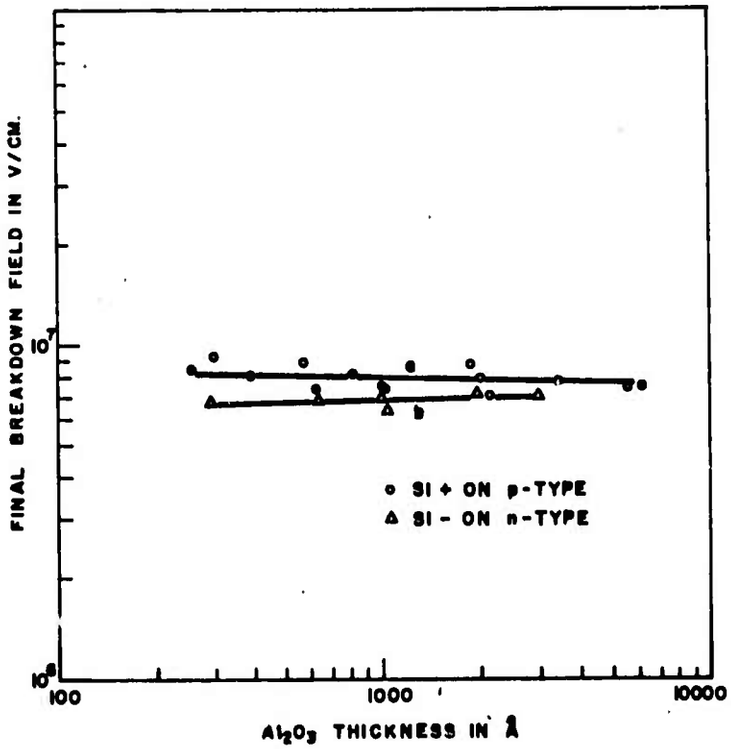

(a) *Breakdown field vs. Al_2O_3 thickness. (Al_2O_3 on Si. Ref. 5)*

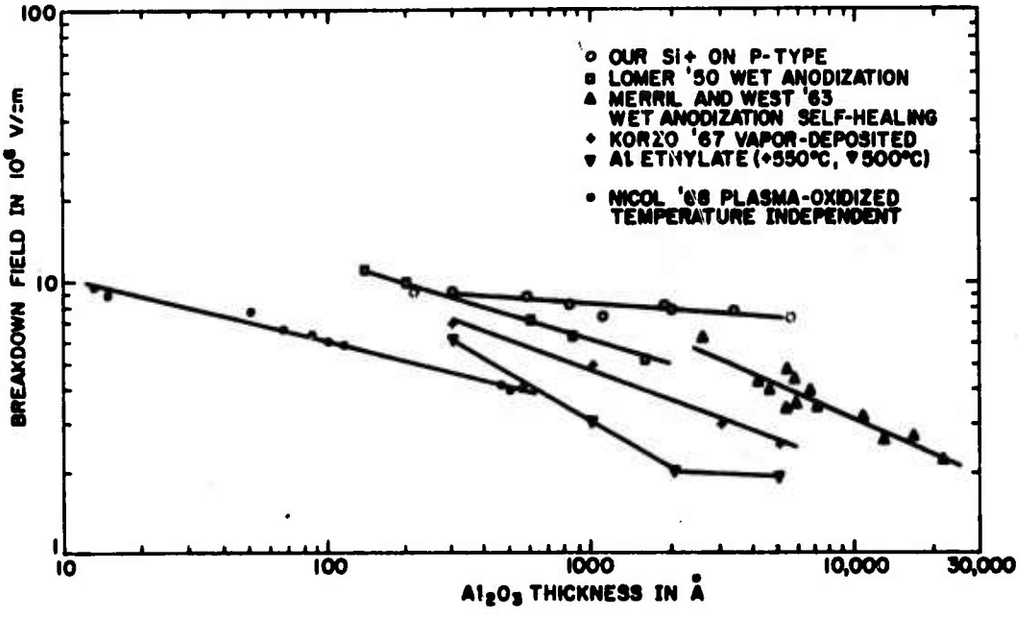

(b) *Al_2O_3 breakdown field vs. thickness as reported by several different workers. (Ref. 6)*

Fig. 7. Breakdown in AL_2O_3 Films.

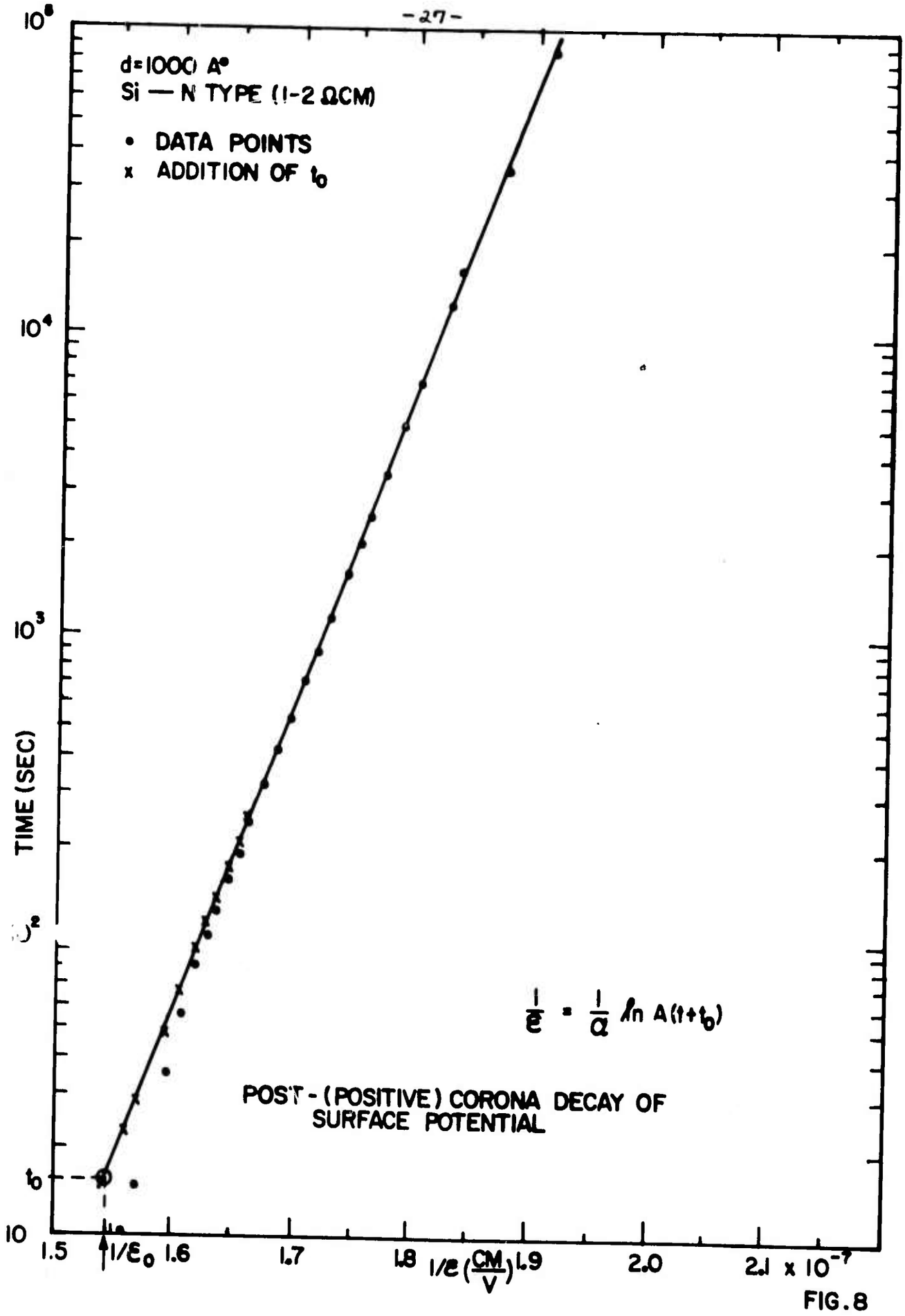
d=1000 A°
Si — N TYPE (1-2 ΩCM)
• DATA POINTS
x ADDITION OF t_0
10^5
10^4
10^3
t_0
10
TIME (SEC)
$\frac{1}{e} = \frac{1}{\alpha} \ln A(t+t_0)$
POST - (POSITIVE) CORONA DECAY OF SURFACE POTENTIAL
1.5
$1/\varepsilon_0$
1.6
1.7
1.8
$1/e\,(\frac{CM}{V})$
1.9
2.0
2.1 x 10^{-7}

FIG. 8

tunneling out of surface states (adsorbed ions) into the oxide. Since a detailed knowledge of these surface states is lacking at present - we know nothing of the trapped-electron wave function, or even its binding energy - a detailed theory is not possible for the present. For this reason the decay after negative corona charging is not discussed here). In order to interpret the positive-corona decay curve exhibited in Fig. 8 it is necessary first to sketch the background theory.

First we note that, since there is no observed trapping of electrons in the oxide, the field across the oxide is quite uniform, and accurately given by its nominal value: $\mathcal{E} = V_{ox}/d$. Since V_{ox} is a known, measured function of time, $\mathcal{E}$ is also a known function of time: $\mathcal{E} = \mathcal{E}(t)$.

The relations between the conduction-current density J through the oxide, the surface charge Q per unit area on the oxide, and the oxide field $\mathcal{E}$ are

$$J(t) = -\frac{d}{dt} Q(t) = -\varepsilon \frac{d}{dt} \mathcal{E}(t) \quad , \qquad (1)$$

where ε is the static dielectric constant of the oxide, and we have used Gauss' theorem.

For J we use the Fowler-Nordheim tunneling expression, here omitting the correction terms:[7]

$$J = \beta \mathcal{E}^2 \exp(-\alpha/\mathcal{E}) \quad , \qquad (2)$$

with

$$\alpha = \frac{4}{3} \frac{\sqrt{2m_{ox}}}{\hbar q \varepsilon} \phi^{3/2} \quad \text{and} \quad \beta = \frac{q^3 \varepsilon^2}{16\pi^2 \hbar \phi} \frac{m_{Si}}{m_{ox}} \quad , \qquad (3)$$

with ϕ the barrier height, as defined in Fig. 9, m_{ox} the

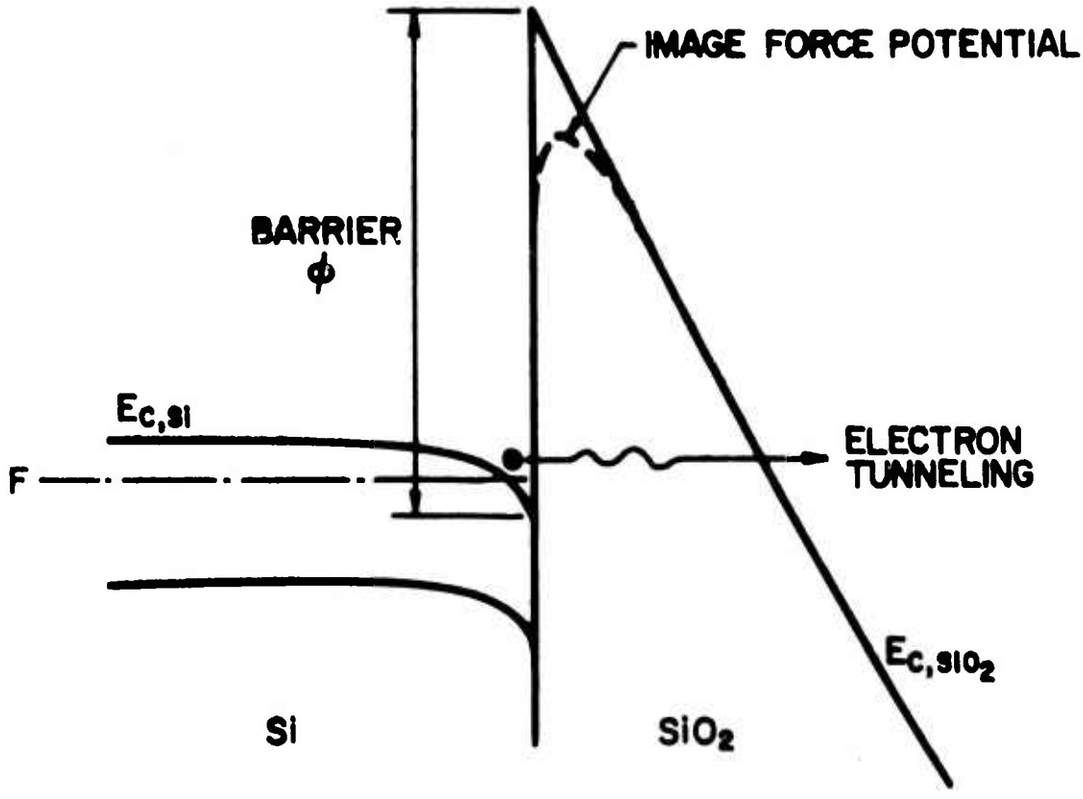

SCHEMATIC ENERGY-BAND DIAGRAM FOR FOWLER-NORDHEIM TUNNELING FROM THE CONDUCTION-BAND OF Si INTO SiO_2

FIGURE 9

electron effective mass in the oxide conduction band, m_{Si} the properly averaged (orientation-dependent) effective mass in the silicon conduction band, $\hbar$ = Planck's constant/2π , and q the charge on the electron.

Substitution of (2) into (1) yields the differential equation:

$$\beta \mathcal{E}^2 \exp(- \alpha/\mathcal{E}) = - \epsilon \frac{d\mathcal{E}}{dt} \quad , \qquad (4)$$

or

$$\frac{\exp \frac{\alpha}{\mathcal{E}}}{\mathcal{E}^2} \, d\mathcal{E} = - \frac{\beta}{\epsilon} \, dt \quad , \qquad (5)$$

which integrates directly to

$$\frac{1}{\mathcal{E}} = \frac{1}{\alpha} \ln A(t + t_o) \quad , \quad A = \frac{\alpha\beta}{\epsilon} \quad . \qquad (6)$$

The constant of integration t_o is determined from (6) evaluated at t = o :

$$\frac{1}{\mathcal{E}_o} = \frac{1}{\alpha} \ln At_o \quad . \qquad (7)$$

Equations (6) and (7) yield the oxide field $\mathcal{E}$ as a function of time t. Note that for $t >> t_o$ the predicted plot of $1/\mathcal{E}$ vs $\ln(t)$ is asymptotically linear, as observed experimentally (see Fig.9). Further, the slope of the asymptotic straight line gives precisely the constant α appearing in the Fowler-Nordheim expression (2). Finally, the experimental plot yields a value for A, from which the Fowler-Nordheim pre-exponential constant β is also determined.

In processing the experimental data points (circles) of Fig. 9, first the linear portion is extrapolated down to

$t = 0$, at which time the measured field $\mathcal{E}_o$ yields the constant t_o, using (7). When t_o is added to each value of t the resultant plot (crosses) in Fig. 9 is an accurate straight line extending over four decades in time (corresponding roughly to four decades in current), and following the predicted form, Eq. (6). The measured slope of this line gives α, which, according to (3) is related to $m_{ox}\phi^{3/2}$. Using for ϕ its recently measured value[8] we finally obtain:

$$(\ \phi = 3.1 \text{ ev}) \qquad \frac{m_{ox}}{m} = 0.39 \quad . \tag{8}$$

Note that this value for m_{ox} is in good agreement with previously published results of Lenzlinger and Snow[9], who studied tunneling in MOS capacitor structures. The following table compares our results for m_{ox} with theirs:

		m_{ox}/m	from ϕ
Lenzlinger and Snow	Tunneling from Si :	0.42	3.25 ev
	" " Al :	0.39	3.2
	" " Mg :	0.48	2.4
Our result	" " Si :	0.35	3.25*

(* Used for purpose of comparison only)

A theoretical value for A, the constant appearing in Eq. (6), is obtained from a more refined analysis of Fowler-Nordheim tunneling which will be presented in a more detailed report. Here we state only the result, namely

$$A_{\text{theoretical}} = 1.3 \times 10^{15} \text{ sec}^{-1} \tag{9}$$

Experimental values for A, obtained for three different oxide thicknesses grown on n-Si, are:

d (Å) :	587	1000	2580
A (sec^{-1}) ;	1.8×10^{15}	2.5×10^{14}	1.4×10^{15}

Considering the simplicity of the model this is quite satisfactory agreement with (9). It is to be recalled that the Fowler-Nordheim analysis is worked out for tunneling from a highly-degenerate Sommerfeld (non-interacting) electron gas into the vacuum. In the present set of experiments there is strong band-bending of the silicon at the interface. Thus the degenerate electron gas at the interface is actually held in a triangular well narrow enough to produce significant space-quantization effects. The latter have been studied extensively by Stern[10] and others at the IBM Research Laboratories, without considering tunneling. We have extended this analytical work to include tunneling into the oxide, as outlined in Section 8 of this report.

In concluding this discussion of decay experiments we would like to emphasize the accuracy and reliability of the technique. The Kelvin probe measurements have an accuracy of $\pm$ 0.1%. A potential is directly measured rather than a current; thus, weak spots in the oxide, of small area, have a negligible influence on the overall result. This is in marked contrast to MOS capacitor measurements where current is measured and where, consequently, weak spots can lead to large errors. Likewise, edge effects and potential spreading associated with metallic contacts and high fields are avoided with the present technique. Measurements on different samples cut from the same wafer give results that agree to within 0.1%. Different thicknesses of oxide have the same slope to within 1%. Our conclusion is that the corona-charging, potential-decay technique promises to be a powerful technique for further studies of tunneling.

L. Positive Charging Induced by Negative Corona

A final subject remains to be discussed in this section, and that is the observation of positive charging of the oxide under negative corona, as noted on Fig. 5. A typical charging rate, plotted as flat-band voltage shift vs time is shown in Fig. 10. The amount of positive charge corresponding to

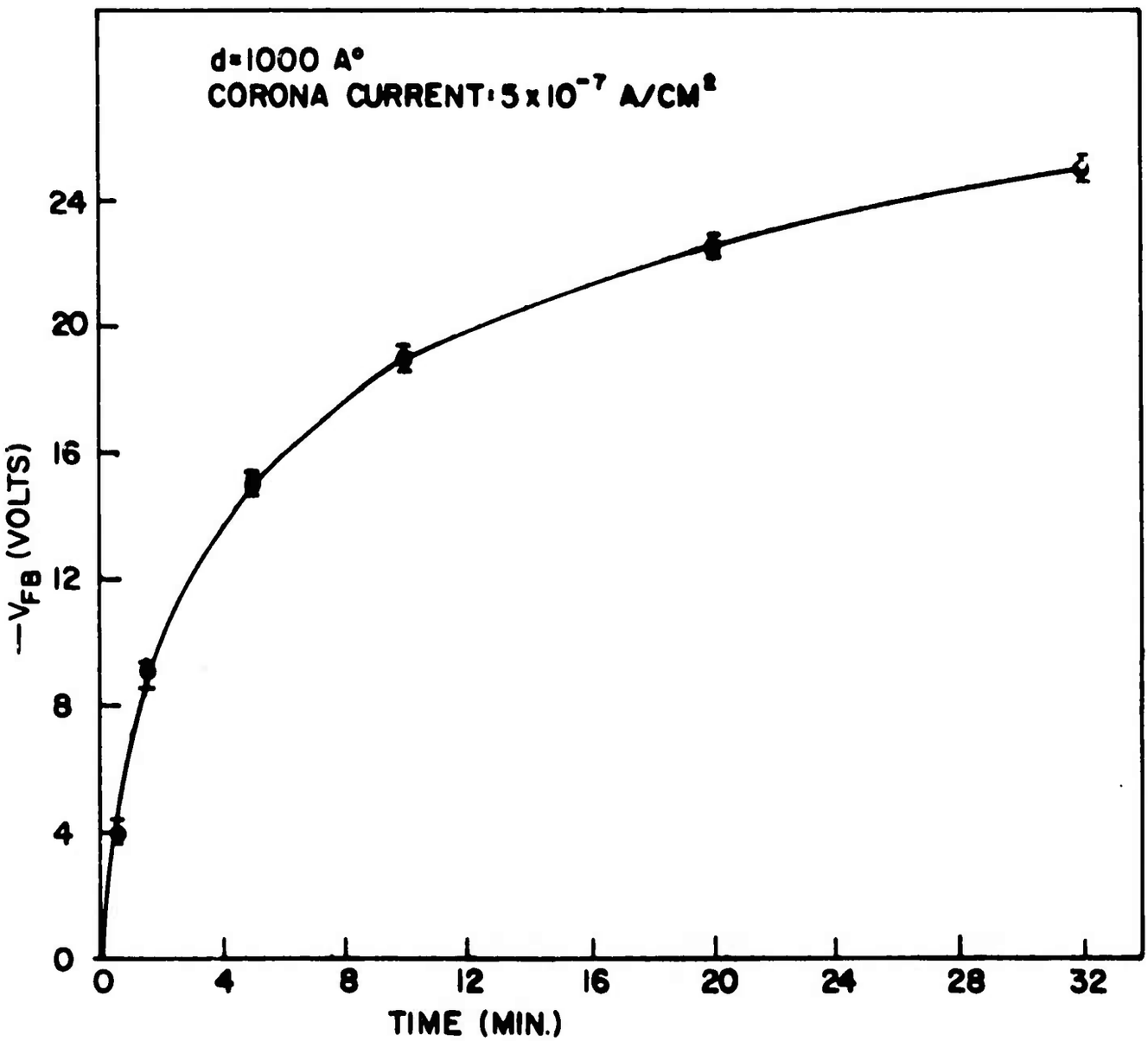

POSITIVE CHARGE BUILD-UP IN SiO_2 UNDER NEGATIVE CORONA

FIG. 10

V_{FB} = -20V and d = 1000Å is Q ≈ 5 x 10^{12} cm^{-2} (assuming the charge is trapped near the interface, as is certainly reasonable in the present problem. If the charge were trapped near the exposed surface, the corresponding Q would be higher). The simplest interpretation of this charging phenomenon is that it is due to the tunneling of holes from the Si into the SiO_2 at the very high fields, exceeding 1 x 10^7 V/cm. We proceed to analyze the charging on this basis, the model being schematically illustrated in Fig. 11.

The field in the oxide at the interface, $\mathcal{E}_I = \mathcal{E}_I(t)$, can be written, using Gauss' Theorem, as

$$\mathcal{E}_I(t) = \mathcal{E}_o - \frac{Q(t)}{\varepsilon} \quad , \qquad (10)$$

Q(t) being the charge trapped at (or near) the interface at time t, and $\mathcal{E}_o$ being the equivalent ohmic field, $\mathcal{E}_o$ = V/d. (V is constant in time, since these are steady-state corona experiments).

In the spirit of the tunneling model, we represent the hole current J_h entering the oxide from the silicon by a Fowler-Nordheim-like expression:

$$J_h = \frac{dQ(t)}{dt} = C \exp - \frac{\alpha_h}{\mathcal{E}_I(t)} \quad , \qquad (11)$$

neglecting the pre-exponential field-dependence, i.e., C ≠ C($\mathcal{E}$), since the model is not precise enough (at this stage) to warrant such a complication. Note that in writing (11) we have assumed that all injected holes are trapped in the oxide (presumably near the interface). Again, departure from this assumption would bring in unnecessary complications at this stage of the game.

Substituting for $\mathcal{E}_I(t)$ from (10) into (11) gives the differential equation for Q:

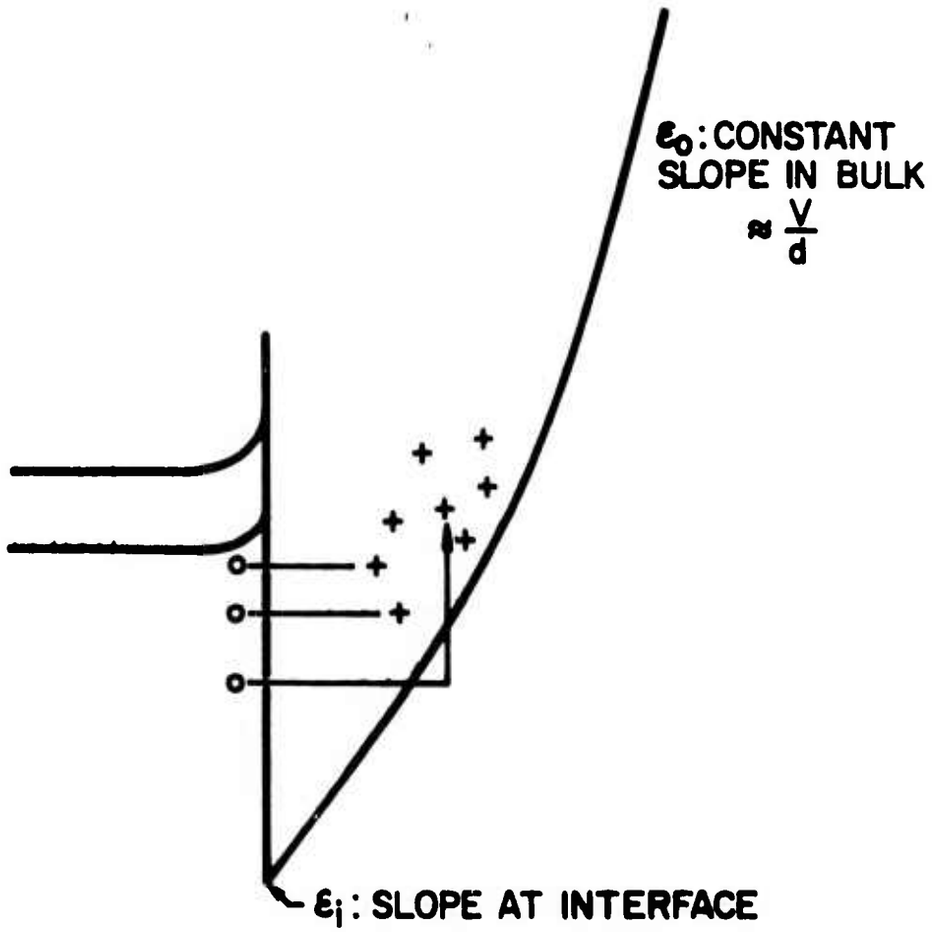

SCHEMATIC ENERGY-BAND DIAGRAM
FOR TUNNELING AND TRAPPING OF HOLES IN SiO_2

FIGURE 11

$$\frac{dQ}{dt} = C \exp - \frac{\alpha_h}{(\mathcal{E}_o - \frac{Q}{\varepsilon})} \quad . \tag{12}$$

Since, even at the upper end of the V_{FB} vs t plot in Fig. 10, the reduction in the field at the interface is only about 15% there is no significant loss of accuracy in expanding the exponent in (12), giving the new equation

$$\frac{dQ}{dt} = C \exp -\{\frac{\alpha_h}{\mathcal{E}_o}(1 + \frac{Q}{\varepsilon \mathcal{E}_o})\} = J_o \exp - \frac{\alpha_h Q}{\varepsilon \mathcal{E}_o^2} \quad , \tag{13}$$

where $J_o = C \exp(-\alpha_h/\mathcal{E}_o)$ is the initial hole flux.

Equation (13) is readily integrated to give

$$Q(t) = Q_1 \ln (\frac{t}{\tau} + 1) \quad , \tag{14}$$

with

$$Q_1 = \frac{\varepsilon \mathcal{E}_o^2}{\alpha_h} \quad \text{and} \quad \tau = \frac{\varepsilon \mathcal{E}_o^2}{\alpha_h J_o} \quad , \tag{15}$$

where the boundary condition: $Q(o) = o$, has been used.

The corresponding flat-band voltage shift is

$$V_{FB} = - \frac{Q(t)d}{\varepsilon} = - \frac{\mathcal{E}_o^2 d}{\alpha_h} \ln (\frac{t}{\tau} + 1) \tag{16}$$

In view of this theoretical expression, the experimental data of Fig. 10 were re-plotted on a semi-log plot exhibited in Fig. 12. It is seen that quite good linearity holds over the full two decades in time for which the data were available. From the slope of this line, using (16), a value for α_h is obtained, namely:

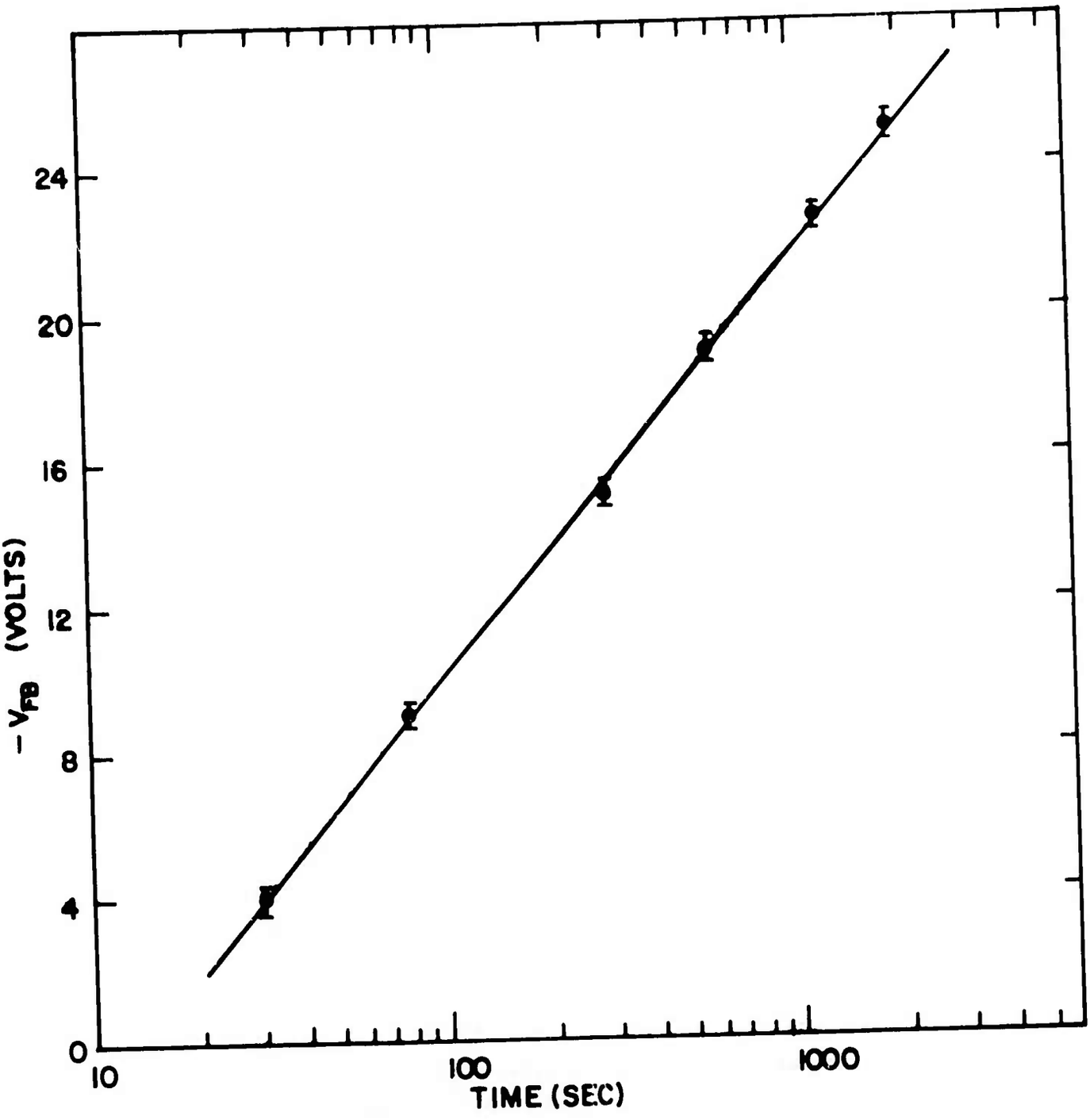

FLAT-BAND VOLTAGE SHIFT vs TIME DUE TO HOLE INJECTION FROM Si INTO SiO_2 (NEGATIVE CORONA)

FIG. 12

$$\alpha_h = (3.7 \pm 0.8) \times 10^8 \text{ V/cm} \quad . \qquad (17)$$

The corresponding Fowler-Nordheim constant for electrons, obtained from the surface-potential decay measurements, Fig. 8, is:

$$\alpha_e = 2.3 \times 10^8 \text{ V/cm} \quad . \qquad (18)$$

From (17) and (18) we see that, at most, $\alpha_h/\alpha_e \simeq 2$.

The theoretical value for this same ratio, assuming tunneling of thermal holes (for α_h) and thermal electrons (for α_e) is:

$$\left(\frac{\alpha_h}{\alpha_e}\right)_{\text{theor.}} = \left(\frac{m_{ox,h}}{m_{ox,e}}\right)^{1/2} \left(\frac{\phi_h}{\phi_e}\right)^{3/2} \simeq 2\left(\frac{m_{ox,h}}{m_{ox,e}}\right)^{1/2} \qquad (19)$$

where we have used the values $\phi_h = 4.8$ ev and $\phi_e = 3.1$ ev (see Fig. 1). We have already seen that $m_{ox,e} \simeq 0.4$ m. Although $m_{ox,h}$ is not known, a reasonable guess is that $m_{ox,h}/m \gg 1$, as would follow if holes in the oxide are either strongly self-trapped (a speculative concept) or drift in an equivalently very narrow band (very high density of states at the top of the valence band). Finally, note that the calculated Fowler-Nordheim $J_o \simeq 10^{-8}$ A/cm^2 is quite consistent with the measured sample current, $J_s \simeq 5 \times 10^{-7}$ A/cm^2 already determined to be carried by electrons, whereas the calculated Fowler-Nordheim τ is about five orders of magnitude larger than the experimental τ, gotten from Fig. 12. All of these observations suggest strongly that tunneling of hot holes generated in the Si by the incoming electrons is responsible for the charging of the oxide. This hypothesis will be incisively tested experimentally.

3. Locally Destructive , Self-Quenching Breakdown in MIS Capacitor Structures (D. Y. Yang collaborating)

A. Summary

Work in continuing on the self-quenching breakdown (SQB) studies of pyrolytically deposited Al_2O_3 films on Si, and such studies have now also been initiated on thermally grown SiO_2 films on Si. Voltage-time studies of breakdown events on the Al_2O_3 structure, with a Au electrode, consistently give an order-of-magnitude longer time scale for breakdown with the substrate in inversion (hundreds of nanoseconds), than in accumulation (tens of nanoseconds). Charge-storage (C-V) measurements on the Al_2O_3 structures suggest that, whatever the polarity of the Au gate, the breakdown is initiated at the Si interface. Photomicrographs of the Au gate show marked differences in the topography of the localized breakdown areas between the accumulation and inversion situations. The breakdown voltage vs time behavior of SiO_2 structures follows a pattern very similar to that of the Al_2O_3 structures, with an order-of-magnitude longer time scale for inversion as compared to accumulation. C-V measurements indicate negligible charge storage induced by negative gate voltage and either large-scale positive charge storage and/or production of new interface states induced by positive gate voltage. SEM studies of the SiO_2 structures after breakdown have shown marked differences in the topography of the breakdown spots produced by positive gate polarity as compared to negative gate polarity.

B. The Breakdown Voltage vs Time Behavior for Al_2O_3 Structures

The pyrolytic Al_2O_3 films have been studied over a thickness range 300 to 2000Å , on both p-Si and n-Si substrates, of resistivity approximately 1 Ω-cm, and with gold metallization of thickness ≈ 1000Å and area ≈0.01 cm^2. A constant voltage was applied to the MAS (metal-Al_2O_3- Si) structure through a series, current-limiting resistor R_L. Following the initiation of breakdown, the voltage across the film was monitored on a

Tektronix 546 oscilloscope. The breakdown pulse was used to trigger the oscilloscope sweep. (However, because of the built-in oscilloscope delay line a portion of the signal before triggering can still be seen). Typical voltage-time characteristics are exhibited in Figs. 13, 14 and 15 which are direct tracing of photographs of the oscilloscope screen. Upon breakdown, the voltage deceases sharply, then climbs back again, relatively slowly, (on a time scale determined by the external circuitry), to the full applied voltage. The most straight-forward interpretation of the voltage drop is that it is produced by discharge of the electrostatic energy stored in the capacitor through the breakdown spot. The turn-around point in the V vs t trace presumably corresponds to the instant of time at which either evaporation, or melting flow, or blow-out of the gate in the immediate neightborhood of the breakdown volume produces an open circuit between the intact area of the gate and the breakdown volume. It is this breakdown-produced open circuit that we call 'self-quenching'.(It has previously been called 'self-healing'. From the gross, overall capacitance point of view, this is appropriate terminology. From the microscopic point of view, there is severe local damage, and 'self-quenching' seems a more appropriate description). The recovery of the voltage across the capacitor is determined by the RC time constant, with R the current-limiting series resistance and C the MAS capacitance.

Figures 13(a) and (b) show the V vs t characteristic for a film thickness $\simeq$ 300Å, on a p-Si substrate. In (a) the Si is in accumulation (gate negative); in (b) the Si is in inversion (gate positive). Figure 13(a) is a single-shot breakdown; Fig. 13(b) is a multiple exposure exhibiting several breakdowns. As expected, there is some fluctuation in behavior from breakdown to breakdown. Comparing (a) and (b), it is seen that the time scale for the breakdown is a full order of magnitude longer with the substrate in inversion than in accumulation, an

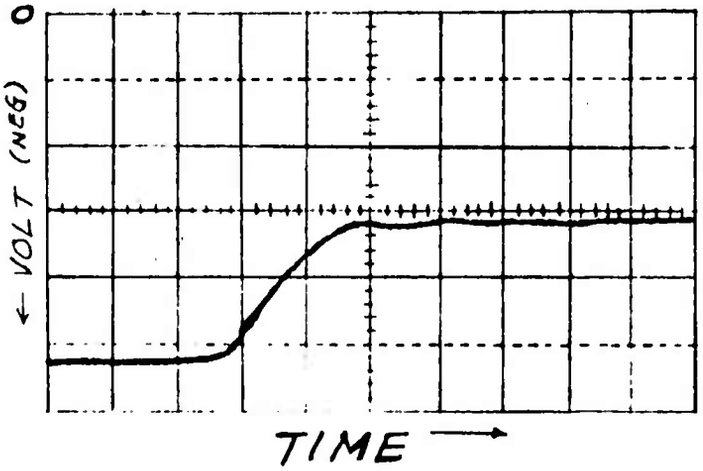

(a) Si in accumulation (Gate negative)

5 V/Div., 20 nanosec/Div., $R_L = 10\ k\Omega$

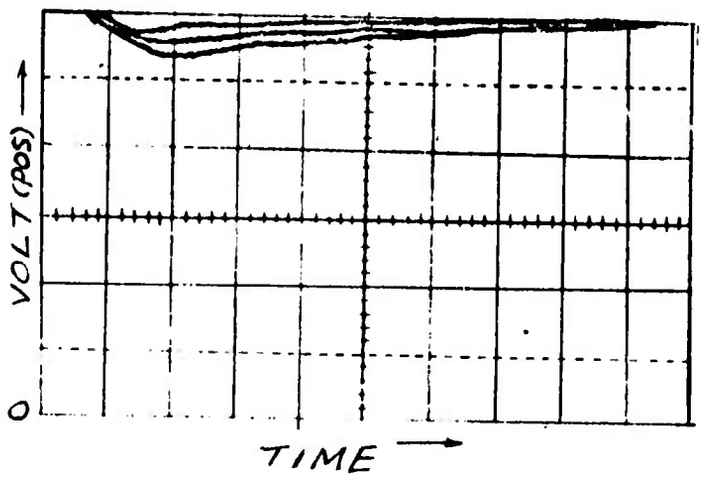

(b) Si in Inversion (Gate positive)

5V/DIV., 1 μsec/DIV.; $R_L = 10\ K\Omega$

FIG. 13. VOLTAGE-TIME CHARACTERISTICS FOR LOCALIZED BREAKDOWN OF $Au-Al_2O_3-Si$ STRUCTURES (FILM THICKNESS $\simeq 300$ Å, p-Si SUBSTRATE)

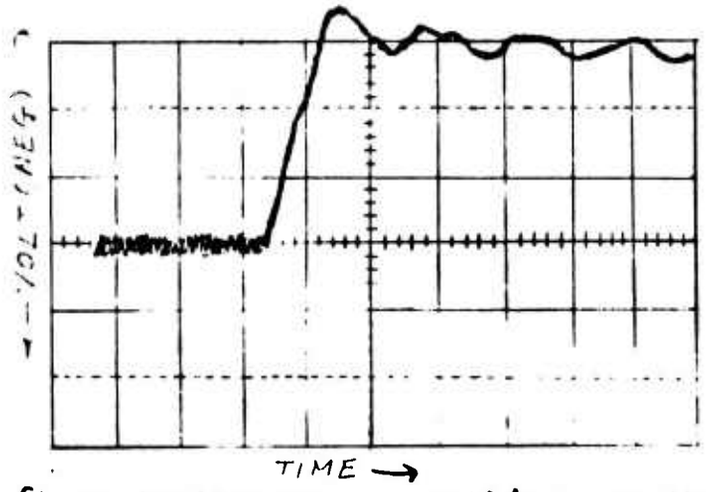

(a) Si IN ACCUMULATION ; 50 V/DIV , 20 NANOSEC/DIV ; $R_L = 10\ K\Omega$

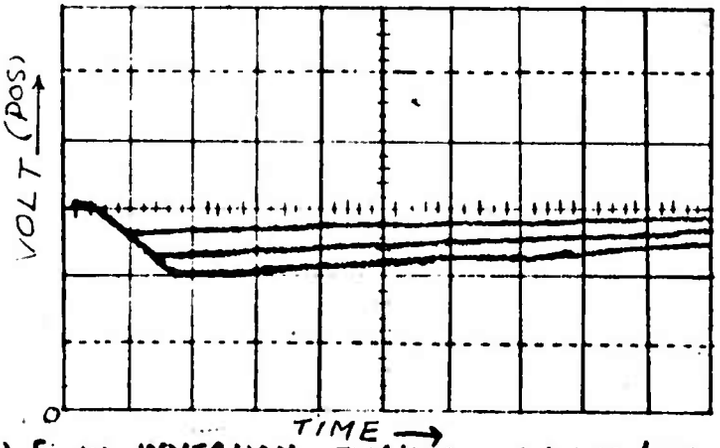

(b) Si IN INVERSION ; 50 V/DIV. ; 0.1 μSEC/DIV. ; $R_L = 10\ K\Omega$
(SAMPLE ILLUMINATED)

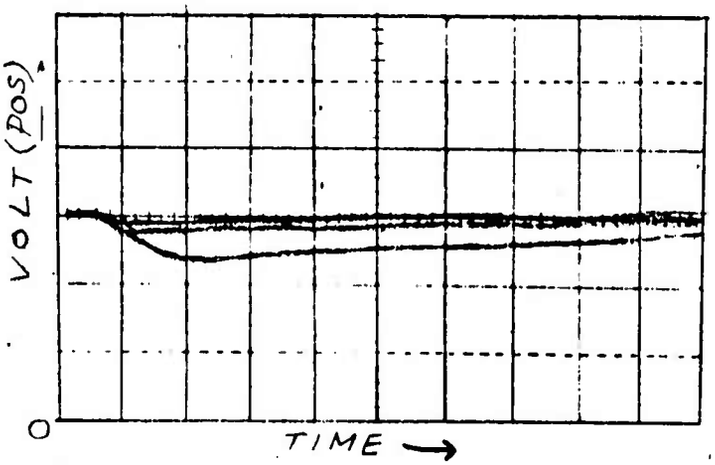

(c) Si IN INVERSION ; 50 V/DIV. , 0.1 μSEC/DIV. ; $R_L = 10\ K\Omega$
(SAMPLE IN DARK)

FIG. 14. VOLTAGE-TIME CHARACTERISTICS FOR LOCALIZED BREAKDOWN OF $Au-Al_2O_3-Si$ STRUCTURES (FILM THICKNESS ≈ 2000 Å , p-Si)

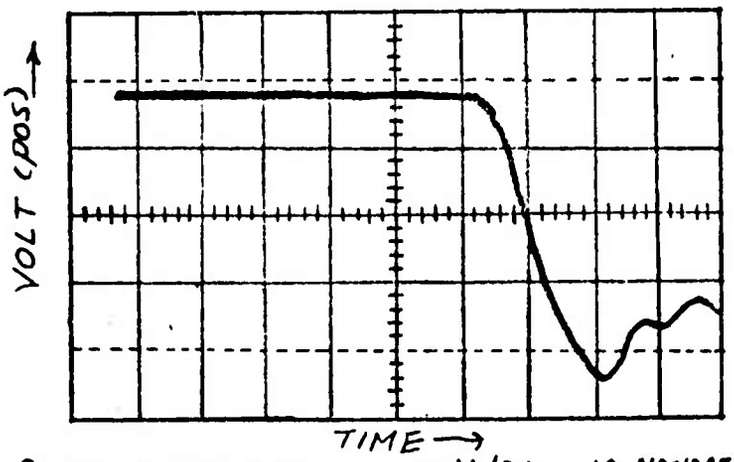

(a) Si IN ACCUMULATION; 20 V/DIV., 10 NANOSEC/DIV.; $R_L = 1 M\Omega$

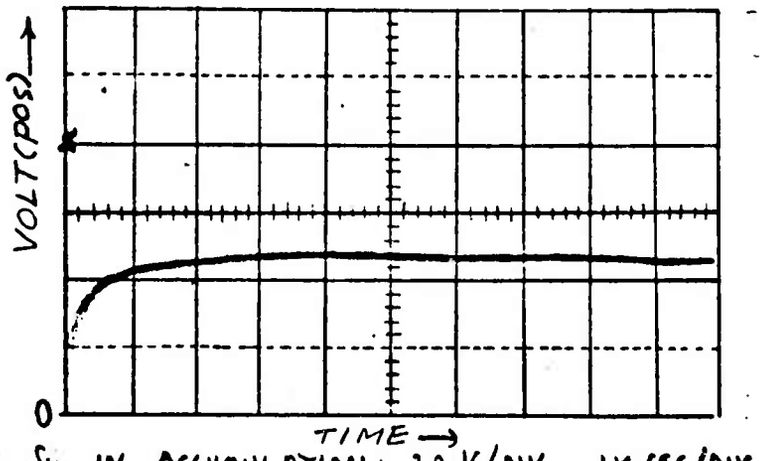

(b) Si IN ACCUMULATION; 20 V/DIV., 1 μSEC/DIV.; $R_L = 1 M\Omega$

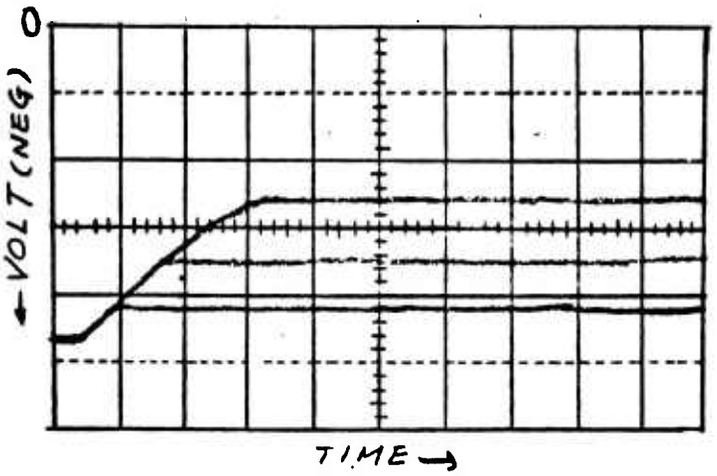

(c) Si IN INVERSION; 20 V/DIV.; 0.1 μSEC/DIV.; $R_L = 1 M\Omega$

FIG. 15. VOLTAGE-TIME CHARACTERISTICS FOR LOCALIZED BREAKDOWN OF Au-Al_2O_3-Si STRUCTURES (FILM THICKNESS ≈ 1000 Å, n-Si SUBSTRATE)

effect first reported by Klein in 1966[11] in studies of SiO_2 films on Si. Concomitantly, the fractional voltage drop across the oxide is much larger for accumulation than it is for inversion. Comparable results are obtained with a thicker Al_2O_3 film, $d = 2000\text{Å}$, on p-Si, Fig. 14, where (a) is taken in accumulation and (b) and (c) in inversion, (b) with light illumination and (c) in the dark. We note further, that with the substrate in inversion a microscope lamp shining on the sample through the gate, Fig. 14 (b), can shorten the breakdown time as compared to its value in the dark, Fig. 14(c) - an obviously reasonable result. Note that (a) is a single-shot exposure, (b) and (c) multiple-shot exposures. Figure 15 exhibits the V vs t transient for an n-Si substrate with $d_{ox} = 1000\text{Å}$. Figure 15(a) shows the normal fast breakdown for the substrate in accumulation. Fig. 15(b), also for accumulation, is unusual in that it exhibits two distinct time constants for the recovery following self-quenching, a normal, fast recovery initially, barely visible on the drawn-out time scale, 1 μsec/div, followed by a very slow recovery to full voltage. Figure 15(c) exhibits several breakdown transients, with the usual fluctuations. Some characteristic numbers for the voltage-time transients, derived from the oscilloscope photographs, are presented in Table I. (see page 46).

If the time-constant τ characterizing the voltage vs time transient is plotted vs d_{ox} the results obtained are as shown in the log-log plot of Fig. 16. It is seen that with the substrate in accumulation the data is well represented by the simple relation $\tau \propto 1/d_{ox}$. This suggests that an equivalent breakdown resistance R_B be defined thru

$$\tau_a = R_{B,a} C = R_{B,a} \frac{\varepsilon A}{d_{ox}} \quad , \qquad (20)$$

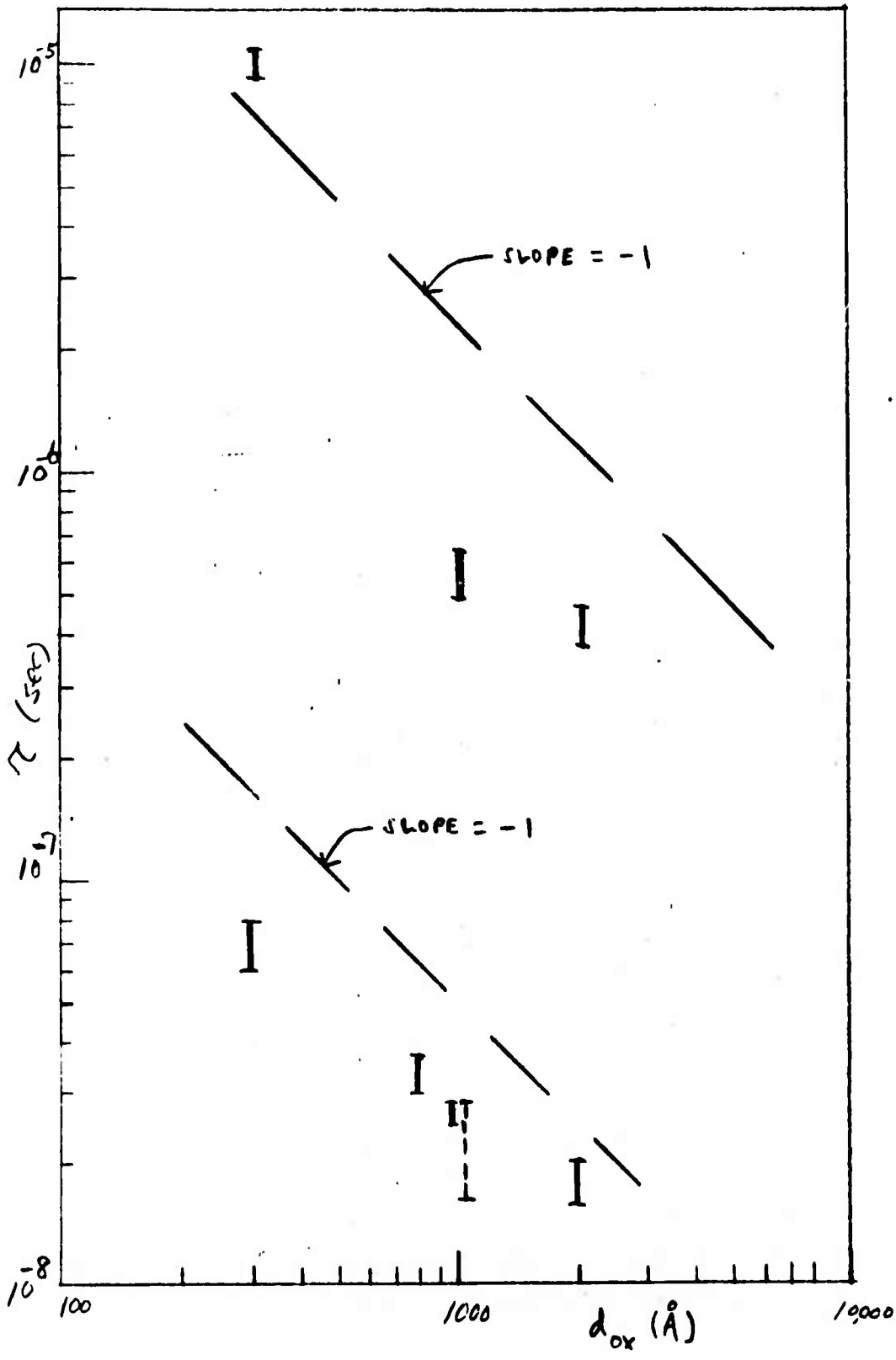

FIG. 16. BREAKDOWN TIME CONSTANT VS. FILM THICKNESS FOR $Au-Al_2O_3-Si$ STRUCTURES (AREA OF GATE: 0.01 cm^2)

Table I. Some Characteristic Numbers for the Voltage-Time Transients

Xtal type	Interface	d_{ox} (Å)	V_{appl}	V_{SQ} *	τ_{SQ} **	τ ***
p-	accum	300	-26V	-16V	40×10^{-9} sec	80×10^{-9} sec
p-	accum	2000	-150	0	20×10^{-9}	20×10^{-9}
n-	accum	1000	+95	+10	20×10^{-9}	20×10^{-9}
p-	inv.	300	+30	+27.5	1×10^{-6}	11×10^{-6}
p-	inv.	2000	+150	+100	100×10^{-9}	400×10^{-9}
n-	inv.	1000	-95	-70	150×10^{-9}	550×10^{-9}

* V_{SQ} is the voltage at the turn-around point in time

** τ_{SQ} is the time to turn-around

*** τ is the extrapolated time to reach 0 voltage, using the slope of the V vs t curve at t = 0.

---

with A the capacitor area, and with the subscript a added to signify that the substrate is in accumulation. (Correspondingly, the subscript i signifies that the substrate is in inversion). From the plot of Fig. 16, $R_{B,a} \simeq 100\Omega$. Using only the two points corresponding to $d_{ox} = 1000$Å and $d_{ox} = 2000$Å, then also in inversion, $\tau_i \propto 1/d_{ox}$, and $R_{B,i} \simeq 5K\Omega$. (There is a point for $d_{ox} = 300$Å which is well off the inversion straight line. However, it is also to be noted that thin-oxide substrates, in inversion, generally lead to shorts following breakdown and therefore, in some sense, embody different physical phenomena).

The V vs t relation associated with the simple RC representation (20) of the discharge is

$$V(t) = d_{ox}\mathcal{E}_B \exp - \frac{t}{R_B C} \quad , \quad V_B = d_{ox}\mathcal{E}_B, \qquad (21)$$

where V is the voltage across the oxide, V_B the voltage at breakdown, $\mathcal{E}_B$ the thickness-independent breakdown field, and R_B the equivalent breakdown resistance.

The power dissipated in the resistance R_B is

$$P = IV = \frac{dQ}{dt} V = C \left|\frac{dV}{dt}\right| V = \frac{(d_{ox} \mathcal{E}_B)^2}{R_B} \exp -\{\frac{2t}{R_B \varepsilon A} d_{ox}\}. \quad (22)$$

Equations (22) and (20) state that the initial power dissipation is proportional to the square of the oxide thickness, whereas the time constant for the dissipation is inversely proportional to the thickness. Assuming that the equivalent resistance R_B can be associated with an approximately fixed volume of silicon (or silicon plus oxide), as suggested by the large difference in time scales between the accumulation and inversion situations, we would infer that self-quenching is favored by thicker oxides. Further, from (22) we see that self-quenching is also favored by accumulation (smaller R_B) as compared to inversion (larger R_B). Indeed, we find that with thin oxides, d_{ox} in the range 300 to 800 Å, and with the substrate in inversion, the breakdown almost always leads to a short rather than to self-quenching. These results bear directly on Carnes' observation[5,6] that in his ramp-mode experiments it was very difficult to obtain consistent, reproducible behavior when the substrate was in inversion, although the same substrate, in accumulation, always exhibited definable, measureable behavior. With the thin oxides, and the substrate in inversion, it was generally not possible to obtain a voltage drop, following breakdown, sufficiently large to trigger the oscilloscope sweep. However, observation of the sample through the optical microscope did reveal the presence of bubble-like areas on the Au gate, but no visible evidence of local destruction.

C. C-V Measurements and Optical Photomicrography of Al_2O_3 Structures

C-V measurements were made on the Al_2O_3 structures to determine the charge storage in the oxide, both before the application of the high field and after the occurrence of self-

quenching breakdowns, Figure 17 exhibits the results for MAS samples with d_{ox} = 1000Å and with an n-type Si substrate. There is an initial, positive flatband voltage of approximately 15V prior to the application of high fields. With the gate positive, the flatband voltage shifted to +45V. On a different capacitor on the same sample, with the gate negative, the flatband voltage shifted in the opposite direction, from +15V to -25V after breakdown. There appears to be no distortion in the post-breakdown C-V curves. Other samples with a p-type substrate generally exhibited the same features. A simple interpretation of these results is that breakdown is initiated at the Si interface rather than at the Au interface. This important conclusion remains to be verified by independent experiments. Similar charging effects could be observed at high fields below the breakdown threshold. Pre-breakdown charging of the oxide might influence the breakdown via a distortion of the applied-field distribution away from the uniform, ohmic distribution.

Observations of self-quenching breakdown were made through an optical microscope. Breakdown events occurred randomly in space and were always accompanied by a flash of light. Figure 18 shows two typical photomicrographs, (a) taken of a p-type sample in accumulation, and (b) taken of an n-type sample in inversion. Figure 18(a) is typical of breakdowns with the substrate in accumulation, whether n-or p-type, and also for a p-type substrate in inversion. Corresponding to each breakdown event there is an outer circular area, of diameter $\approx$10 μ and an inner spot of diameter $\lesssim$ 1 μ. Figure 18(b) is typical of breakdowns with an n-type substrate in inversion. Corresponding to each breakdown there is an outer area of quite irregular shape, with a maximum dimension on the order of 20 μ roughly, or less. As in Fig. 18(a), there is also a much smaller inner spot. The photomicrographs suggest that there is an inner core to the discharge corresponding to a filament through which the capacitor energy discharges.

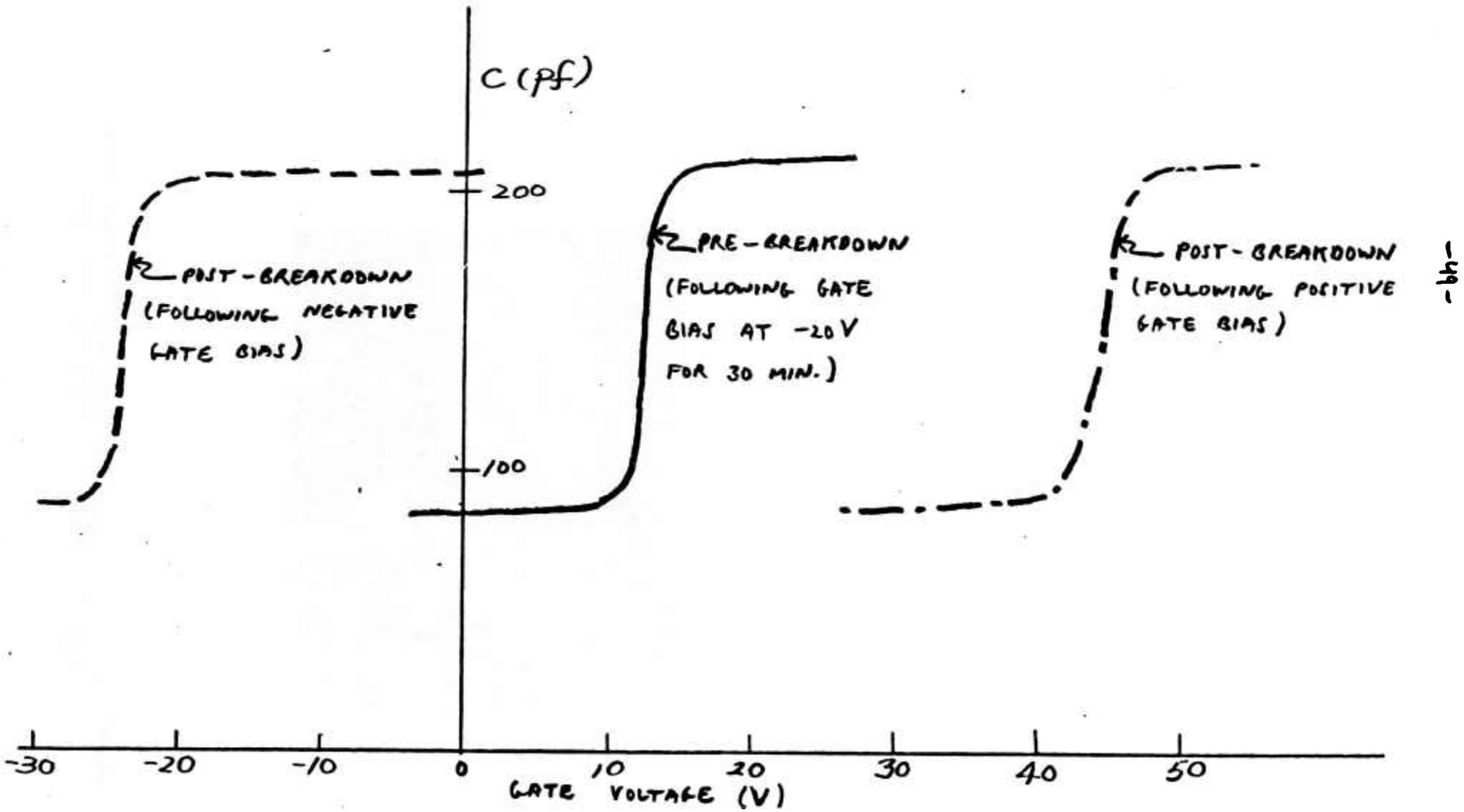

FIG. 17. C-V MEASUREMENTS ON Au-Al_2O_3-Si STRUCTURES BEFORE AND AFTER BREAKDOWN (AT BOTH SIGNS OF GATE BIAS)

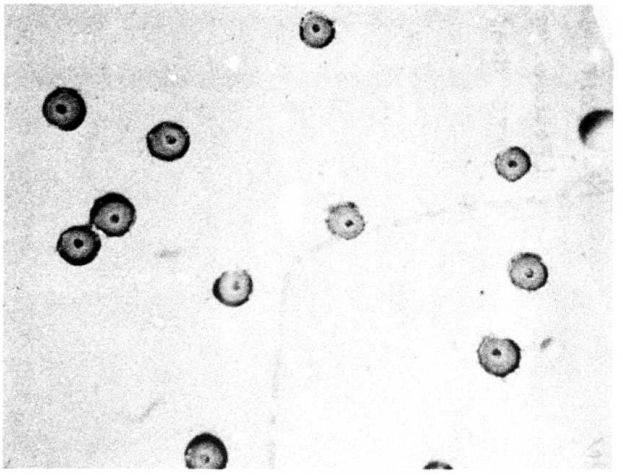

(a) p-Si in Accumulation, d_{ox} = 2000Å

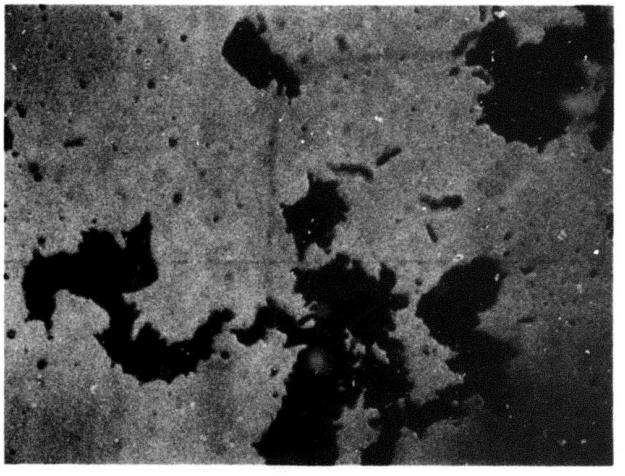

(b) n-Si in Inversion, d_{ox} = 1000Å

Fig. 18. Optical Photomicrographs of Localized Breakdown Areas on Au-Al_2O_3-Si Structures. (Magnification: 300X)

D. The Breakdown Voltage vs Time Behavior for SiO_2 Structures

Breakdown voltage vs time studies, similar to those discussed in Section B for Al_2O_3 structures, have also been made on SiO_2 structures. The oxides are thermally grown, to an approximate thickness $d_{ox} \simeq$ 2500Å, on both n- and p-Si substrates of resistivity in the range 1-2 Ω cm. The metal electrode is Al, of thickness ≈ 1000Å, and with the area in the range 10^{-3} to 10^{-2} cm^2. Typical voltage-time characteristics are exhibited in Figs. 19 and 20, which, again, are direct tracings of photographs of the oscilloscope screen.

Figures 19 (a) and (b) exhibit the V vs t characteristics for SiO_2 on a p-Si substrate. In (a), the Si is in accumulation (gate negative); in (b) the Si is in inversion (gate positive). Figures 20 (a), (b) and (c) correspond to an n-type substrate - (a) to accumulation, (b) and (c) to inversion. The gate area in (b) is double that in (c), and accordingly the breakdown time constant is in (b) approximately twice that in (c). As in Section B, one can use the measured time constants to define equivalent breakdown resistances, obtaining $R_{B,a} \gtrsim 75$ Ω in accumulation, and $R_{B,i} \simeq 1.5K\Omega$ in inversion. In this, as well as all other respects, as regards the voltage-time measurements, the behavior of SiO_2 structures is very similar to that of Al_2O_3 structures. Thus, the time scale for breakdown is about an order of magnitude larger for the inversion case than for the accumulation case, and the fractional voltage drop across the oxide is much larger in the accumulation case, 90- 100%, than for the inversion case, 40-60% (with large fluctuations).

E. C-V Measurements on SiO_2 Structures

Charge storage in the oxide was monitored by C-V measurements as exhibited in Fig. 21 for a p-type substrate, and Fig. 22 for an n-type substrate. The solid lines denote the initial C-V areas, measured before the samples were exposed

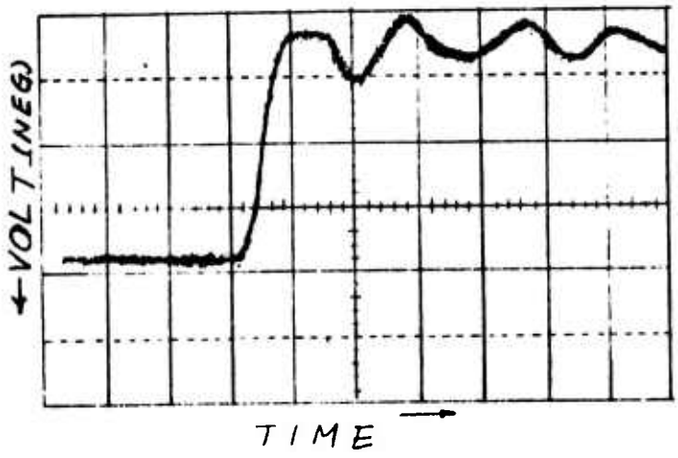

(a) Si IN ACCUMULATION; 50 V/DIV, 20 NANOSEC/DIV., $R_L = 1 M\Omega$

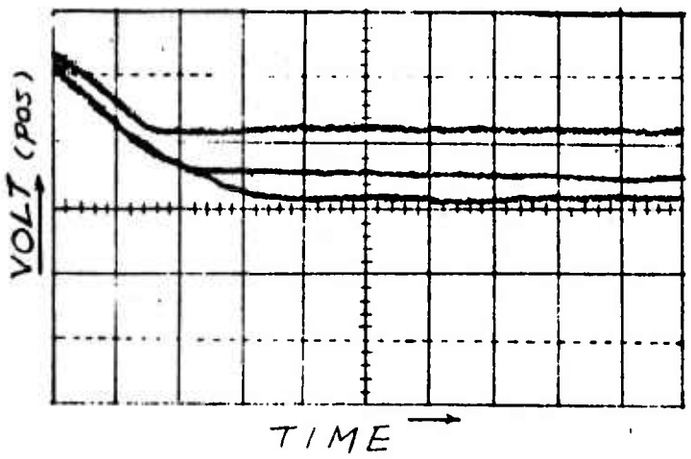

(b) Si IN INVERSION; 50 V/DIV, 0.1 μSEC/DIV., $R_L = 1 M\Omega$

FIG 19. VOLTAGE-TIME CHARACTERISTICS FOR LOCALIZED BREAKDOWN OF Al-SiO_2-Si STRUCTURES (FILM THICKNESS ≃ 2500 Å, p-Si SUBSTRATE)

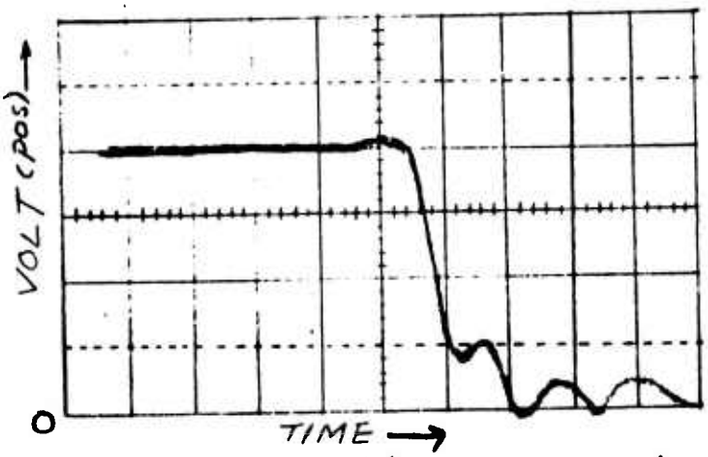

(a) Si IN ACCUMULATION; 50 V/DIV., 10 MILLISEC/DIV.; $R_L = 1\,M\Omega$

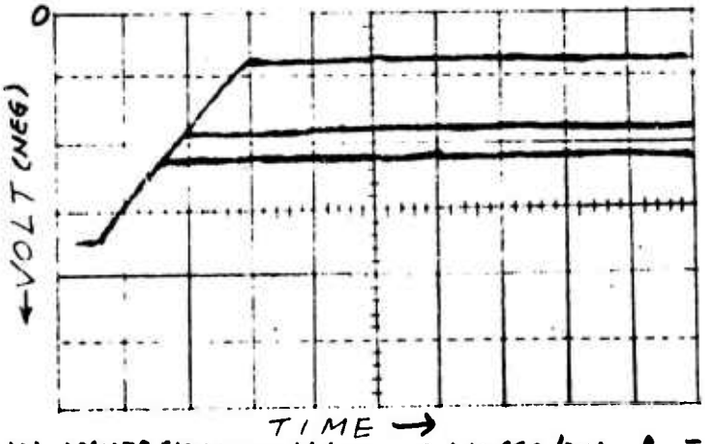

(b) Si IN INVERSION; 50 V/DIV., 0.1 μSEC/DIV., $R_L = 1\,M\Omega$
(GATE AREA = 0.013 cm^2)

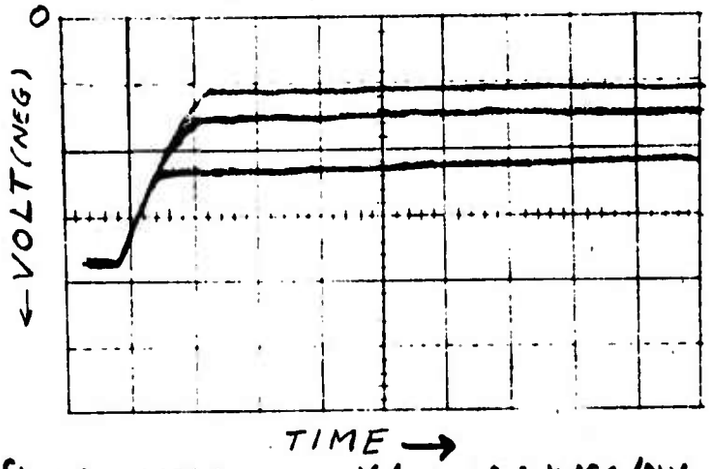

(c) Si IN INVERSION; 50 V/DIV., 0.1 μSEC/DIV, $R_L = 1\,M\Omega$
(GATE AREA = 0.006 cm^2)

FIG. 20. VOLTAGE-TIME CHARACTERISTICS FOR LOCALIZED BREAKDOWN OF Al-SiO_2-Si STRUCTURES (FILM THICKNESS ≃ 2500 Å, n-Si SUBSTRATE)

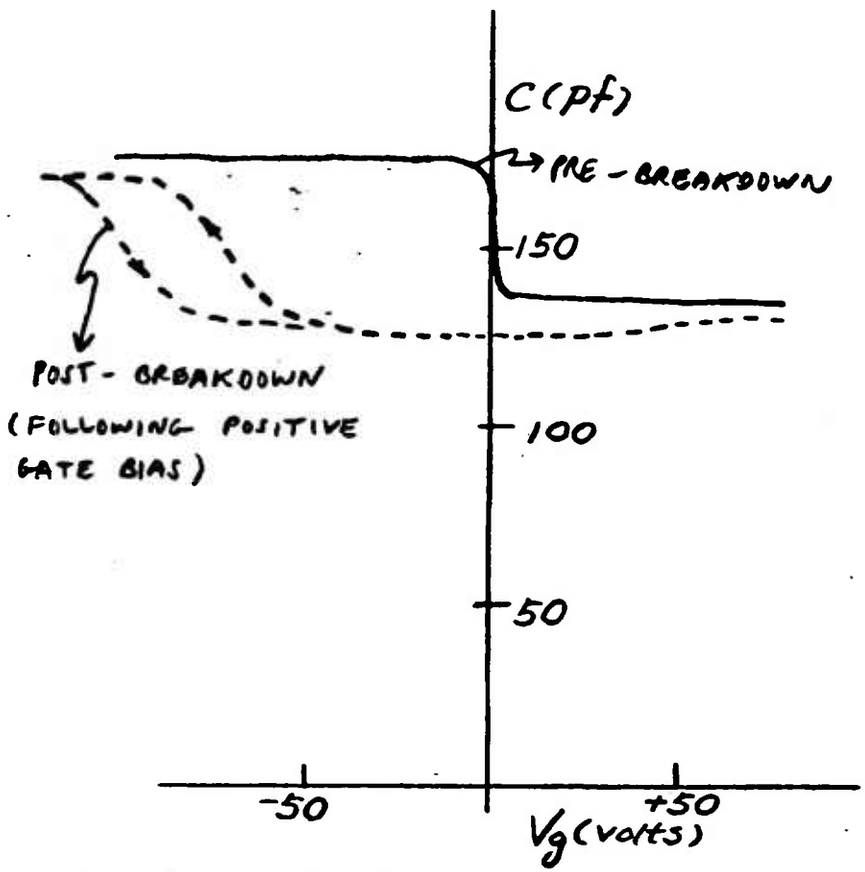

(a) Si IN INVERSION

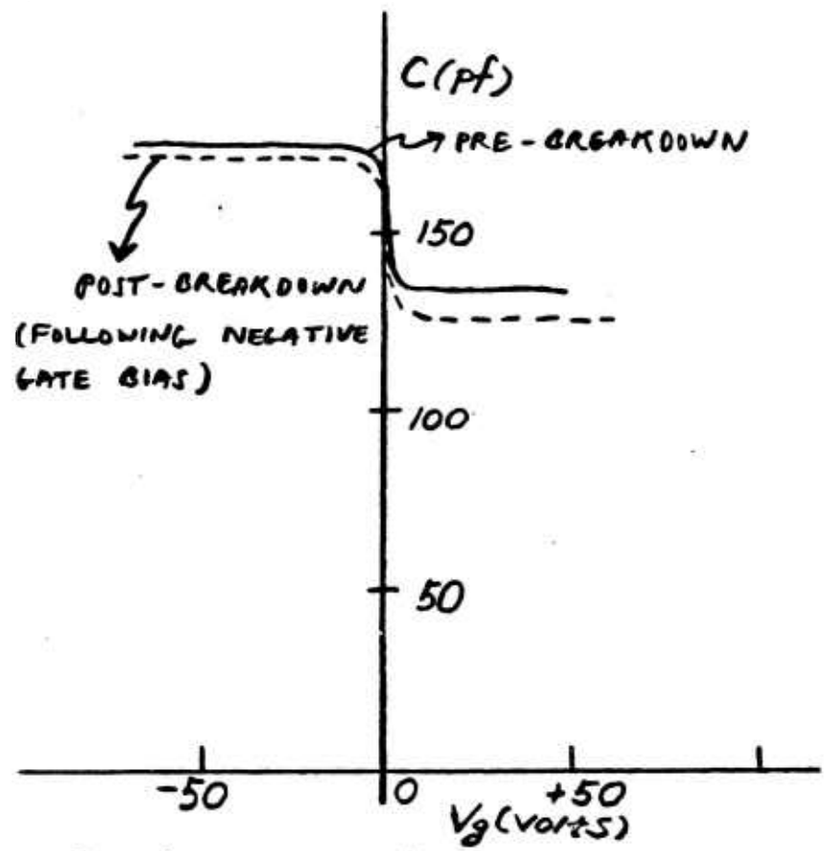

(b) Si IN ACCUMULATION

FIG 21. C-V MEASUREMENTS ON Al-SiO_2-Si STRUCTURES BEFORE AND AFTER BREAKDOWN (AT BOTH SIGNS OF GATE BIAS); p-Si SUBSTRATE

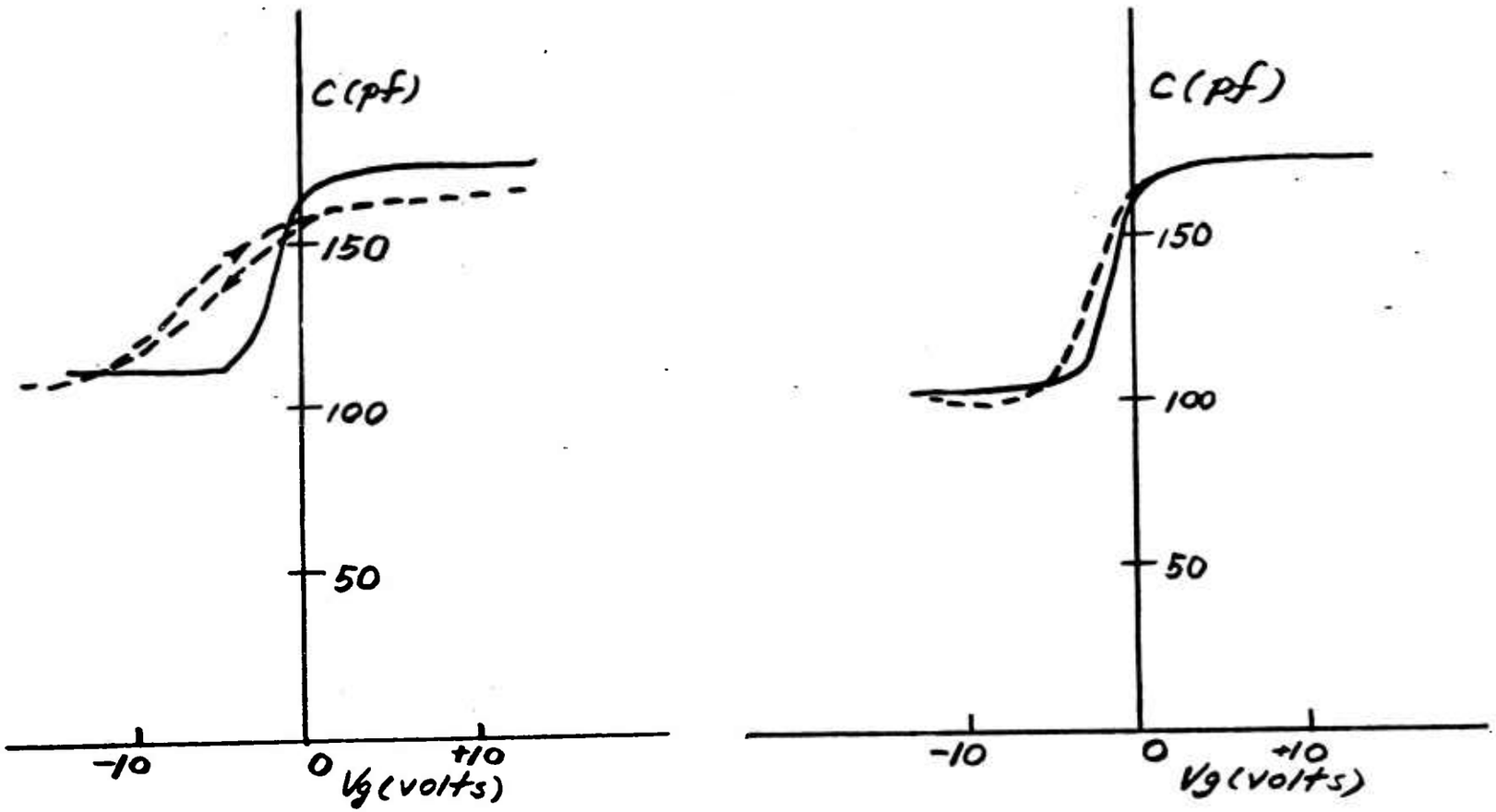

FIG. 22. C-V MEASUREMENTS ON Al-SiO_2-Si STRUCTURES BEFORE AND AFTER BREAKDOWN (AT BOTH SIGNS OF GATE BIAS); n-Si SUBSTRATE

to high fields. THey indicate that there is negligible charge storage prior to the application of the high fields. In Fig. 21(a), the inversion case,it is seen (the dashed curve) that positive gate bias, inducing breakdown, produce a large negative flatband shift of about 70 volts, corresponding to a volume density of positive charge (near the Si interface) $\approx 10^{17}/cm^3$. A substantial distortion of the C-V curve is produced, accompanied by large hysteresis. These striking results are consistent with field-induced tunneling of holes from the Al and their subsequent transport through the oxide and trapping near the interface. (However, based on the corona studies reported in Section 2L, we see that this observation does not, by itself, establish the sign of the dominant carrier in the oxide during breakdown. Further experiments are needed to settle this point). Note that the magnitude of the capacitance is somewhat reduced due to loss of gate area through repeated breakdown events. The magnitude of the nominal breakdown field is 8×10^6 V/cm. In Fig. 21(b), the accumulation case, it is seen (the dashed curve) that negative gate bias leading to breakdown results in no charge storage whatever. This strongly suggests breakdown initiated at the Al gate with the injected electrons as the dominant carriers. For both n- and p-substrates, whether in accumulation or inversion, there is a steady occurrence of breakdown events at the field strength 8×10^6 V/cm, and an onset of such events at $6.6\text{-}7.0 \times 10^6$ V/cm.

Figures 22(a) and (b) exhibit comparable plots for an n-type substrate, (a) corresponding to the gate positive (substrate in accumulation) and (b) to the gate negative (substrate in inversion). Although the gate-positive case does not produce a large flatband shift as in Fig. 21(a), there is very substantial distortion with some hysteresis,evident in the post-breakdown ((dashed) curves of Fig. 22(a), indicating a probably large production of interface states. Figure 22(b) strongly resembles Fig. 21 (b) in that the post-breakdown (dashed) curve is very little changed from the pre-breakdown (solid) curve, indicating negligible charge storage and negligible surface-state production

due to the breakdown.

Studies are also under way of pre-breakdown current flow and charge storage at high fields. With the gate of a p-Si sample held positive at a nominal field of 7.4×10^6 V/cm the current decayed from an initial value of 10^6 A/cm^2 by one order of magnitude over a 24 hour period. Concomitantly, the C-V plots exhibited a slow drift towards negative voltage - a 10 volt shift after 1.5 hours and a 30 volt shift after 24 hours. These pre-breakdown effects are currently being studied systematically.

F. SEM Topographic Studies of SiO_2 Structures

Topographical studies of the local breakdown areas on SiO_2 structures were made in the Princeton SEM, with results for p-type samples exhibited in Figs. 23 and 24. A notable feature which the SiO_2 breakdown spots have in common with the Al_2O_3 breakdown spots, Fig.18, is the existence of an inner core surrounded by a much larger area from which the gate material has been removed. We have already noted the strong polarity dependence of the behavior of the C-V plots, Figs. 21(a) and 22(a) as compared to Figs. 21(b) and 22(b). Polarity dependence also shows up in the SEM photographs. With the gate positive, Figs. 23(a) - (c), the edge of the breakdown area is quite round and very smooth in appearance, as if molten during the course of the breakdown. Figure 23(a) shows a few overlapping spots and 23(b) a single spot. Figure 23(c) exhibits the structure after etch-off of the gate. The inner core of the spot appears vividly exposed as a hole 'burned through' the oxide. For all three photographs of Fig. 23 the total gate area was the same, namely 1.3×10^{-2} cm^2. Figures 24 (a) and (b) exhibit breakdown spots for the opposite polarity, gate negative, and for two different gate areas, 1.3×10^{-2} cm^2 in (a) and 1.3×10^{-3} cm^2 in (b). In both cases, the breakdown areas have a quite different appearance form those seen in Fig. 23 (gate positive). Those in Fig. 24 are smaller and have much rougher edges, as if gate material were either blown

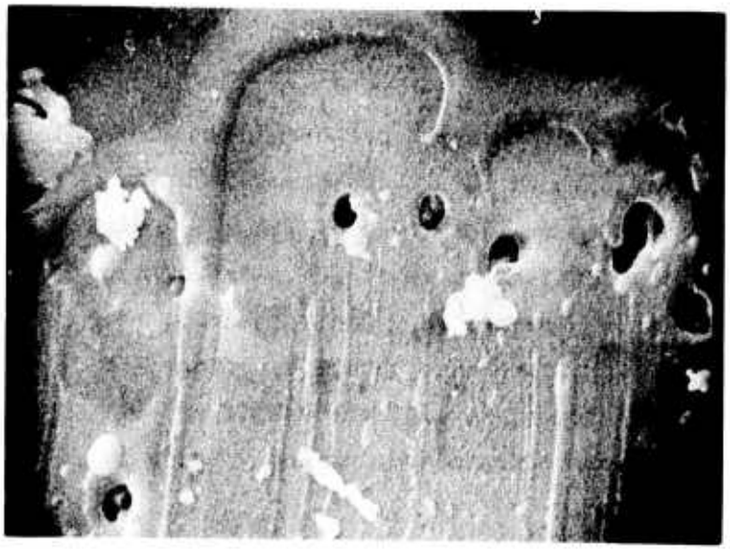

(a) Scan of Gate (5800X)

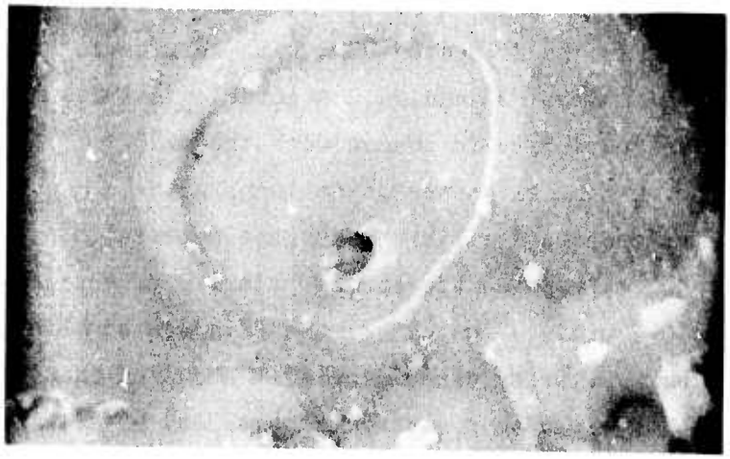

(b) Scan of Gate (5800X)

(c) Scan After Etch-Off of Gate (19,000X)

Fig. 23. SEM Photographs of Localized Breakdown Areas on Al-SiO_2-Si Structures; p-Si Substrate, Gate Positive. (Gate Area = 1.3×10^{-2} cm^2)

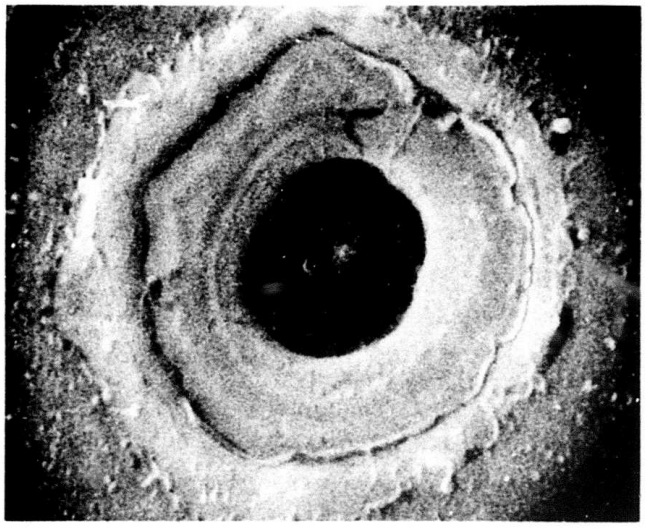

(a) Gate Area = 1.3×10^{-2} cm^2 (58,000X)

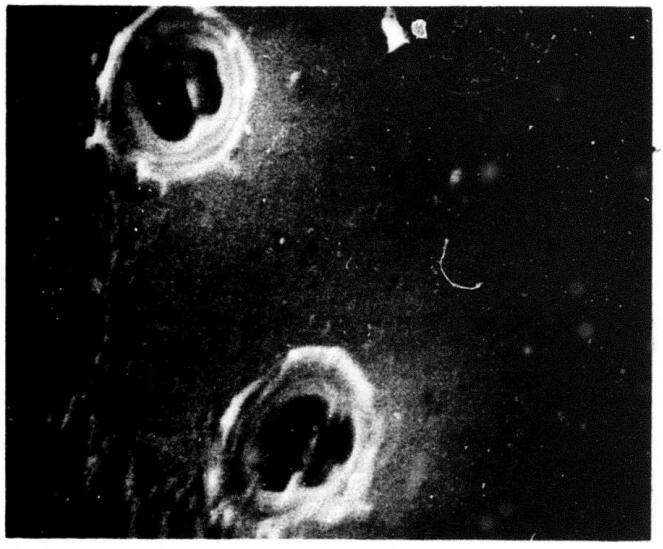

(b) Gate Area = $1.3 \times 10^{-3} cm^2$ (58,000X)

Fig. 24. SEM Photographs of Localized Breakdown Areas on Gate of Al-SiO_2-Si Structures; p-Si Substrate, Gate Negative.

out or exceedingly rapidly quenched from a molten state. The spot in (a) is much larger than either of the two in (b), corresponding to the order-of-magnitude larger gate area in (a), and correspondingly larger stored capacitor energy. The SEM photographs of Figs. 23 and 24 were taken on p-type substrates. With n-type substrates, negative gate voltage (substrate in inversion) produces breakdown spots of exceedingly irregular shape as already noted in the optical photograph of Fig. 18(b). With the oxide completely etched off, penetration of the inner core of the breakdown into a p-Si substrate has been seen in the SEM.

An interesting phenomenon was discovered accidently when four dots on p-type substrates were inadvertently scratched. With positive gate polarity, the breakdowns were clearly initiated along the line of a scratch, whereas with negative gate polarity the scratch appear to have no effect on the spatially random pattern of breakdown spots. These same results were also found to hold for n-type samples. After etch-off of the oxide, no sign of the scratches could be seen on the substrate.

4. Electron-Beam Techniques for Probing the Solid-Solid Interface

A. Background Discussion

When an electron beam strikes a solid surface there are a number of "signal channels" activated which, if properly collected and analyzed, can offer useful analytical information about the sample. These are illustrated schematically in Fig. 25. The electron beam loses energy when passing through a sample by a number of mechanisms. These include plasmon generation, phonon generation, "knock on" damage, and ionization processes, both localized and non-localized in nature. These energy losses limit the range of the electron beam and, at the same time, give rise to analytical information resulting from the relaxation of the absorbed energy. In most of the existing electron-optical installations, provisions are made to gather the information from

SCANNING ELECTRON MICROSCOPE

MODES OF OPERATION

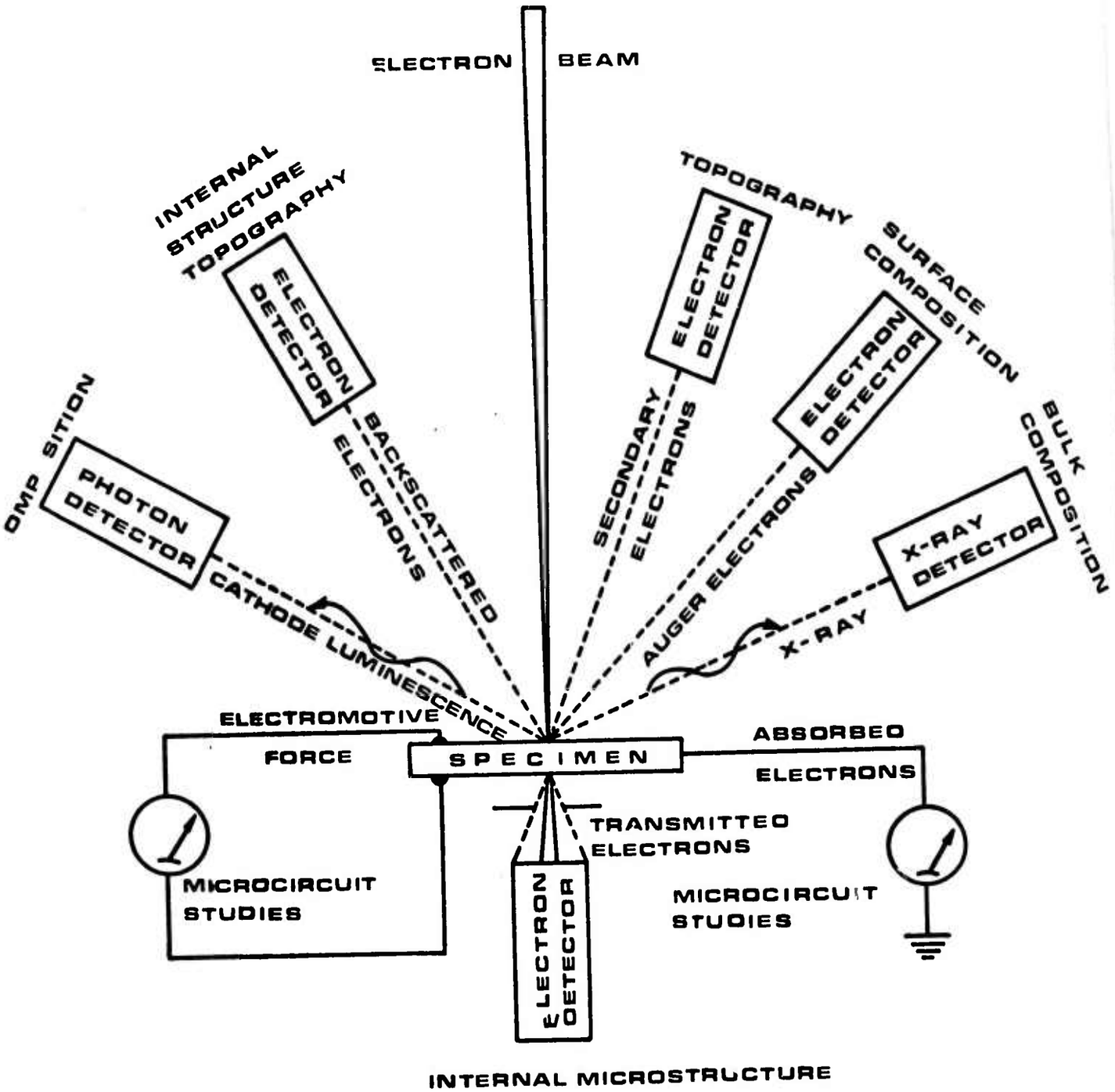

Fig. 25 · SEM MODES OF OPERATION

only one or two of these signal channels. In order to deal in the most efficient way with a particular signal, specialized instruments have been developed such as the Auger electron spectrometer, the electron microprobe, the transmission electron microscope and the scanning electron microscope. The most complete specification of a material can be obtained only by collecting the signal from a maximum number of activated signal channels in one instrument. An electron beam technique has been developed which can probe structure at the interface between a thin insulating film and a semiconductor substrate utilizing the simultaneous collection of signals from more than one signal channel.

B. Differential Detection-Volume Spectroscopy

The information contained in the various signal channels provides analytical data for the volume of material in which a given signal is generated. This volume we will refer to as the "detection volume". It is schematically illustrated in Fig. 26 for a number of signal channels being excited by the same incident electron beam. The exact sizes of the detection volumes for different signal channels depend both on the nature of the specimen under examination and on the beam voltage, which together determine the range of the primary electrons, and the angle of incidence of the incoming electron beam, which determines the surface normal component of that range. The depth to which this detection volume extends can therefore be altered, by changing the pertinent parameters, from a very shallow penetration on the order of a few angstroms to a penetration of several microns. The range R of the electrons in solids can be expressed by the following approximate expression:

$$R = kE_o^n \qquad (23)$$

where k and n are constants for a given material and E_o is the primary beam energy. This expression is accurate to within

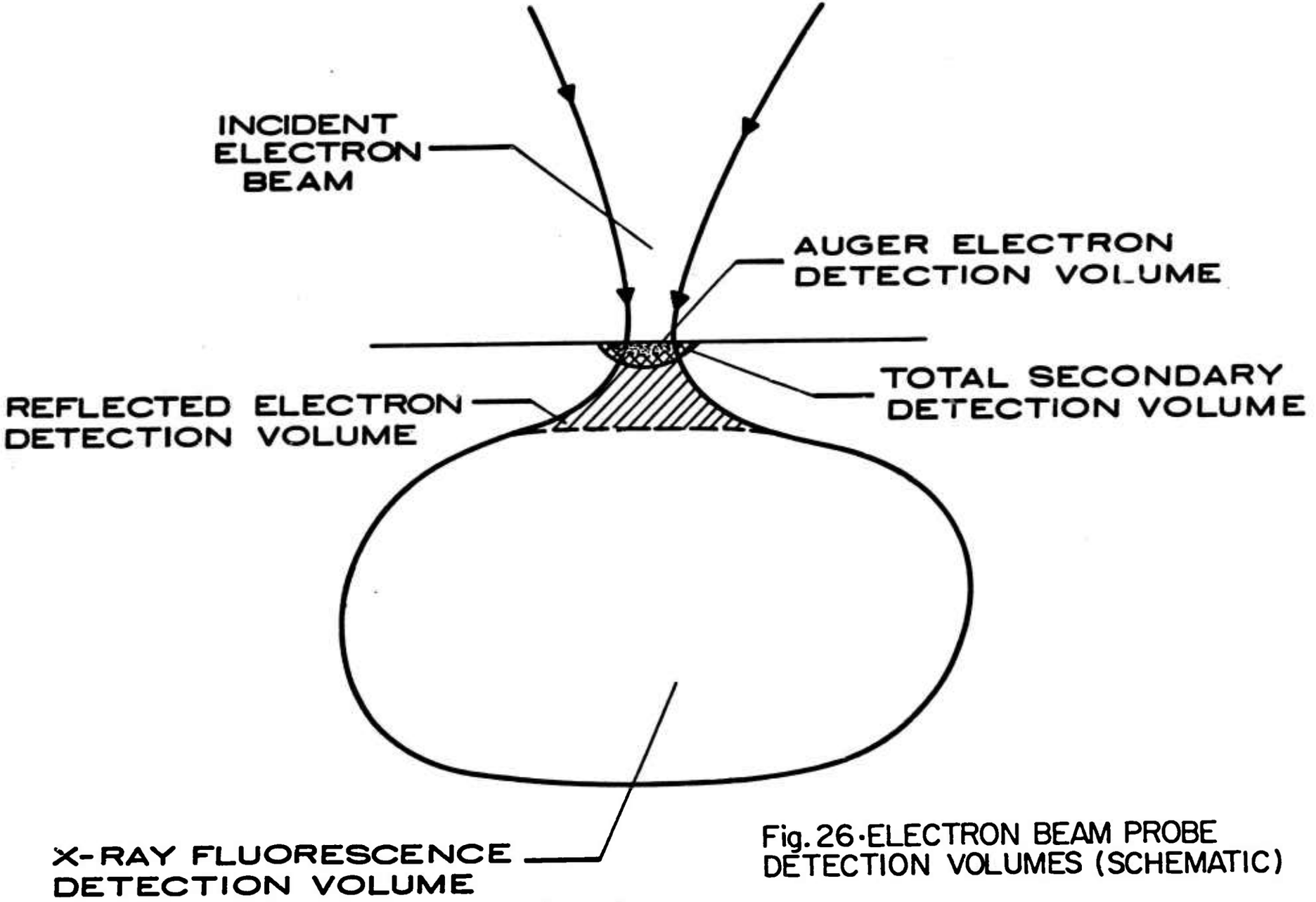

Fig. 26 · ELECTRON BEAM PROBE
DETECTION VOLUMES (SCHEMATIC)

FIG. 26

± 10 per cent in the range of incident energies between 2 and 50 kev for metallic absorbers. It is less accurate for materials of lower electron density. Since the values of n and k are not readily available, and the range of electrons in thin films of varying density is not expected to follow this equation with great accuracy, an alternate method of estimating the range can be used. Assuming that the density of a material is proportional to the volume electron density we may determine a range-density product for a given incident beam energy and then estimate the range for any other material by dividing the product by the appropriate density. Estimates of primary electron range using this range-density product can be made with an accuracy of ± 30%. The errors introduced by the change from one material to another are smaller than those due to the changes in the densities of materials when we are examining thin films. In order to examine the interface between a semiconductor substrate and a thin insulating film we can alter the range of the electrons (and thereby the detection volume) so that the volume sweeps through the interface region. When the detection volume includes part of the interface and substrate regions we may record differences in the signal channels and attribute them to the differences in the material encompassed by the detection volume, i.e., the interface and the substrate. The information gathered in this way is of course an integral of the particular signal channel over the entire detection volume so that the sensitivity, resolution, etc. of the technique are best when the insulating film on the substrate is as thin as possible and there is little, if any, metallization on the sample surface. For an analysis of the interface between an insulating film and its substrate the following measurements are made: 1. The chemical composition of the oxide is determined using X-ray fluorescence with the sample at a high tilt angle. The incident beam voltage must be sufficiently high that the energy levels of interest will be

excited by the beam,and the penetration depth is controlled by using a high angle of incidence so that the electron range normal to the surface is less than the thickness of the oxide. 2. The chemical composition of the interface region and the substrate material is determined using X-ray fluorescence, as above, by decreasing the angle of tilt so that the detection volume includes the interface and part of the substrate region. The spectra are then normalized to those obtained from the insulating film alone (high tilt angle) to determine that portion of the spectra which is due to the material at the interface and in the substrate. A further increase in the penetration will allow some separation of the spectra due to the insulating film and the interface region from that due to the substrate. An example of such a measurement is shown in Fig. 27. While these measurements are not yet quantitative in depth resolution, they offer information about the critical region near the interface which is not available from any other nondestructive technique at this time. Our expectation is that future development of this technique will yield semiquantitative or quantitative results. 3. The structure of the oxide can be probed by using an induced-current mode of imaging where the insulating film is sandwiched between the substrate and a thin metal layer. The secondary emission of the sample at low voltages may charge the specimen either positively or negatively to provide a self-biased induced-current image. As the incident angle, and electron energy, are changed we can form the images by the transport of charge due to the electron-beam-induced carriers at varying depth in the specimen. An example of an image formed in this way is shown in Fig. 28. Figure 28(a) is an image formed with incident electron beam energy of 30 Kev and an incident angle of 30 degrees using the secondary electrons to modulate the intensity. Figure 28(b) is a similar image formed with the same beam energy and incident angle but the induced current signal has been used

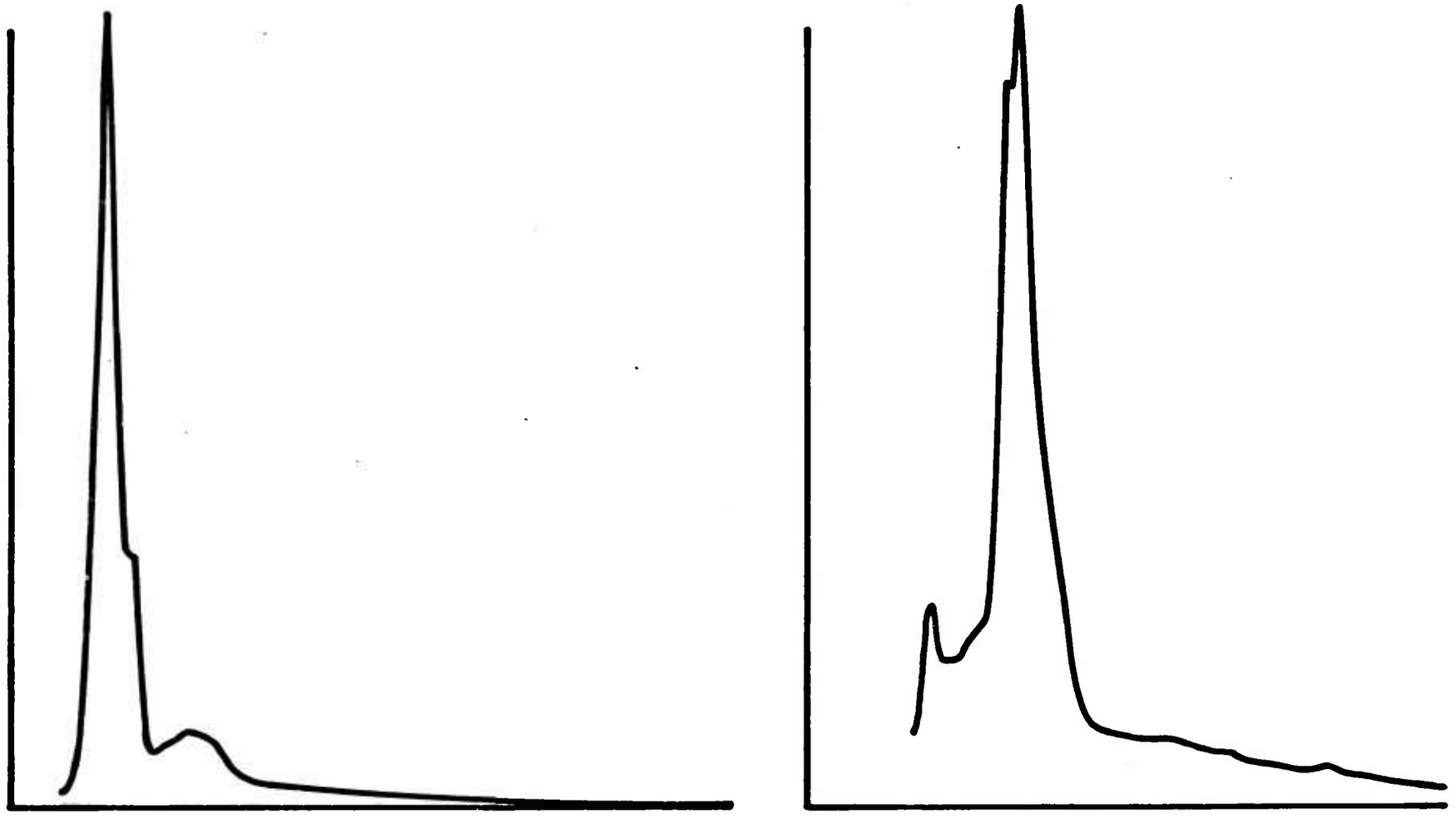

FIG. 27 • X-RAY FLUORESCECE SPECTRA IN A DIFFERENTIAL STUDY

Figure 28(a) Secondary electron image showing surface structure.

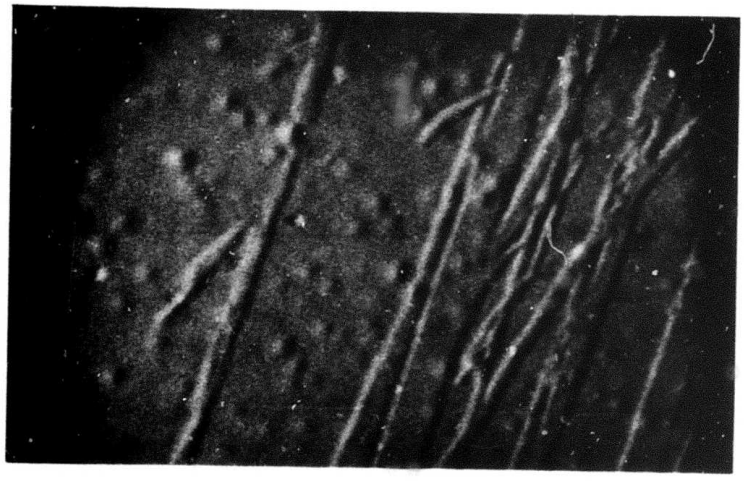

Figure 28(b) Film and interface region imaged with induced current signal. Structure not visible in the surface image (a) above is noted.

Figure 28. SEM secondary electron and induced current images of Al_2O_3 on Si. The beam energy is 30 KV and the incident angle is 30°.

to modulate the image intensity. The electron beam penetration into the oxide, after compensation for the stopping power of the top electrode, is on the order of 1300 angstroms and the impact area of the beam includes the interface region. The structure visible in the induced current image can be attributed to the oxide or interface region since it is not visible in the secondary electron image which has information about the surface layer only. Figure 29 shows a lower magnification of the same area. In Figure 29(a), a secondary electron image, taken with a beam energy of 15 Kev, the striations on the surface of the sample are visible as in Figure 28. Figure 29(b) shows that at lower accelerating voltages the lateral nonuniformities in the charge stored at the interface and in the oxide region can be imaged using the induced current signal. Spatial resolution on the order of 200 Å is obtainable with this technique. Although interpretation of these images is not yet well understood, they offer a method of observing the structure at the interface which has not yet been exploited, and work is currently underway to quantify this method for the study of thin insulating layers on semiconducting substrates.

5. Charge-Discharge Studies of Electron-Trappling in Al-Implanted SiO_2* (Noble Johnson collaborating)

A. Background Discussion and Summary

It is a well-known property of clean, thermally grown SiO_2 films on Si that they are relatively free of electron traps. In consequence, electrons are easily removed from the oxide at high electric fields, there generally being no impediment to their egress at the oxide interface with either the silicon substrate or the gate. On the other hand, holes are very strongly trapped in the oxide, either throughout the bulk or at

*Work supported in part, also, by ONR under Contract N00014-67-A-0151-0035

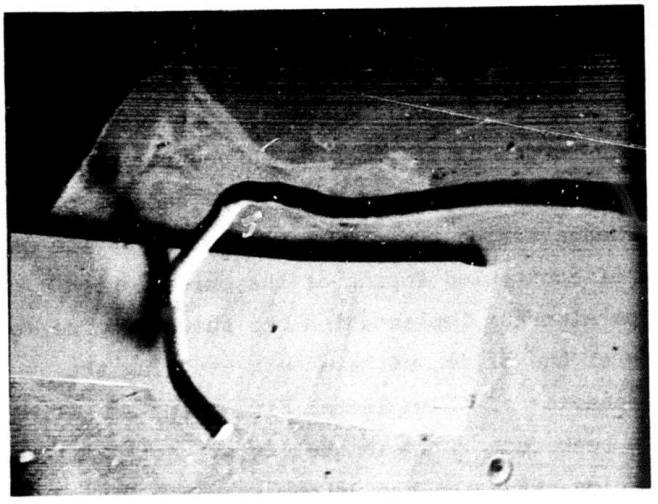

Figure 29(a) Secondary electron image showing surface structure.

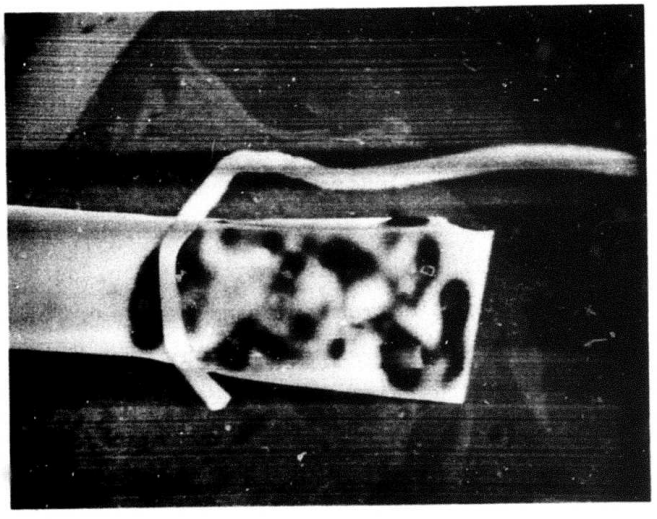

Figure 29(b) Film and interface region imaged with induced current signal. Two-dimensional charge distribution is visible.

Figure 29. SEM secondary electron and induced current images of Al_2O_3 on Si. The beam energy is 14 Kev and the incident angle is 40°.

the SiO_2-Si interface. The very weak trapping of electrons and the very strong trapping of holes is almost certainly the origin of the radiation sensitivity of SiO_2 films on Si. One logical approach to radiation-hardening of the SiO_2 is controlled doping of the oxide in such a manner as to produce large numbers of electron traps and hence strong trapping of electrons in the oxide. A convenient means of controlled doping of the oxide is ion implantation. Since aluminum implantation has shown promise for radiation hardening of the oxide, we have been studying the electron-trapping behavior of Al-implanted SiO_2 films on silicon by charge-discharge techniques. These studies are not concerned directly with radiation-hardness, but rather with the fundamental electronic behavior of SiO_2 as modified by the implantation-doping with Al. A brief, preliminary report of these studies was given in the First Semiannual Technical Report. A more extensive report is presented here.

The experiments have conclusively demonstrated that unannealed aluminum-implanted SiO_2 possesses electron traps not found in the undoped material. Optical excitation of trapped electrons indicates that the traps are located in the lower half of the forbidden energy gap of SiO_2. A model of electron trapping has been formulated which illustrates the dynamic features of the trapping process and correctly predicts the time dependence of the flat-band voltage and photocurrent during electron photoinjection. Application of this model to the experimental results indicates that essentially all of the photoinjected electrons are trapped in the oxide. An analytical solution of the rate equations has been obtained by suitable approximations.

B. Experimental Procedure and Results

The samples used were MOS structures in which the oxide layer was grown to a thickness of 1400 Å in dry oxygen on the (100) face of a 3 Ω-cm n-type silicon wafer. The oxide of the test samples was implanted with 20 keV aluminum ions to a fluence of 10^{14} cm^{-2}. A control sample was not implanted. The profile of the implanted aluminum ions has been published elsewhere.[12]

Semi-transparent gold field plates were vacuum deposited on the exposed oxide surface. The implanted samples, as received (unannealed), showed a flat-band voltage typically of -15 volts (see curve labelled 1 in Fig. 5 of the First Semiannual Report).

An initial exposure of the implanted samples to UV light with the contacts short-circuited reduced the flat-band voltage approximately to zero. After this optical annealing, a positive voltage was applied to the gate and the sample was exposed to 4.77 eV photons from a high-intensity monochromator. This exposure induced an internal photo-emission of electrons from the silicon into the oxide. Up to the highest applied voltage, 35 volts, no steady-state current could be observed, only a transient current which always decayed to zero. Following the current decay, C-V measurements, made at 1 MHz, showed a positive flat-band voltage, indicating negative charge storage, with the magnitude of the flat-band voltage being essentially equal to the applied gate voltage. The flat-band voltage could then be reduced approximately to zero by either optical or thermal annealing with the contacts short-circuited. Optical annealing required photon energies greater than about 4.6 eV. Thermal annealing could be accomplished at temperatures below 350°C. This experiment was repeated, with reproducible results, over the entire range of gate voltages.

In marked contrast with the foregoing results obtained with Al-implanted samples, the non-implanted control sample, when subjected to the same experiment, showed no detectable storage of negative charge and the photo-induced current showed no signs of decaying over a long period of time.

The dynamics of the negative charging of the Al-implanted samples were investigated by shutting the light off, and so interrupting the photoinjection at intervals during the charging process, and measuring the C-V curve. The resulting time evolution of this curve for a gate voltage of 10 volts is shown in Fig. 30. In Fig. 31(a) is shown a plot of $V_g - V_{FB}$ vs. time, where V_g is the gate voltage and V_{FB} is the flat-band voltage.

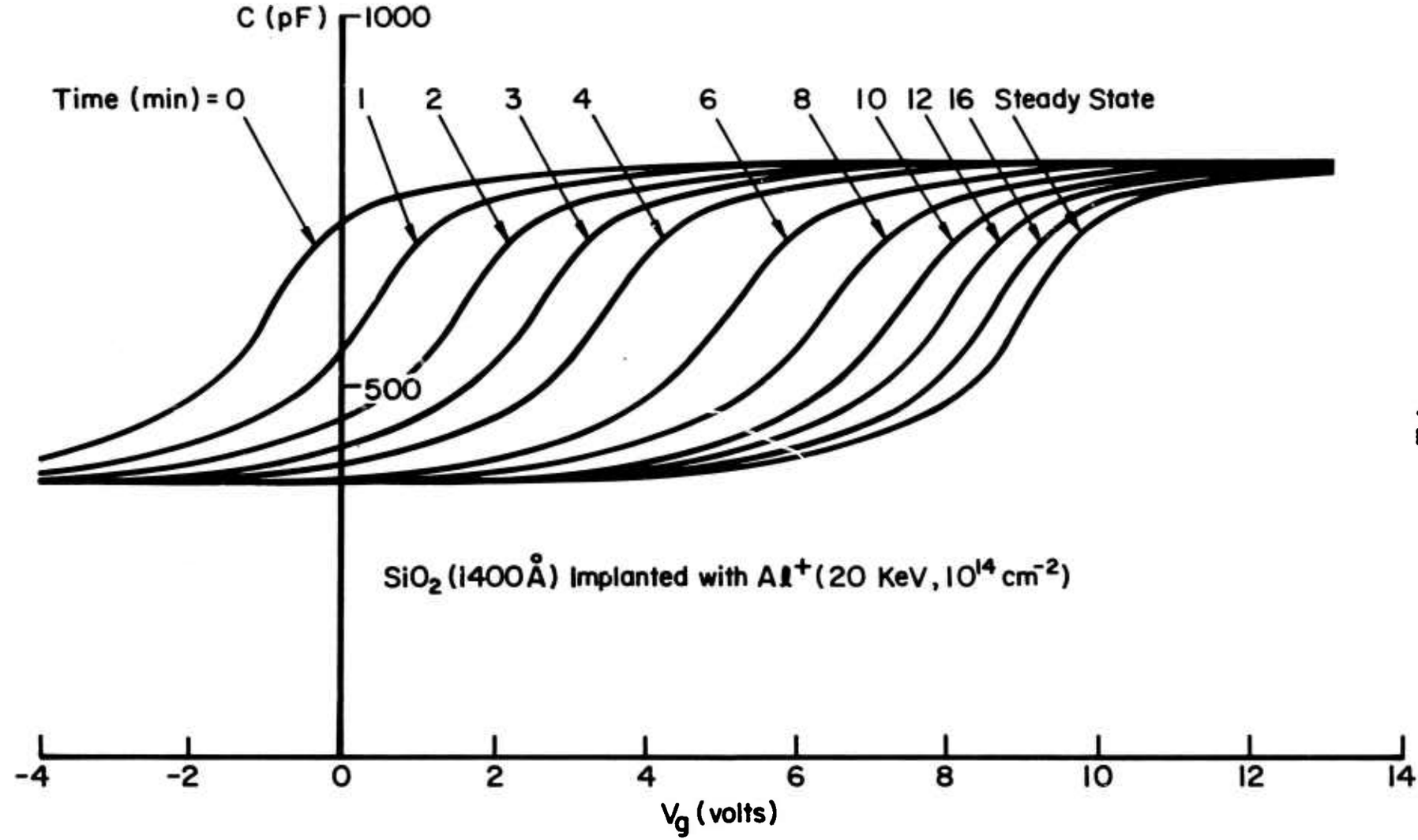

Fig. 30. Shift of the C-V Curve with Time During Electron Photoinjection with $V_g = 10$ volts

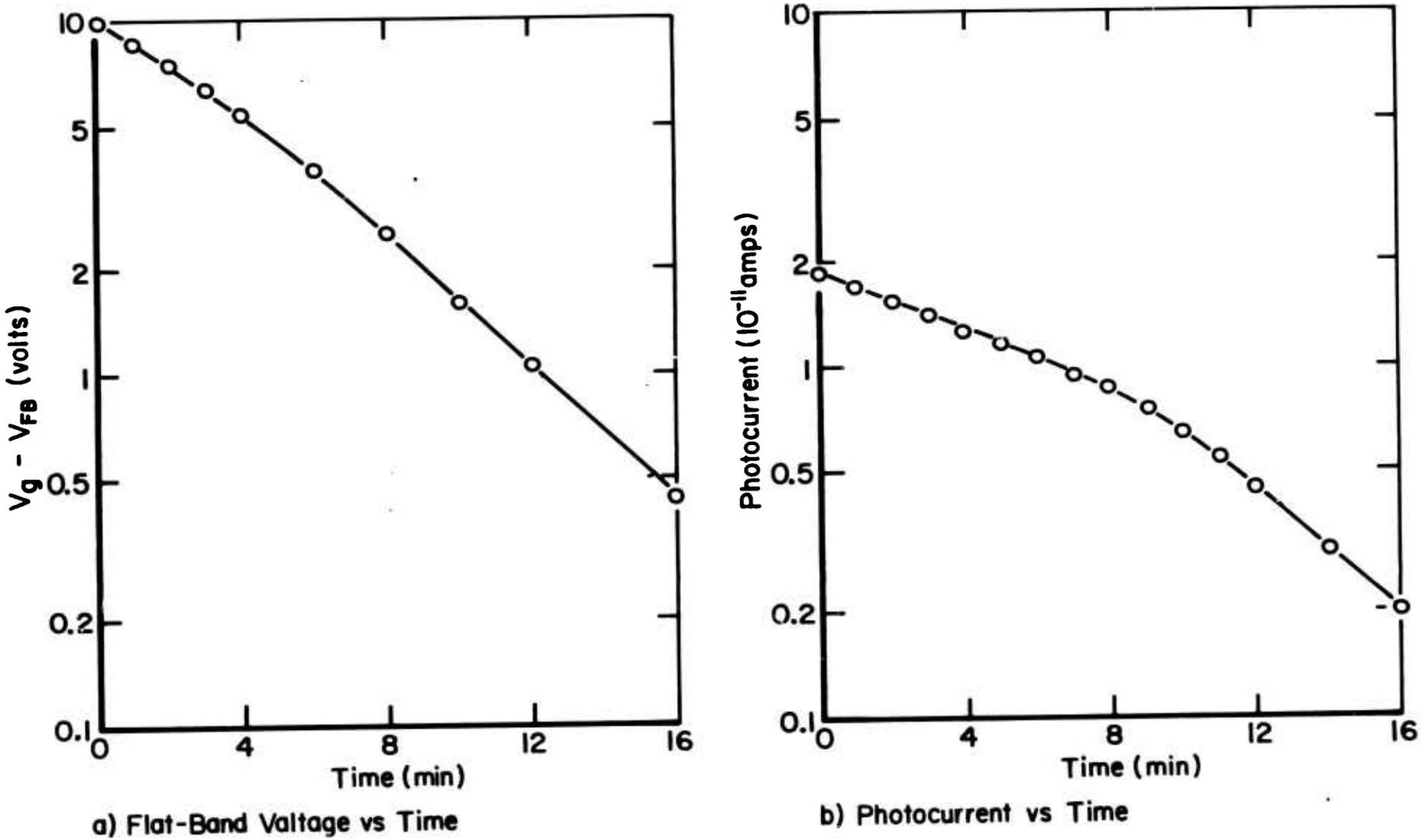

Fig. 31. Time-Dependent Behavior of Sample During Electron Photoinjection with V_g = 10 Volts [SiO_2 (1400 Å) Implanted with Al^+ (20 KeV, $10^{14}cm^{-2}$)]

The corresponding photocurrent, as measured in the external circuit, is shown in Fig. 31(b). Similar results were obtained for all other gate voltages used in the study.

A straightforward interpretation of the above-described results is as follows: The aluminum implantation into the SiO_2 created deep electron traps in the insulator. Electrons photoinjected into the insulator were captured into these traps, building up a negative space charge which gradually reduced the electric field at the Si-SiO_2 interface to zero, concomitantly reducing the injected photocurrent to zero. The trapped negative charge shifts the flat-band voltage in the positive direction, and a shift in flat-band voltage equal to the applied gate voltage corresponds to the reduction in electric field at the interface to zero. In the next section we present a model of electron trapping which correctly predicts the time dependence of V_{FB} and of the photocurrent measured in the external circuit during electron photoinjection. The shapes of the curves in Figs. 31(a) and (b) reflect the dependence of the photoinjected current on the intensity of the electric field at the Si-SiO_2 interface.[13] A tentative conclusion resulting from application of the model to the data of Figs. 31(a) and (b) is that essentially all of the photoinjected electrons are trapped in the oxide, the measured gate current being almost entirely caused by displacement current in the oxide. In this connection it should be noted that at the largest gate voltage used in our experiments, namely 35 volts, the number of trapped charges was approximately 10^{13} cm^{-2} in the steady state, whereas the number of implanted aluminum atoms was an order of magnitude greater than this. The indicated position of the centroid of the space-charge distribution of trapped charge was approximately 620 Å from the metal-oxide interface.

C. Analysis and Numerical Results

In this section we examine two aspects of the experimental results: first, we analyze the relationships between the

steady-state magnitudes of photoemitted, trapped, and externally measured charge, and show by comparison with the known aluminum impurity profile that it is likely that all of the photoemitted electrons were trapped in the oxide; then we analyze the time evolution of the flat-band voltage and the externally measured current during the trap-charging transient.

i) Steady-State Analysis

The total charge photoinjected into the oxide at the Si-SiO_2 interface, Q_{inj}, can be expressed as the sum of two components: the charge trapped in the oxide, Q_{ox}, and the charge that is drifted completely through the oxide and into the metallic gate, Q_{thru}. Thus:

$$Q_{inj} = Q_{ox} + Q_{thru} \quad . \tag{24}$$

The charge that has been transported through the external circuit, on the other hand, consists of the sum of the conduction-current component Q_{thru} and a displacement-current component which is equal to Q_{ox} weighted by the factor $1 - \bar{x}/L$, where $\bar{x}$ is the distance from the Metal-SiO_2 interface to the centroid of the steady-state distribution of trapped charge and L is the thickness of the oxide, i.e.:

$$Q_{ext} = (1 - \frac{\bar{x}}{L})Q_{ox} + Q_{thru} \quad . \tag{25}$$

Finally, the change in flatband voltage caused by Q_{ox} is given by

$$\Delta V_{FB} = \frac{\bar{x}}{\varepsilon} Q_{ox} \quad , \tag{26}$$

where ε is the absolute dielectric constant of the oxide.

By elimination of the quantity Q_{ox} between Eqs. (25) and (26) we obtain the following expression for the ratio of the through-going charge to the charge measured in the external circuit:

$$\frac{Q_{thru}}{Q_{ext}} = 1 - \frac{\varepsilon \Delta V_{FB}}{Q_{ext} L} \left(\frac{L}{\bar{x}} - 1\right) \quad . \tag{27}$$

By elimination of Q_{ox} and Q_{thru} between Eqs. (24), (25), and (26), we obtain an expression for the ratio of the charge trapped in the oxide to the total photoinjected charge:

$$\frac{Q_{ox}}{Q_{inj}} = \frac{L/\bar{x}}{Q_{ext} L/\varepsilon \Delta V_{FB} + 1} \quad . \tag{28}$$

We now apply the foregoing relationships to the data of the present experiment. By integration of the data for current given in Fig. 31(b) we find $Q_{ext} = 2.9 \times 10^{-7}$ coulomb/cm^2. Using $L = 1.4 \times 10^{-5}$ cm, $\Delta V_{FB} = 10$ volts, and a relative dielectric constant of 3.8 for the oxide, we can plot the ratios given by Eqs. (27) and (28) as functions of the ratio $\bar{x}/L$. The results are shown in Fig. 32, together with a graph of the aluminum impurity profile.[12]

Inasmuch as Q_{ox}/Q_{inj} cannot exceed unity, and Q_{thru} cannot be negative, the results plotted in Fig. 32 show that the centroid of steady-state charge distribution is restricted to the range $0.45 \leq \bar{x}/L \leq 1$. Furthermore, the tail of the aluminum impurity profile to the right of $\bar{x}/L = 0.45$ contains only about one-tenth of the total number of implanted Al atoms. If we assume that the location of the centroid is somewhat to the right of $\bar{x}/L = 0.45$, say at $\bar{x}/L = 0.6$, we must suppose that the implantation-related traps caused by fewer than 10^{13} cm^{-2} impurity atoms were able to capture three-fourths of the electrons ($Q_{ox}/Q_{inj} \approx 0.75$) while the traps on the left, which were the result of an order-of-magnitude greater number of impurity atoms, were unable to capture the remaining 25 percent of the carriers. This argument makes it appear highly likely that essentially every emitted electron was captured, and that the location of the centroid of charge distribution in the final steady state was at $\bar{x}/L = 0.45$.

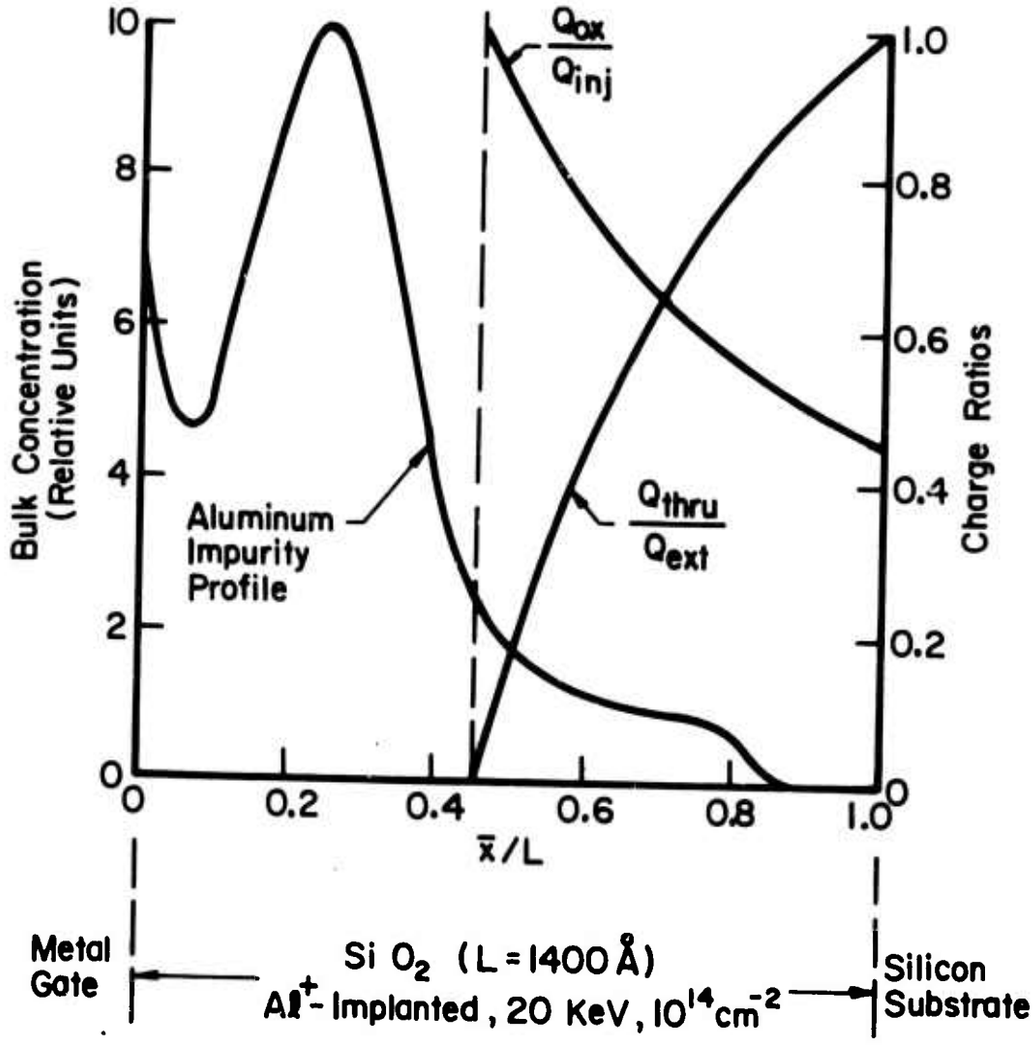

Fig. 32. Plots of Relative Trapped Charge and Relative Transmitted Charge vs the Relative Trapped-Charge Centroid Position. Also Plotted is the Implanted Aluminum Profile (Ref. 12).

ii) Transient Analysis

We next analyze the dynamics of the trap-charging process, assuming that the location of the centroid of trapped charge distribution is not a function of the time. This assumption is made purely for mathematical convenience; its relationship to the ongoing physics is discussed below. When a positive voltage is impressed on the gate of the MOS structure and electrons are photoemitted from the Si into the SiO_2 by means of optical excitation, the injected current is a function of the electric field intensity at the Si-SiO_2 interface.[13] The dependence of photocurrent on electric field intensity for our samples, using photons of 4.77 eV energy, is shown in Fig. 33. (This relationship was obtained by measurements made on our unimplanted control sample, in which sample charging was shown to be negligible.) As the traps in the implanted sample capture electrons, the electric field intensity at the interface, $\mathcal{E}_i$, is gradually reduced toward zero, thus diminishing the photoinjected current; meanwhile the trapped negative charge increases the flatband voltage in the positive direction. The process ceases when the electric field in the oxide at the interface is reduced to zero, at which point, assuming negligible fixed charges in interface states, the bands in the semiconductor are flat; i.e., the flatband voltage has been brought to the value of the gate voltage.

Neglecting the effects of fixed charge at the Si-SiO_2 interface, the flatband voltage of the MIS structure can be written as

$$V_{FB}(t) = \phi_{ms} - \frac{1}{\epsilon} \int_0^L x\, \rho_{ox}(x,t)\, dx \quad , \quad (29)$$

where ϕ_{ms} is the metal-semiconductor work-function difference, ρ_{ox} is the charge density in the oxide, and x is measured from the metal-insulator interface. The total charge per square centimeter, Q_{cx}, is

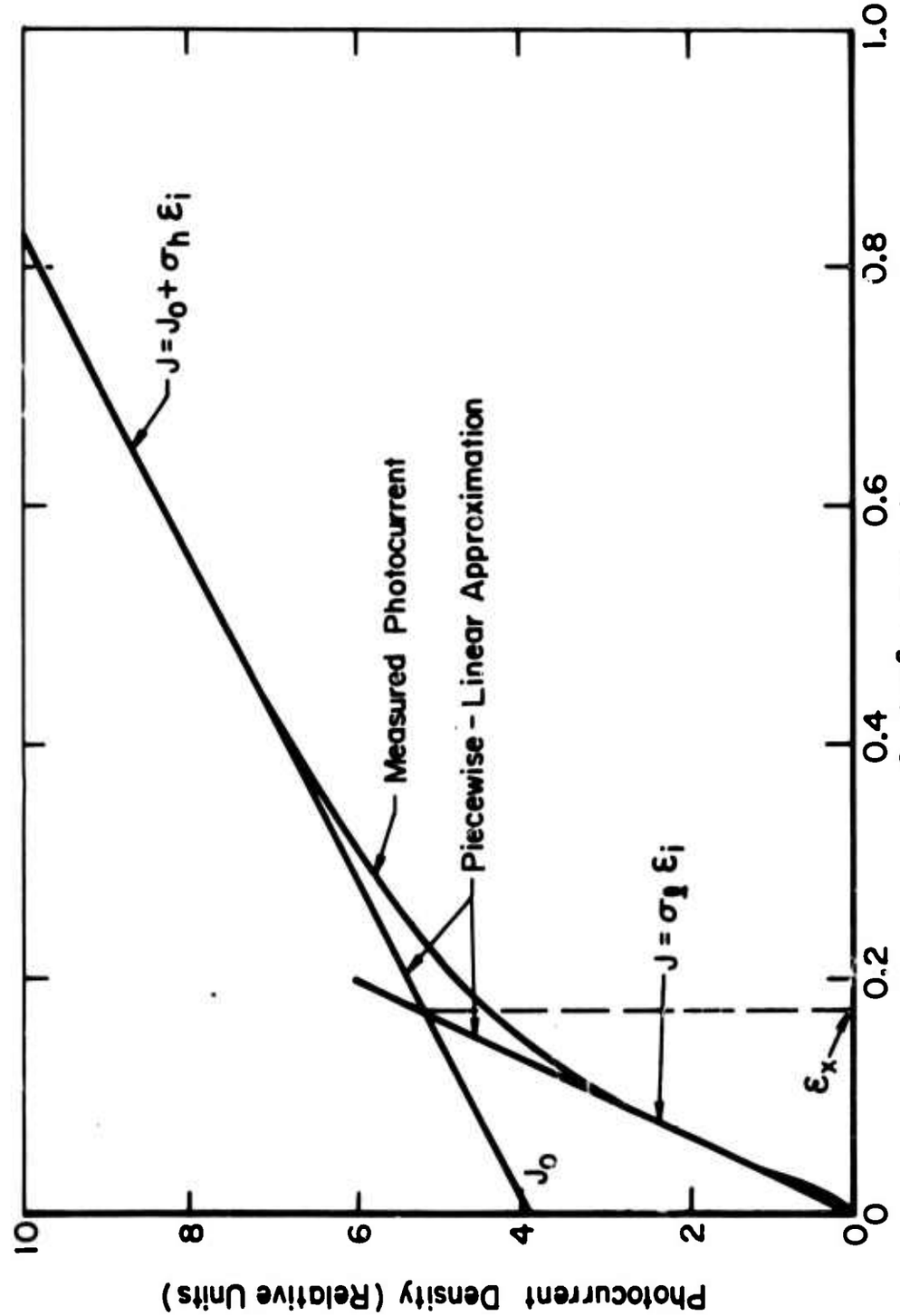

Fig. 33. Field-Dependence of the Electron-Current Photoinjected from the Si into the SiO_2 ($\mathcal{E}_i$ is the Electric Field at the Interface)

$$Q_{ox}(t) = \int_0^L \rho_{ox}(x,t)\, dx \quad . \tag{30}$$

The centroid of the charge distribution is defined by:

$$\bar{x} = \frac{\int_0^L x\, \rho_{ox}(x,t)\, dx}{\int_0^L \rho_{ox}(x,t)\, dx} \quad , \tag{31}$$

or by use of (30):

$$\bar{x} = \frac{1}{Q_{ox}} \int_0^L x\, \rho_{ox}(x,t)\, dx \quad . \tag{32}$$

Using (32), we can write (29) as

$$V_{FB}(t) = \phi_{ms} - \frac{\bar{x}}{\epsilon} Q_{ox}(t) \quad . \tag{33}$$

Thus, the effect of the distributed charge in the oxide is the same as would be produced by a sheet of charge of magnitude Q_{ox} located at the position of the centroid of the distribution. As was mentioned previously, we shall assume for simplicity of analysis that the location of the centroid is independent of the time. Assuming also that all of the photoinjected charge is trapped in the oxide, we have the following relation:

$$\frac{dQ_{ox}}{dt} = J_{inj} \quad , \tag{34}$$

where J_{inj} is the density of the photoinjected current. This current is a function of the electric field intensity in the oxide at the $Si\text{-}SiO_2$ interface, $\mathcal{E}_i$, in the manner shown in Fig. 33. For the field intensity we can write

$$\mathcal{E}_i(t) = \frac{1}{L}\left[V_g - \phi_{ms} - \phi_s + \frac{\bar{x}}{\varepsilon} Q_{ox}(t)\right] , \qquad (35)$$

where V_g is the gate voltage and ϕ_s is the surface potential of the semiconductor. The current measured in the external circuit, J_{ext}, is given by

$$J_{ext}(t) = (1 - \bar{x}/L) J_{inj}(t) \quad . \qquad (36)$$

An analytical solution can be obtained by using a piecewise-linear approximation to the photoinjected current as a function of electric field intensity, in the manner shown in Fig. 33. The use of two straight lines divides the field dependence into a high-field regime and a low-field regime, with the intersection of the two linear segments defining a transition field $\mathcal{E}_x$. Hence the photocurrent density may be written as

$$J_{inj} = \begin{cases} J_o + \sigma_h \mathcal{E}_i , & \mathcal{E}_i \geq \mathcal{E}_x \quad \text{(High-field Regime)}, \\ \sigma_\ell \mathcal{E}_i , & \mathcal{E}_i \leq \mathcal{E}_x \quad \text{(Low-field Regime)} , \end{cases} \qquad (37)$$

where J_o is the intercept of the high-field linear segment, and σ_h and σ_ℓ are the slopes of the high- and low-field segments, respectively. For simplicity the metal-silicon work function difference and the surface potential of the semiconductor are neglected in comparison with the gate voltage. From Eq. (35) $\mathcal{E}_i$ depends only on the applied gate bias and the trapped charge Q_{ox}. From Eq. (33), V_{FB} depends only on Q_{ox}. Then for an initial flat-band voltage of zero the initial condition for the total charge is $Q_{ox}(0) = 0$. Thus, Eq. (34) can be solved to yield $Q_{ox}(t)$ which when substituted into Eqs. (35) and (37) yields $J_{inj}(t)$. Then $V_{FB}(t)$ and $J_{ext}(t)$ are obtained from Eqs. (33) and (36), respectively. The following results are then obtained:

High-Field Regime, $t \leq t_x$:

$$V_{FB}(t) = (V_g + \frac{J_o L}{\sigma_h})(1 - e^{-t/\tau_h}) \quad , \tag{38}$$

$$J_{ext}(t) = (1 - \frac{\bar{x}}{L})(J_o + \sigma_h \frac{V_g}{L}) e^{-t/\tau_h} \quad , \tag{39}$$

$$\tau_h = \frac{\varepsilon L}{\sigma_h \bar{x}} \quad . \tag{40}$$

Low-Field Regime, $t \geq t_x$:

$$V_{FB}(t) = V_g - \mathcal{E}_x L \, e^{-(t - t_x)/\tau_\ell} \quad , \tag{41}$$

$$J_{ext}(t) = (1 - \frac{\bar{x}}{L}) \, \sigma_\ell \, \mathcal{E}_x e^{-(t - t_x)/\tau_\ell} \quad , \tag{42}$$

$$\tau_\ell = \frac{\varepsilon L}{\sigma_\ell \bar{x}} \tag{43}$$

The quantity t_x is defined as that instant of time when $\mathcal{E}_i = \mathcal{E}_x$.

Note that Eqs. (39) and (42) yield a linear dependence of $\ell n(J_{ext})$ on time in each field regime, in agreement with the experimental results, Fig. 31(b).

The experimental results presented in Figs. 31(a) and (b) furnish the following numerical values for parameters appearing in the analytical solutions:

$$J_{ext}(0) = 5.9 \times 10^{-10} \text{ amps/cm}^2$$

$$J_{ext}(t_x) = 2.4 \times 10^{-10} \text{ amps/cm}^2$$

$$t_x = 5.7 \times 10^2 \text{ sec.}$$

$$\tau_h = 6.3 \times 10^2 \text{ sec.}$$

$$\tau_\ell = 2.9 \times 10^2 \text{ sec.}$$

In order to make a self-consistency check with the results quoted earlier in this section, where the location of the final steady-state centroid of charge distribution was deduced to be at $\bar{x}/L = 0.45$, we can use Eqs. (39) and (40) to obtain the following expression for $\bar{x}$ (as obtained from our transient data):

$$\frac{\bar{x}}{L} = 1 - \left[1 + \frac{\epsilon V_g}{\tau_{Vo} L J_{ext}(0)}\right]^{-1} , \tag{44}$$

with

$$\frac{1}{\tau_{Vo}} = \frac{1}{\tau_h}\left(1 + \frac{J_o L}{\sigma_h V_g}\right) \tag{45}$$

Substitution of the above-listed numerical values (and also $\tau_{Vo} = 4.3 \times 10^2$ sec) into Eq. (44) yields the result $\bar{x}/L = 0.49$, which is only slightly in excess of the value of 0.45 which was deduced from the steady state analysis (Fig. 32). It is to be expected that the value of $\bar{x}$ deduced from the transient analysis should, if anything, be larger than that obtained in the steady state, for, as the traps charge, the centroid of charge distribution should move away from the Si-SiO_2 interface and toward the metal gate; thus the mean value of $\bar{x}$ during the transient should be larger than the final value. The discrepancy between the two values of $\bar{x}$ is small and the difference is in the expected direction; thus we regard the results to be satisfactorily self-consistent.

6. Electron-Beam Injection and Damage Studies* (C.T. Shih collaborating)

A. Background Discussion

In the initial studies with the electron beam, summarized in the First Semiannual Technical Report, we were concerned primarily with the properties of the beam-induced I-V characteristic of the oxide. Typical results of this phase of the study are presented in Figs. 34(a) and (b). There is

*Work supported in part, also, by ONR under Contract N00014-67-A-0151-0030

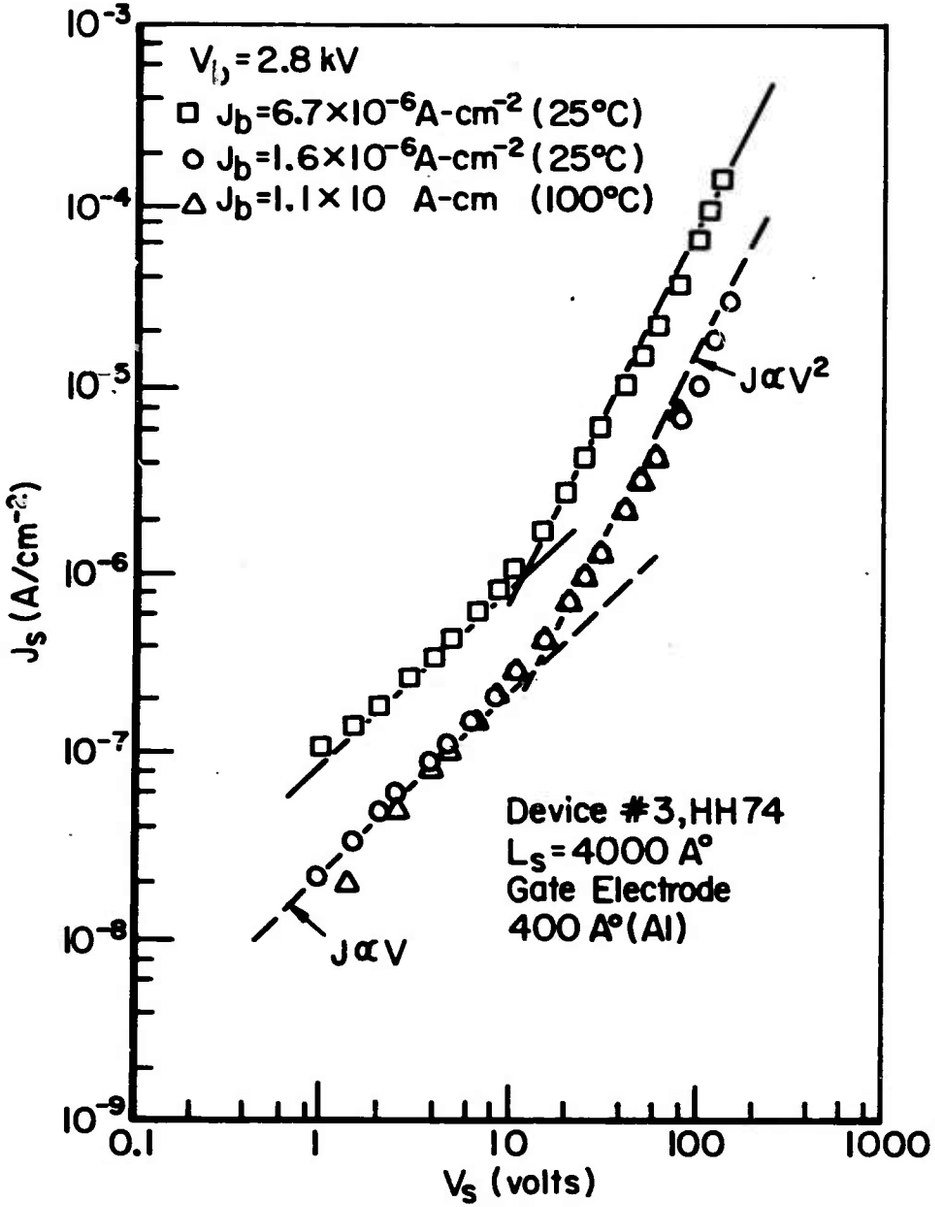

a) J vs V at Three Beam Currents and Two Temperatures

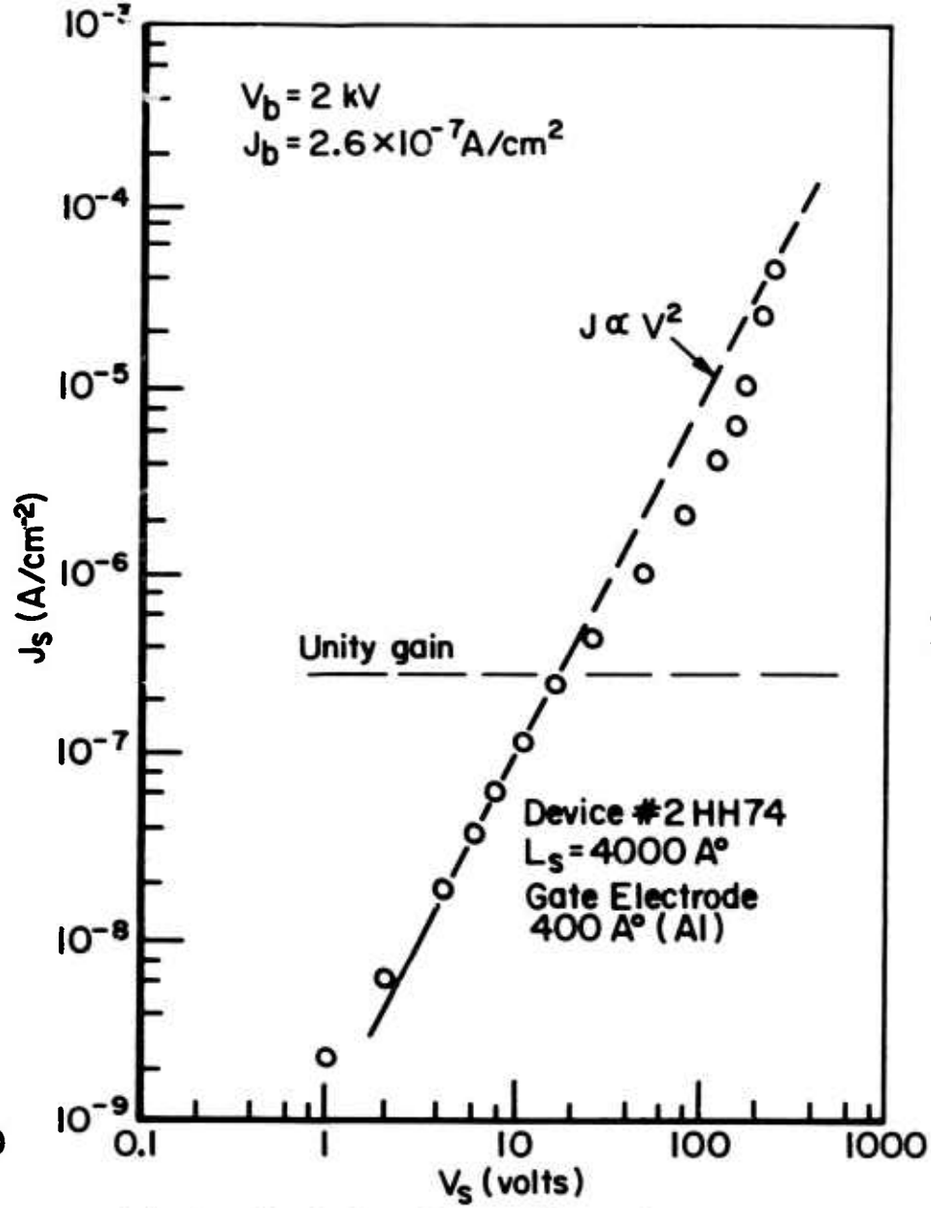

b) J vs V at One Beam Current

Fig. 34. Oxide Current-Voltage Characteristics at Fixed Beam Voltage

generally a temperature-insensitive square-law-regime, up to the point of unity gain ($I_{sample} = I_{beam}$), in which furthermore, at fixed voltage, $I_{sample} \propto I_{beam}$. We interpreted this set of results in terms of shallow-trapping of the injected electrons in the oxide bulk, the de-trapping being due to photons generated by the beam. In order to obtain supporting evidence for this interpretation, extensive charge-storage (C-V) measurements were made, both before and after electron-beam irradiation. These measurements have confirmed negative-charge storage in the oxide as a result of the beam injection. Further, the trapping states are created in the oxide bulk by the beam, presumably within the range of the beam. Interface states, at the $Si-SiO_2$ interface, are also created by the beam - undoubtedly by photons generated by the beam - but these states cannot explain either the I-V or C-V data.

B. Charge-Storage Studies: C-V and Internal Photoemission Measurements

A typical set of C-V curves is shown in Fig. 35. The capacitance measurements are made at high frequency, namely 1 MHz. The curve labelled ① is taken on the sample prior to any electron bombardment. It indicates a small initial positive charge in the sample. The curve labelled ② is measured following a 30-minute exposure, at low temperature (107°K) to UV illumination ($h\nu$ = 5 eV) through the gate with the gate positive, still prior to any electron bombardment. (This curve is actually independent of polarity). The very small shift to the right corresponds to a slight diminution of the net positive charge, due to trapping of the internally photo-injected electrons. Electron-trap densities in the as-grown thermal oxide generally do not exceed about 10^{14} cm^{-3}[14,15] giving a maximum trapped-electron sheet-density below 10^{10} cm^{-2}. This is consistent with the tiny shift from ① to ②. The curve labelled ③ exhibits the C-V curve measured after electron-beam irradiation for 15 minutes at 2.5 kV with the field in the oxide at 3×10^6 V/cm., with

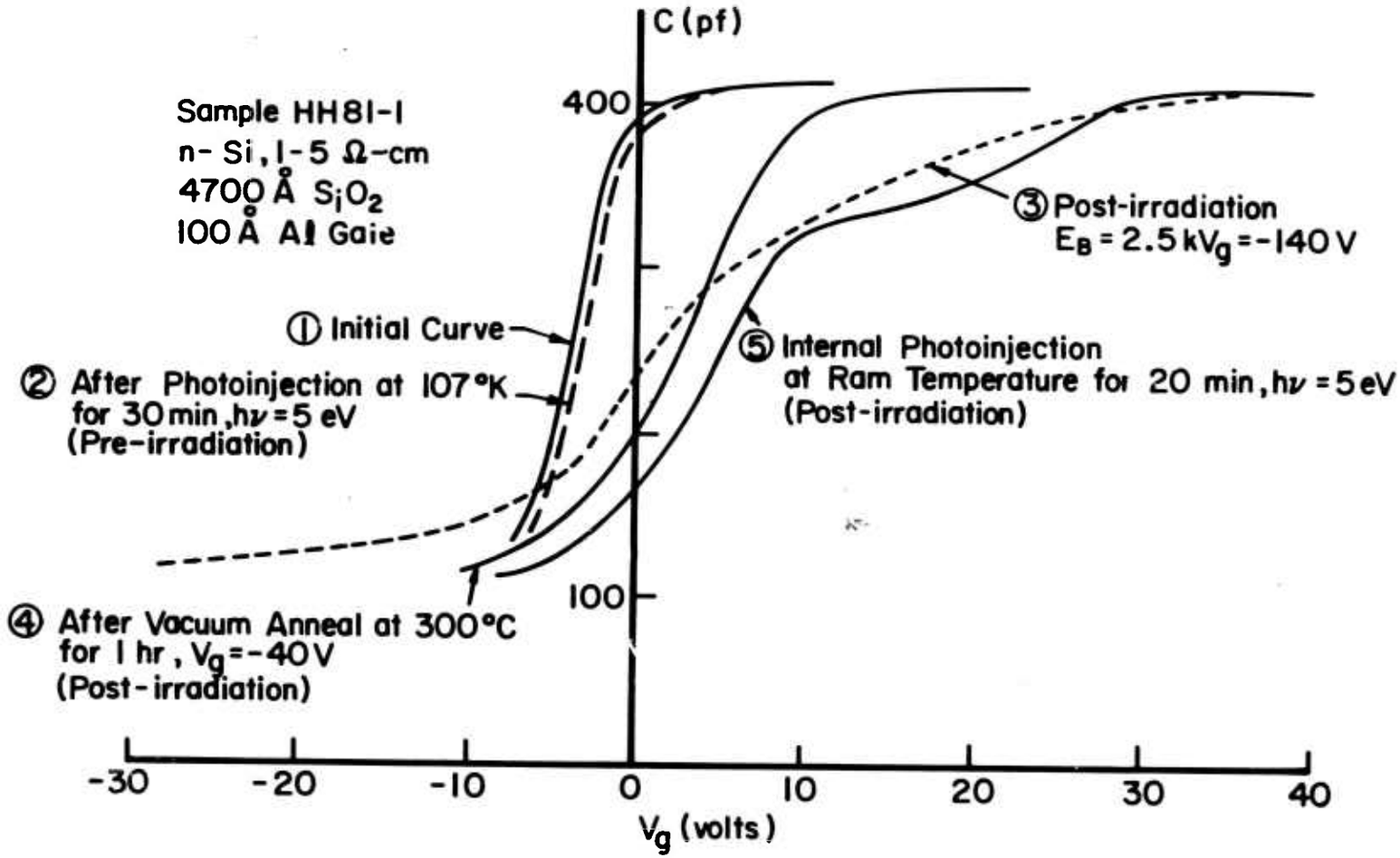

Fig. 35. C-V Curves Showing Effects of Electron Irradiation

the gate negative. This C-V curve is obviously strongly distorted and also indicates large negative charge storage. Its general shape is discussed further in connection with Fig. 36. The curve labelled ④ is a post-irradiation curve taken after a vacuum anneal at 300°C, for 1 hr, with the gate negative at 40 V. A substantial recovery from ③ toward ① is evident, both in the shape of the curve (much less distortion in ④ than in ③) and in the amount of shift. If the anneal had proceeded for many hours ④ would have been driven back to ① (this has been observed), indicating the removal of all negative charge trapped during the electron irradiation. After curve ④ was taken, and without any further electron irradiation or annealing, the sample was subjected to UV irradiation ($h\nu$ = 5 eV) for 20 minutes at room temperature with the results exhibited as curve ⑤. The significance of ⑤ is that it demonstrates conclusively that although the charge created by the electron irradiation is indeed annealable at 300°C (by thermal stimulation out of the traps) the traps themselves do not appear to be annealable (comparing ⑤ with ③), at least at the relatively low temperature of 300°C. The C-V measurements alone do not establish the spatial location of the electron traps in the oxide.

It is by now well-established that almost any form of radiation will either directly or indirectly (via UV or higher-energy photons) generate interface states at the $Si-SiO_2$ interface. The non-penetrating electron beam is no exception. Using the Gray-Brown technique[16], involving C-V measurements over a wide temperature range (from 100° to 300°K, in our case) we have indeed shown that the electron irradiation generated an order-of-magnitude increase in the surface-state density from 2×10^{12} cm^{-2} to 1×10^{13} cm^{-2}. However we do not see any way in which interface trapping of electrons, by itself, can explain our I-V data summarized in Fig. 34. Further evidence of the bulk nature of the electron trapping is given below, in the discussion of Figs. 40 and 41.

The shape of the post-irradiation C-V curves ③ and ⑤ in Fig. 35 can be understood by reference to Fig. 36. In the upper left inset we schematically illustrate the metallization dot with two areas indicated, an area A_b exposed to the electron beam (which is apertured) and an unexposed area A. Purely for simplicity of argument we assume $A = A_b$. Further, assume that the beam is uniform across A_b (rectangular profile in the inset). Obviously we are dealing with two capacitors in parallel, areas A and A_b respectively. The unexposed area A obviously exhibits the same C-V curve before and after irradiation, which we draw schematically as the dashed curve labelled $C = C_{b,pre}$ in Fig. 36. The exposed area A_b exhibits a quite different C-V curve after irradiation, $C_{b,post}$ in Fig. 36, than before irradiation, $C_{b,pre}$. There is a substantial flat-band shift to positive voltages due to stored negative charge and some distortion due to either interface-state generation or lateral non-uniformity. The two capacitors, of area A and A_b respectively, are obviously in parallel, so that the total effective capacitance C_t is simply the sum of the separate capacitances. Prior to irradiation $C_t \equiv C_{t,pre} = 2\ C$, the upper solid curve in Fig. 36, and following irradiation $C_t = C_{t,post} = C + C_{b,post}$, the dot-dashed curve in Fig. 36. [Note that non-uniformities in the irradiating beam will inevitably accentuate the distortion in the transition from low to high capacitance. Practically, the best that can be achieved with a stationary beam is a Gaussian profile, as illustrated in the inset of Fig. 36. A small lateral high-frequency wobble of a Gaussian beam might then yield an effectively uniform beam.] Note the strong resemblance of curves ③ and ⑤ in Fig. 35 to the schematic $C_{t,post}$ curve in Fig. 36.

The experimental C-V curves of Fig. 35 and schematic C-V curves of Fig. 36 are all high-frequency curves. A clearer separation of the separate capacitance effects of areas A and A_b is, in principle, achievable if low-frequency C-V

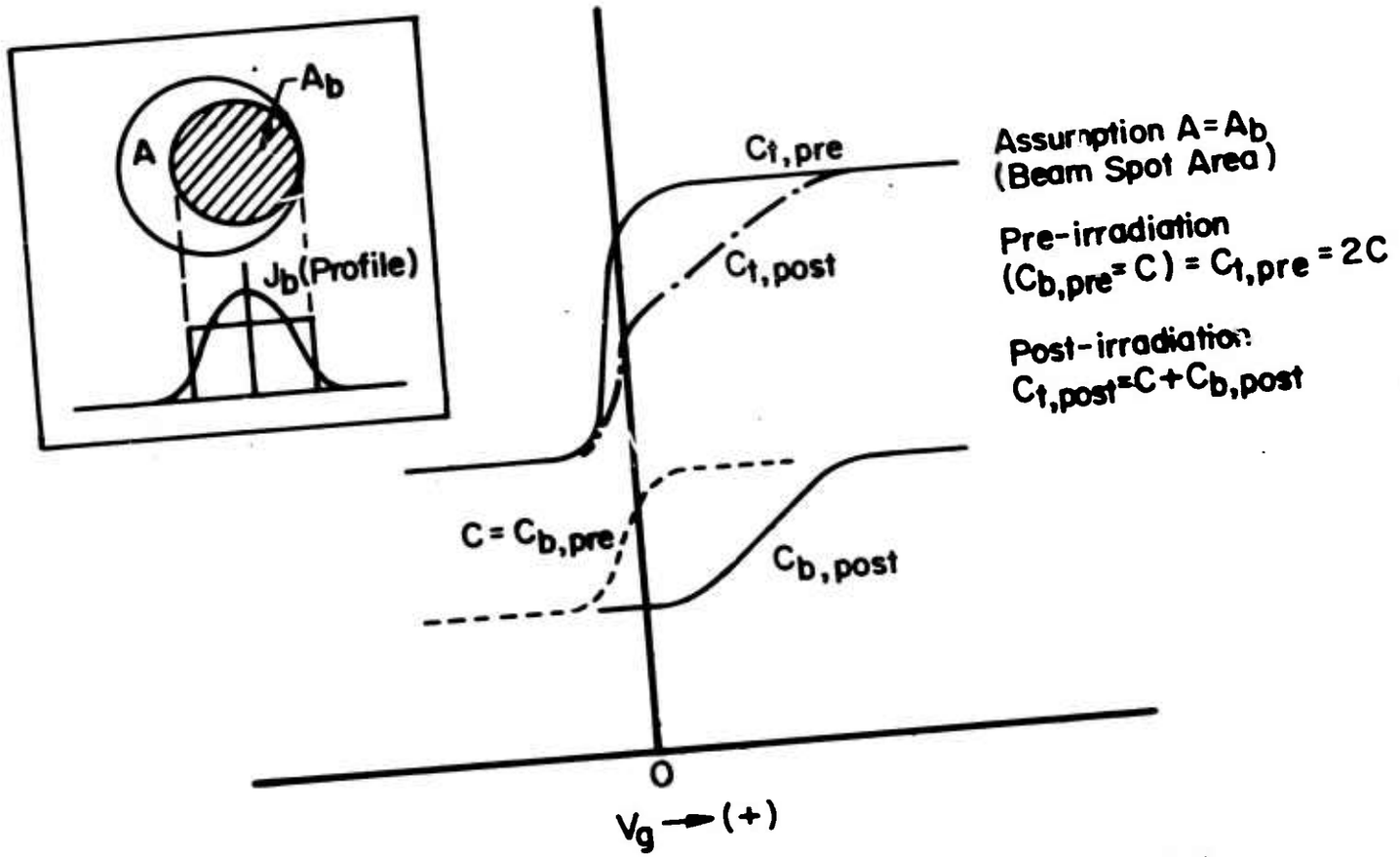

Fig. 36. Parallel Configuration of Capacitor (Schematic)

curves are measured. Practically, it is simpler to keep the measuring frequency fixed and reach the low-frequency C-V regime by either raising the temperature or illuminating the Si substrate, through the oxide, with strongly absorbed (supra-bandgap) light[17,18]. A comparison of the high- and low- frequency situations is given in the schematic C-V diagram of Fig. 37. The room-temperature curves ($T = T_1$) labelled C, $C_{b,post}$ and $C_{t,post}$ are the same as in Fig. 36, and are prototype high-frequency curves. The corresponding curves labelled C_{low}, $C_{b,post,low}$ and $C_{t,post,low}$ are the same C-V curves measured at a sufficiently higher temperature ($T = T_2$) to represent prototype low-frequency curves. The transition portion of the high-frequency C-V curve becomes a dip in the corresponding low-frequency C-V curve. Further, where a significant flat-band shift from C to $C_{b,post}$ has occurred (high-frequency curves), as in Fig. 36, the dips d_1 and d_2 in the corresponding low-frequency curves are well-separated, as shown in Fig. 37. The effects illustrated schematically in Fig. 37, are seen experimentally, as shown in Fig 38. Three post-irradiation C-V curves are shown, corresponding to successively higher temperatures of measurement, ① at room temperature, ② at 200°C and ③ at 250°C. Both ① and ② have the high-frequency appearance of curve ③ of Fig. 35, or $C_{t,post}$ of Fig. 36, whereas ③ exhibits the characteristic low-frequency dips of Fig. 37. Curve ④ is a post-irradiation, room-temperature C-V curve following a partial anneal. Curve ④ is shifted leftwards from ①, as expected. The dip d_2, associated with injected negative charge, is shifted leftwards as a result of annealing, the shift being greater the longer the annealing time.

A curve such as ③ in Fig. 35, corresponds to a single value of gate bias during irradiation (in this case -140 V). Based upon the model of Fig. 36, a flat-band voltage shift can be associated with curve ③, namely from that portion of the curve associated with the irradiated area. The flat-band

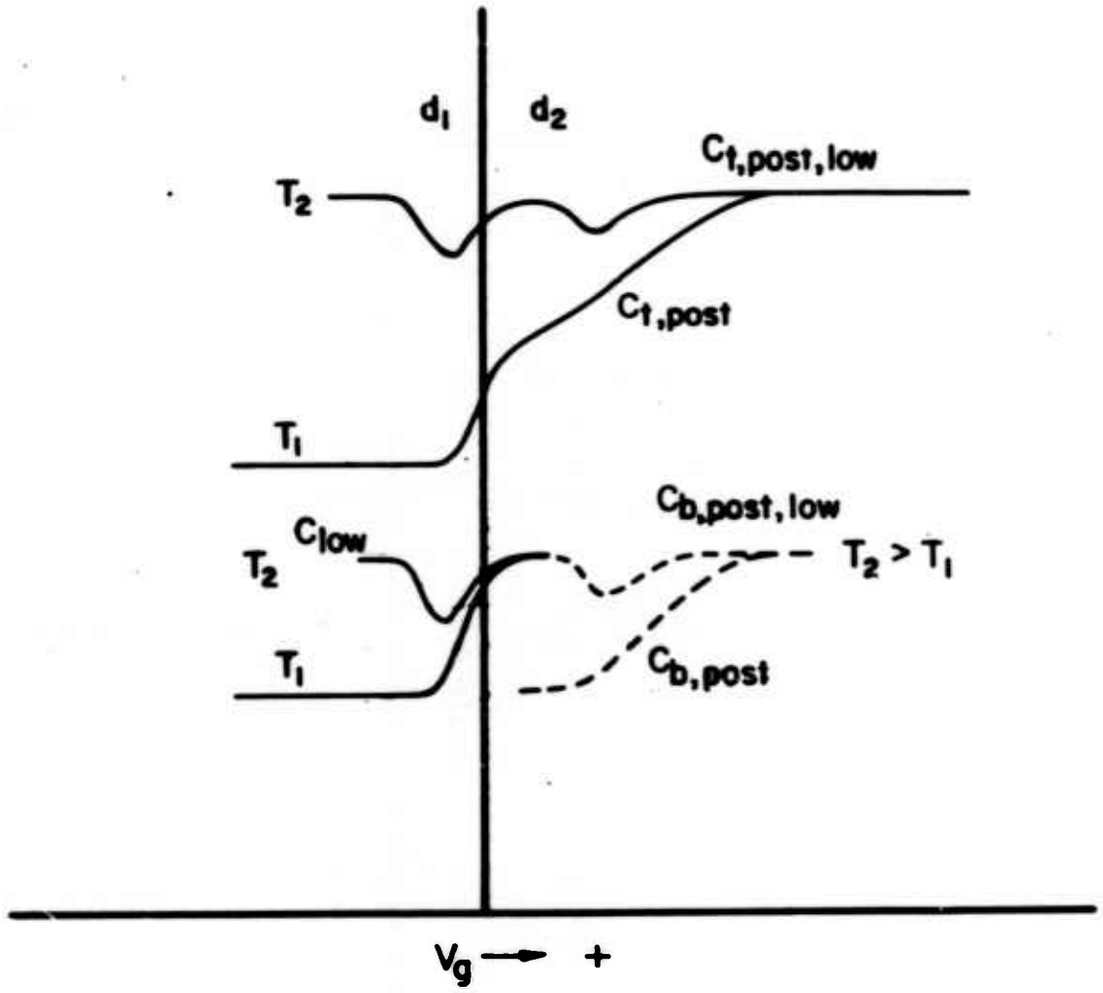

Fig. 37. Effect of Temperature on C-V Curves for Parallel Configuration of Capacitors (Schematic)

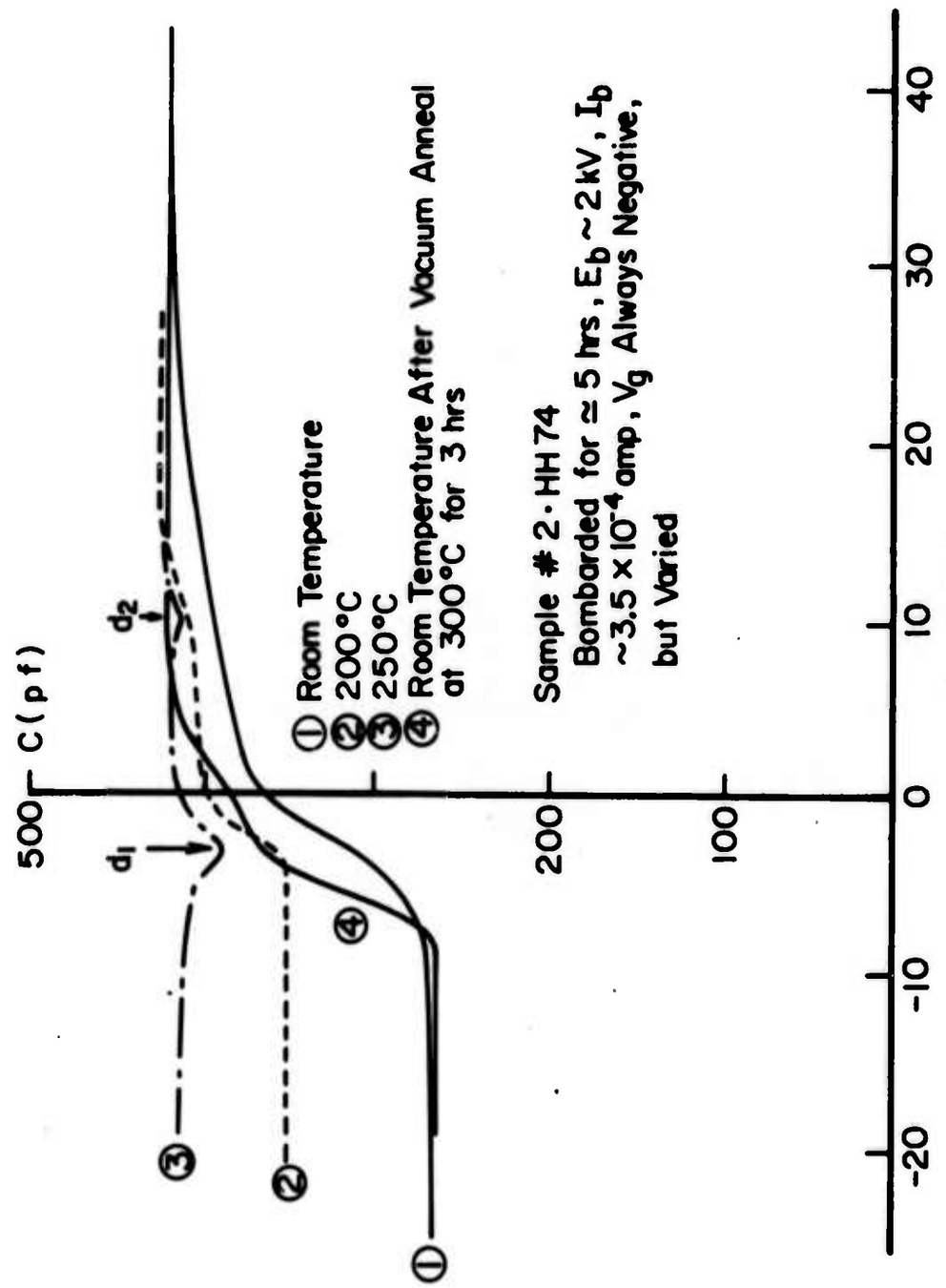

Fig. 38. Temperature Dependence of Post-Irradiation C-V Curve

voltage shift so determined as a function of gate bias during electron irradiation (for a fixed dosage of 3.5×10^{-9} amp of 2 kV electrons for 5 hrs.) is shown in Fig. 39, for irradiation at two temperatures, 200°K and 300°K. The dip in this curve with increasing (negative) gate voltage is not presently understood. The large hysteresis exhibited by the 300°K curve (dashed portion) is quite normal— as $|V_g|$ is reduced in successive irradiations, trapped electrons are not thermally released and the sample is not in thermal equilibrium at the lower $|V_g|$. A similar hysteresis is seen with the 200°K curve (not shown).

The UV-induced ($h\nu$ = 5.0 eV) internal photo-emission current from the Si substrate into the oxide as a function of gate bias (positive) is shown in Fig. 40, under three conditions: curve (1) is taken prior to irradiation by the electron beam, curve (2) after irradiation by the beam and curve (3) after irradiation, then annealing at 300°C for one hour. These curves provide very strong, independent evidence for electron trapping. Curve (1) has the expected shape previously predicted and found experimentally by Powell and Berglund[19]. The post-irradiation curve (2) is approximately a translation of (1) by about 25 V. This latter is readily interpreted as the voltage required to overcome the potential barrier created by the trapped negative charge left in the oxide bulk by the electron-irradiation. The anneal at 300°C for one hour removes over half of this trapped charge so that curve (3) is much closer to the pre-irradiation curve (1).

The curves in Fig. 40 were obtained with a slow, linear ramp voltage across the oxide, as indicated by the diagram in the inset in Fig. 41. The directly measured photocurrent is exhibited as the dashed curves in Fig. 41. There is a hysteresis associated with the direction of the ramp, as shown. The dashed curve includes the contribution to the total current of the constant displacement current associated with the linear ramp. With the direction of the ramp inverted,

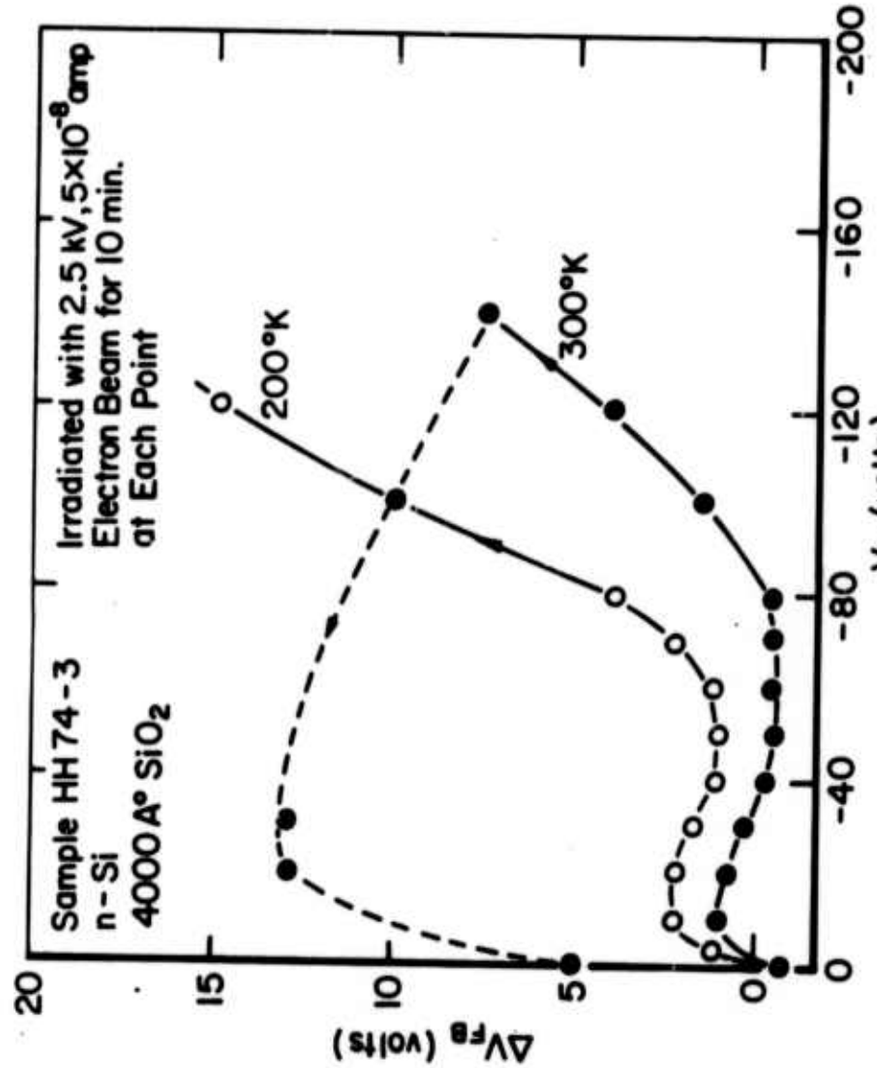

Fig. 39 Flat-Band Voltage Shift vs Gate Bias During Irradiation at Two Different Temperature

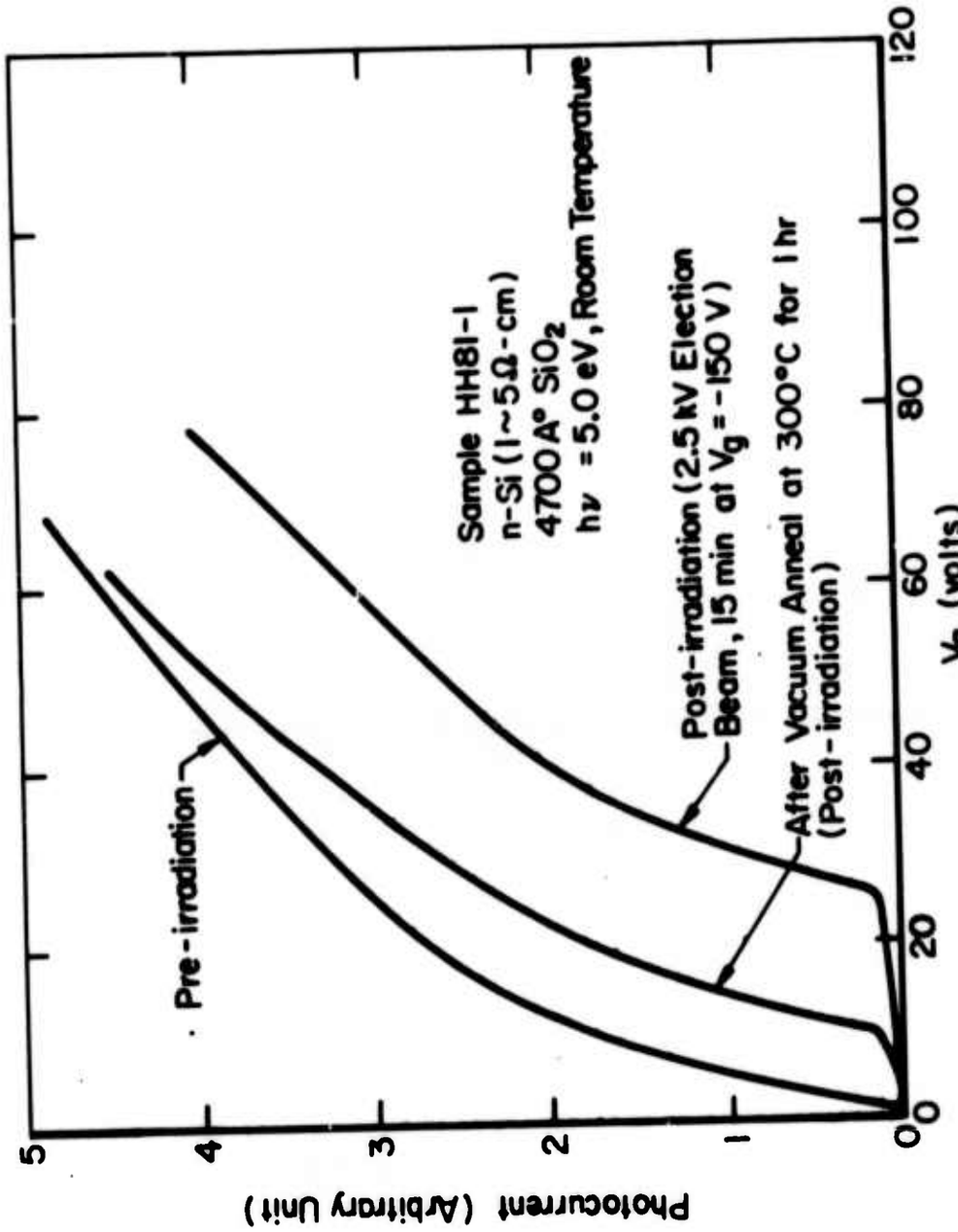

Fig.40. Effect of Oxide Charge on Internal Photoemission Current

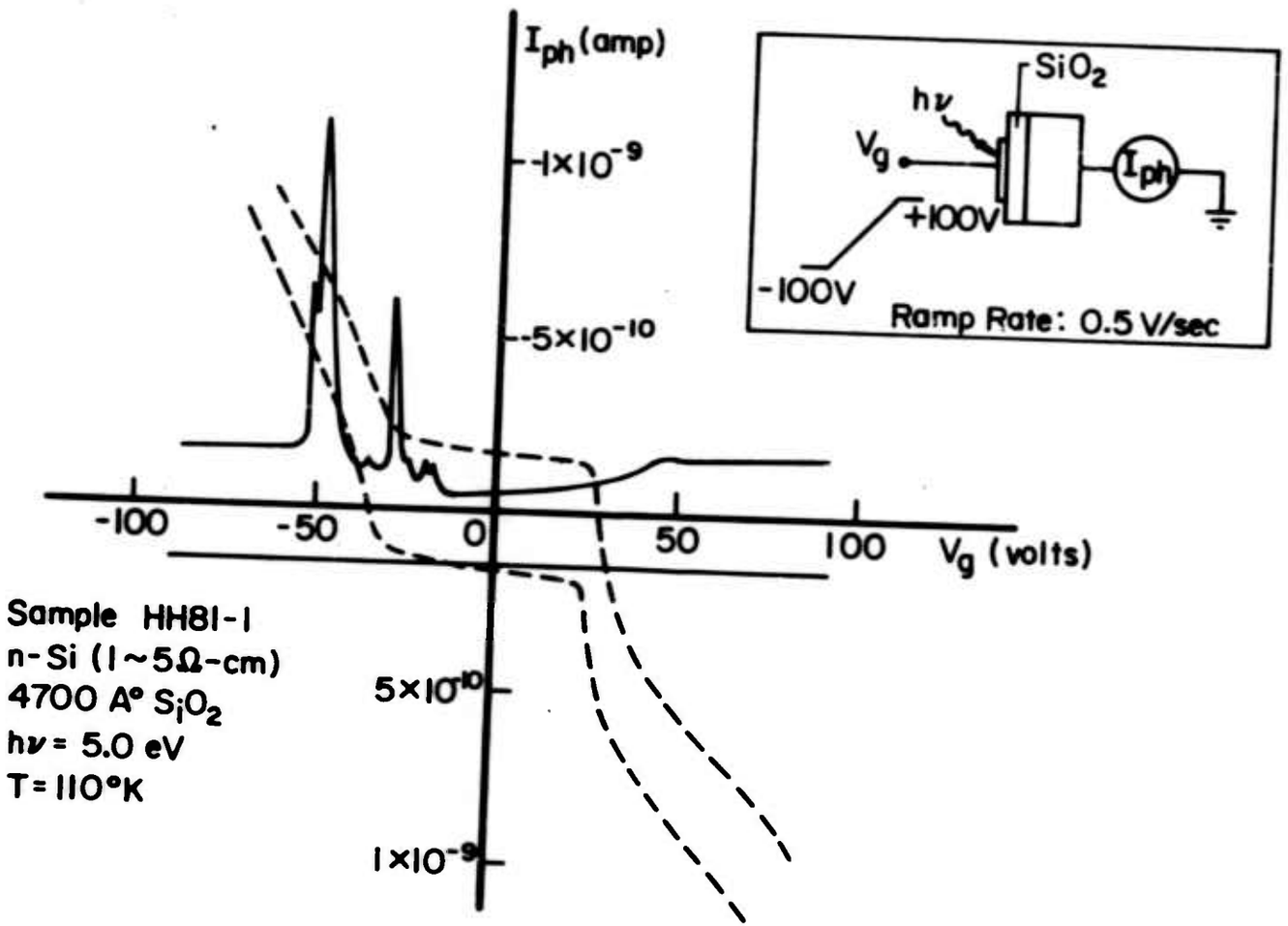

Fig.41. Internal Photoemission Current and Dark Current of the Irradiation Sample with Ramp Voltage Applied Across the Oxide

the constant displacement current changes sign, hence the hysteresis. The three curves exhibited in Fig. 40 have the displacement current substracted out, for the sake of clarity (that is why the curves in Fig. 40 all go through the origin, whereas the two dashed curves in Fig. 41 are symmetrically displaced from the origin).

More important than the hysteresis, which is simply an artifact of the measuring technique, is approximate symmetry as between positive and negative gate bias of either dashed curve, after the constant displacement current is substracted out. In either polarity there is the same magnitude of threshold voltage before photo-emitted current can flow. This is precisely what one would expect from a potential barrier inside the oxide bulk due to trapped negative charge.

Also exhibited in Fig. 41 are the quasi-static C-V curves at room temperature (the solid curves), which, for the slow ramp, are simply I_{ox} vs V_g[20,21,22], in the absence of the UV. In the upward direction of the ramp (- to +) I_{ox} is the pure displacement current of the ramp (the horizontal line); in the downward direction of the ramp there is a very rich structure in I_{ox} vs V_g which is not understood at present. At elevated temperatures such structure could be attributed to ionic motions, but it is difficult to invoke such ionic motions at room temperature.

C. Summary

The outstanding result to-date of our electron-beam irradiation studies is the demonstration of stored negative charge in the bulk following the non-penetrating irradiation. Relatively few other studies have been made utilizing non-penetrating electron beams[23,24,25] and these studies have only reported positive charge storage, near the $Si-SiO_2$ interface, following the irradiation. A major goal of our current program is the reconciliation of these earlier results with our own results. Our current efforts

are concentrated on improving the uniformity of our electron beam and designing means to profile the beam. We expect to obtain the greater uniformity by going over from the standard oxide which we have been using, to a thoriated tungsten cathode. Special phosphor screens have been fabricated for beam-profiling purposes, by the Phosphor Group at RCA Laboratories.

7. Theory of Electron-Tunneling from Si into SiO_2 - Triangular Well Approximation (Z. Weinberg collaborating)

A. Background Discussion

At the high fields (> 5×10^6 V/cm; see Fig. 5) which are required to produce significant tunneling currents from Si into SiO_2 there is very strong band-bending in the Si near the interface. Our interest here is in the polarity with the Si negative, in which case there is a degenerate electron gas in the Si conduction band adjacent to the interface. If the Si is n-type, it is in accumulation at the interface; if the Si is p-type, it is in inversion. Whether the Si is in accumulation or inversion, the electron gas is confined in a very narrow well in the direction perpendicular to the interface. This confinement leads to spatial quantization effects in the perpendicular direction, which have been studied in the inversion case by Stern[10], and in the accumulation case by Duke.[26] The spatial quantization effects have been studied theoretically with various degrees of refinement. A completely accurate theoretical study requires the self-consistent solution of the Schrödinger equation for all electrons trapped in the well together with the Poisson equation (since the detailed shape of the well is determined by space-charge considerations). Such studies, which require the use of a high-speed digital computer, have been made.[10] However, in no case which we are aware of has the spatial-quantization problem been looked at with the aim of calculating the tunneling current from the well into the oxide film. This is precisely the problem to which we address

ourselves here. In order to get a reasonable, analytical handle on the problem we neglect the specific space charge effects and assume that the well has a triangular shape, as shown in Fig. 42. For the case that most of the electrons in the well occupy the lowest quantized energy state, the triangular well approximation is a good one. Since this is also a case of great practical interest, the results presented here are of direct use in the analysis of tunneling currents. (From the diagram in Fig. 42 it is clear that we are also neglecting the well-known image-force lowering of the potential barrier by the tunneling electron. This effect produces only a small change in the tunneling probability, and can be suitably incorporated into the results at a later point.

B. The Mathematical Calculation

The one-electron (fixed potential) quantum-mechanical problem to be solved is defined by Fig. 42. The electron in the Si is trapped in the well defined by the potential step, height $\phi = 3.1$ ev (for SiO_2), at the interface and by the bottom energy of the Si conduction band $E_{c,Si} = -q\mathcal{E}_1 x$ where q is the magnitude of charge on the electron, $\mathcal{E}_1$ the field in the Si (assumed constant near the interface) and x the position variable normal to the interface which is located at x = 0. The barrier through which it must tunnel is defined by the potential step at the interface and by the lowest energy of the SiO_2 conduction band $E_{c,SiO_2} = q\phi - q\mathcal{E}_2 x$.

Mathematically it is convenient to obtain the solution in two non-overlapping regions: Region I extending from the interface into the Si, and Region II extending from the interface into the SiO_2. In each region the solution consists of a suitable combination of Airy functions.[27] The separate solutions are then matched at the interface to provide current continuity. As one might expect in a tunneling problem, the solution inside the well, i.e. Region I, is

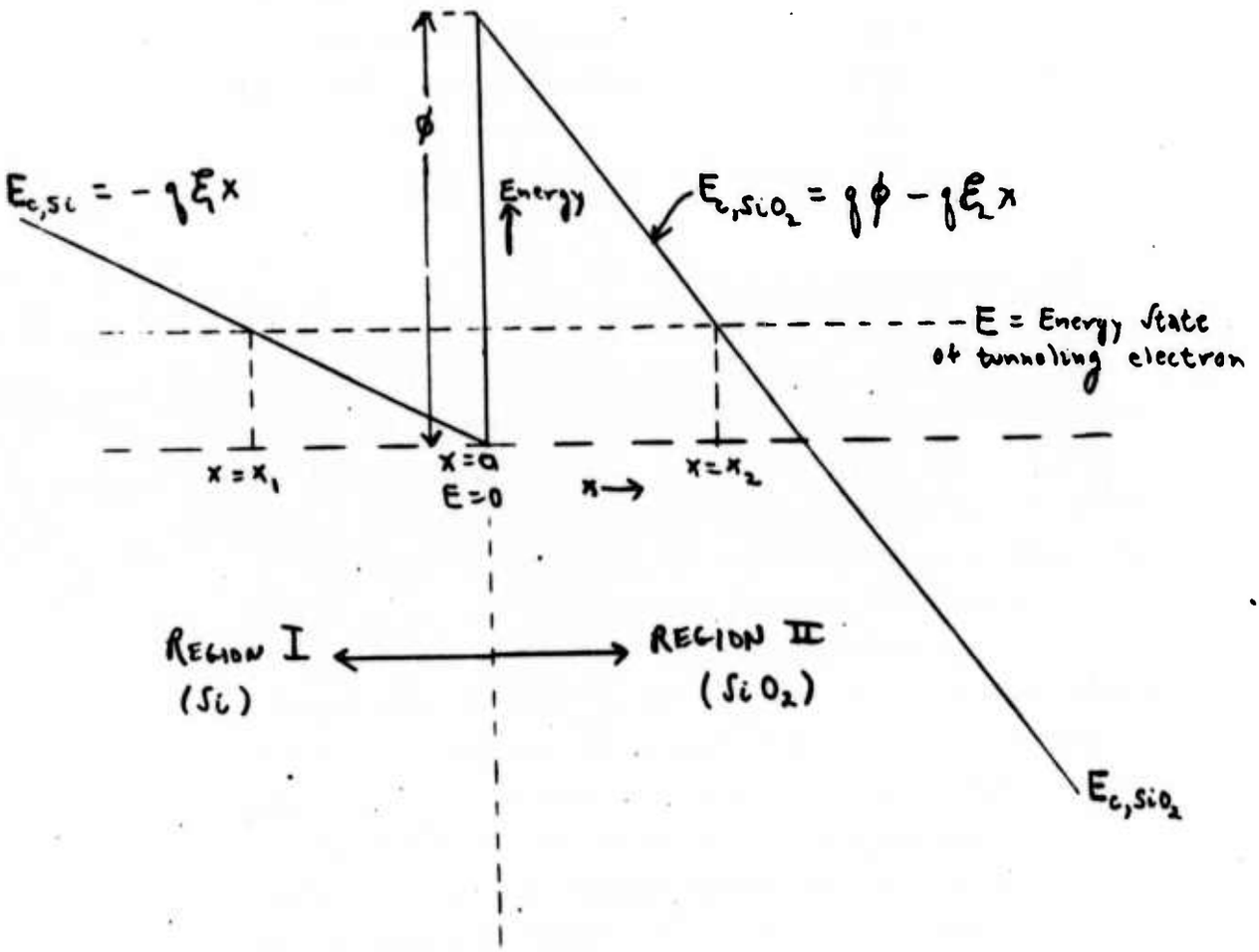

FIG. 42. ENERGY-BAND DIAGRAM FOR TUNNELING FROM Si INTO SiO_2 (TRIANGULAR-WELL APPROXIMATION)

only slightly affected by the presence of the field in the oxide. Thus, the wave function normalization can be carried out using only the solution in Region I. This procedure leads to a closed-form expression for the tunneling current per electron out of the ground state of the well. The total tunneling current must include, additionally, the contributions from electrons in participating excited states in the well. Since the triangular-well approximation is not a good one for the study of the excited levels, we can obtain only a somewhat crude estimate for the tunneling contributions from the former using Airy-function solutions.

We proceed to the mathematical discussion:

Region I (Si): $-\infty < x < 0$, Field $\mathcal{E}_1$, electron effective-mass m_1.

The appropriate Schrodinger equation in the normal direction is

$$\frac{d^2\psi(x)}{dx^2} + \frac{2m_1}{\hbar^2}(E + q\mathcal{E}_1 x)\psi(x) = 0 \ . \qquad (46)$$

Region II (SiO_2): $0 < x < \infty$, Field $\mathcal{E}_2$, electron effective-mass m_2.

The appropriate Schrodinger equation in the normal direction is

$$\frac{d^2\psi(x)}{dx^2} + \frac{2m_2}{\hbar^2}(E - q\phi + q\mathcal{E}_2 x)\psi(x) = 0. \qquad (47)$$

E in Eqs. (46) and (47) is the eigen-state energy of the electron.

It is convenient to introduce dimension-less variables:

$$\text{Region I:} \quad y_1 = a_1^{1/3}\left(\frac{E}{q\mathcal{E}_1} + x\right) \ , \quad a_1 = \frac{2m_1}{\hbar^2} q\mathcal{E}_1 \ ; \qquad (48)$$

$$\text{Region II:} \quad y_2 = a_2^{1/3}\left(\frac{E - q\phi}{q\mathcal{E}_2} + x\right), \ a_2 = \frac{2m_2}{\hbar^2} q\mathcal{E}_2 \ . \qquad (49)$$

Substitution of (48) into (46), and (49) into (47) reduces the two Eqs. (46) and (47) to a common form:

$$\psi''(y_{1,2}) + y_{1,2}\,\psi(y_{1,2}) = 0 \quad , \tag{50}$$

which is a form of Airy's Eq. This equation has two independent solutions which are conventionally written as[27]:

$$Ai(-y) \quad \text{and} \quad Bi(-y)$$

The boundary conditions appropriate to the present tunneling problem are physically obvious.

i) The wave function must decay exponentially going toward $-\infty$ in Region I, i.e. well beyond $x = x_1$.

ii) The wave function must describe a pure outgoing wave in Region II beyond $x = x_2$.

These boundary conditions enable us to write the appropriate solutions of (50) as:

Region I: $\psi = \alpha\, Ai(-y_1)$; (51)

Region II: $\psi = T[Bi(-y_2) + i\, Ai(-y_2)]$. (52)

From (48) and (49), at $x = 0$

$$y_{1,o} = a_1^{1/3}\,\frac{E}{q\mathcal{E}_1} \quad \text{and} \quad y_{2,o} = a_2^{1/3}\,\frac{E - q\phi}{q\mathcal{E}_2} \approx -\,a_2^{1/3}\,\frac{\phi}{\mathcal{E}_2} \quad , \tag{53}$$

since $\phi = 3.1$ ev $\gg E$. With $y_{1,o}$ known, E is determined by (53). Using (49) and the known tunneling field in the oxide ($\approx 6 \times 10^6$ V/cm) we obtain a good estimate for a_2:

$$a_2^{1/3} \approx 2.5 \times 10^9/\text{meter} = 0.25/\mathring{A} \quad . \tag{54}$$

Using this value in (53), taking $\phi/\mathcal{E}_2 = 3.1/6 \times 10^6 \approx 50\mathring{A}$, we obtain

$$y_{2,o} \gtrsim 10 \quad . \tag{55}$$

It is a property of the Airy functions that, in going from x_2 towards $x = 0$, $Ai(y_2)$ decays exponentially whilst $Bi(y_2)$ increases expcnentially. Since $y_{2,o} >> 1$, $Ai(-y_2)$ can be neglected compared to $Bi(-y_2)$ at $y_2 = y_{2,o}$ and the matching of the wave function at $x = 0$ gives, using (51) and (52):

$$\alpha Ai(-y_{1,o}) = T\, Bi(-y_{2,o}) \quad . \tag{56}$$

Matching of the derivative of the wave function at $x = 0$ gives:

$$a_1^{1/3}\, \alpha\, Ai'(-y_{1,o}) = a_2^{1/3}\, T\, Bi'(-y_{2,o}) \quad . \tag{57}$$

Because $|y_{2,o}| >> 1$ it is permissible to use the asymptotic form of the function $Bi(-y_2)$ in evaluating it at $y_2 = y_{2,o}$. Finally, then, division of (56) by (57) gives the equation:

$$\left.\frac{Ai}{Ai'}\right|_{-y_{1,o}} = \left(\frac{a_1}{a_2}\right)^{1/3} |y_{2,o}|^{-1/2} \lesssim 0.1 \quad . \tag{58}$$

The solutions to this equation are the eigen-energies E_i. Note that (58) replaces the simpler condition

$$Ai(x = 0) = 0 \quad , \tag{59}$$

used in space-quantization theory for a triangular well bounded by an infinite wall ($\phi = \infty$). In our problem the solutions E_i to Eq (58) differ negligibly from those to Eq. (59), as shown by Stern.[10]

The tunneling current density, corresponding to the pure outgoing wave (52) in Region II, can be written as

$$J = \frac{\hbar}{\pi m_2}\, a_2^{1/3}\, T^2 \quad . \tag{60}$$

The coefficient T is given by (56):

$$T^2 = \frac{Ai^2(-y_{1,o})}{Bi^2(-y_{2,o})}\,\alpha^2 \quad . \tag{61}$$

As remarked earlier, the wave function throughout Region II is small enough that we can neglect it in normalizing the total wave function. Thus, we write for the normalization:

$$\int_{-\infty}^{o} \alpha^2\, Ai^2 dx = 1 \quad , \tag{62}$$

which yields

$$\alpha^2 = a_1^{1/3}\,\frac{1}{Ai'^2(1+f)} \quad , \quad f = y_{1,o}\,\frac{Ai^2}{Ai'^2} \quad , \tag{63}$$

where the argument of Ai and Ai' is $-y_{1,o}$.

From (58) we know that $(Ai/Ai')^2_{-y_{1,o}} < 0.01$. Further, for the first ten energy levels E_i, $y_{1,o,i} < 10$. Hence $f < 0.1$, and can be neglected in (63).

Using the various results above in (60) we finally obtain for the tunneling current:

$$J = 2\,\frac{m_1}{m_2}\,\frac{1}{\sqrt{2m_2}}\,\frac{q\mathcal{E}_1}{\sqrt{q\phi}}\,\exp -(FN) \quad , \tag{64}$$

where

$$(FN) = \frac{4}{3}\sqrt{\frac{2m_2}{\hbar^2}}\,\frac{(q\phi - E)}{q\mathcal{E}_2} \quad , \tag{65}$$

and the notation (FN) has been used because the exponent in (64) is Fowler-Nordheim-like (see Eqs. (2) and (3)).

It is convenient to re-write (64) in the form

$$J = \frac{4\pi}{Z_o^{3/2}}\,(\frac{m_1}{m_2})^{3/2}\,(\frac{E_o}{q\phi})^{1/2}\,\frac{E_o}{h}\exp -(FN) \quad , \tag{66}$$

where E_o is the lowest space-quantized energy-level in the well:

$$E_o = \frac{(\hbar q \mathcal{E}_1)^{2/3}}{(2m_1)^{1/3}} Z_o \quad , \tag{67}$$

Z_o being the first zero of the Airy function: $Ai(Z_o) = 0$, and $Z_o = 2.34$. Here we have used (59) as a suitable replacement for (58).

The factor E_o/h in the pre-exponential of (66) has the dimension of frequency; indeed it is the frequency of the periodic motion of the electron in the well. Physically it corresponds to the frequency with which the electron hits the potential wall ϕ in Fig. 42 and has accordingly been called "the attempt-to-escape" frequency in the literature. The pre-exponential factor in (66), corresponding to tunneling from a bound state in a triangular well, replaces the pre-exponential factor $\beta\mathcal{E}^2$ of Eqs. (2) and (3), corresponding to tunneling from a Sommerfeld electron gas, in which case one more appropriately considers the particle current incident on the barrier.

C. Application of the Theory

The theory of Section B has been applied to the tunneling experiments on the Si-SiO_2 system described in Section 2. These experiments were all done on (100) Si, for which the appropriate (weighted) electron effective mass in the space-quantization problem is $m_1 = 0.9$. The electron effective mass in the oxide, obtained from the experiments is 0.4 (see Eq. (8)), $E_o = 0.3$ ev, obtained from (67) taking $\mathcal{E}_1 = 6 \times 10^6$ V/cm (see Fig. 5). The corresponding attempt-to-escape frequency is $E_o/h = 7 \times 10^{13}$/sec. Using this in (66) we evaluate the complete pre-exponential factor as

$$J \simeq 1.4 \times 10^8 \exp - (FN) \qquad \text{Amp/cm}^2. \tag{68}$$

The corresponding classical Fowler-Nordheim expression (2) and

(3) yields

$$J = 4 \times 10^{7} \exp - (FN) \quad \text{Amp/cm}^2. \tag{69}$$

In arriving at (68) we have considered tunneling only from the ground state of the well. Stern[10] has estimated that approximately 70% of the electrons in the well at the interface are in the ground state, under the conditions of our experiment, so that (68) should be a fair estimate for J, even allowing that the remaining 30% of the electrons have a higher tunneling probability (smaller area of tunneling barrier). The small image-force corrections to (66) are taken up in a more complete study of this problem to be published later.

8. Monte-Carlo Studies of Hot-Electron Behavior in Insulating Films at High Fields (S. Baidyaroy collaborating)

A. Background Discussion

In the First Semiannual Technical Report an extensive discussion of our Monte Carlo studies of hot electrons in high fields in insulating films was given. Most of that discussion was concerned with constant-mean-free-path problems, with both isotropic and anisotropic scattering. In particular, a detailed study was made of one-dimensional random-walk simulations of three-dimensional problems. A beginning was made on the study of runaway electrons in situations where the mean free path is energy-dependent and increases with energy. In this report we present some additional information on one-dimensional simulations of anisotropic scattering problems and carry the study of runaway electrons considerably further.

B. New Results

In the First Semiannual Report it was shown that constant mfp (mean free path) problems with anisotropy could be well simulated by one-dimensional random walks with a single

anisotropy parameter. In particular, in Fig. 28 of that report it was shown that the computer results could be represented by the simple constant mfp scaling law: $E_{ave,ss} \propto (F\lambda)^2/\varepsilon_{ph}$, with $E_{ave,ss}$ the mean energy of the electron emerging from the film in the steady-state (i.e. independent of film thickness), F the electric field intensity in the film, λ the constant mean free path, and ε_{ph} the optical phonon energy. In that Fig. curves were plotted for f = 0.2, 0.4, 0.5, 0.6 and 0.8, f being the anisotropy parameter (ratio of forward-to-back scattering probabilities). A mysterious change in slope appeared in the f = 0.2 curve. The calculations for f = 0.2 have been done over, with the new results presented in Fig. 43. Also plotted are new results, namely the curves for f = 0.1 and f = 0.9 respectively, and the old results for f = 0.4, 0.5, 0.6 and 0.8. Since the seven plots of Fig. 43 are all linear, the relationship

$$E_{ave,ss} = \kappa_f \frac{(F\lambda)^2}{\varepsilon_{ph}} , \tag{70}$$

holds, where $\kappa_f = \kappa(f)$ is an f-dependent constant which is determined empirically, namely from calculations such as exhibited in Fig. 43. A semi-long plot of κ_f vs f is given in Fig. 44, with points available in the range of $0.1 \leq f \leq 0.99$. It is seen that in the 'middle' range, $0.1 \leq f \leq 0.8$, a simple power-law obtains:

$$0.1 \leq f \leq 0.8 : \quad \kappa_f \simeq 0.1 \exp 4.22f \tag{71}$$

Since κ_f must diverge as $f \to 1$ (pure forward scattering) this relation cannot be valid for f close to 1, as indeed we note in Fig. 44.

A second area in which important progress has been made concerns the runaway of electrons in situations where the mean free path is energy-dependent and increases as the energy increases. Such situations were examined briefly at the end of the First Semiannual Report, in Figs. 38-41 inclusive. The

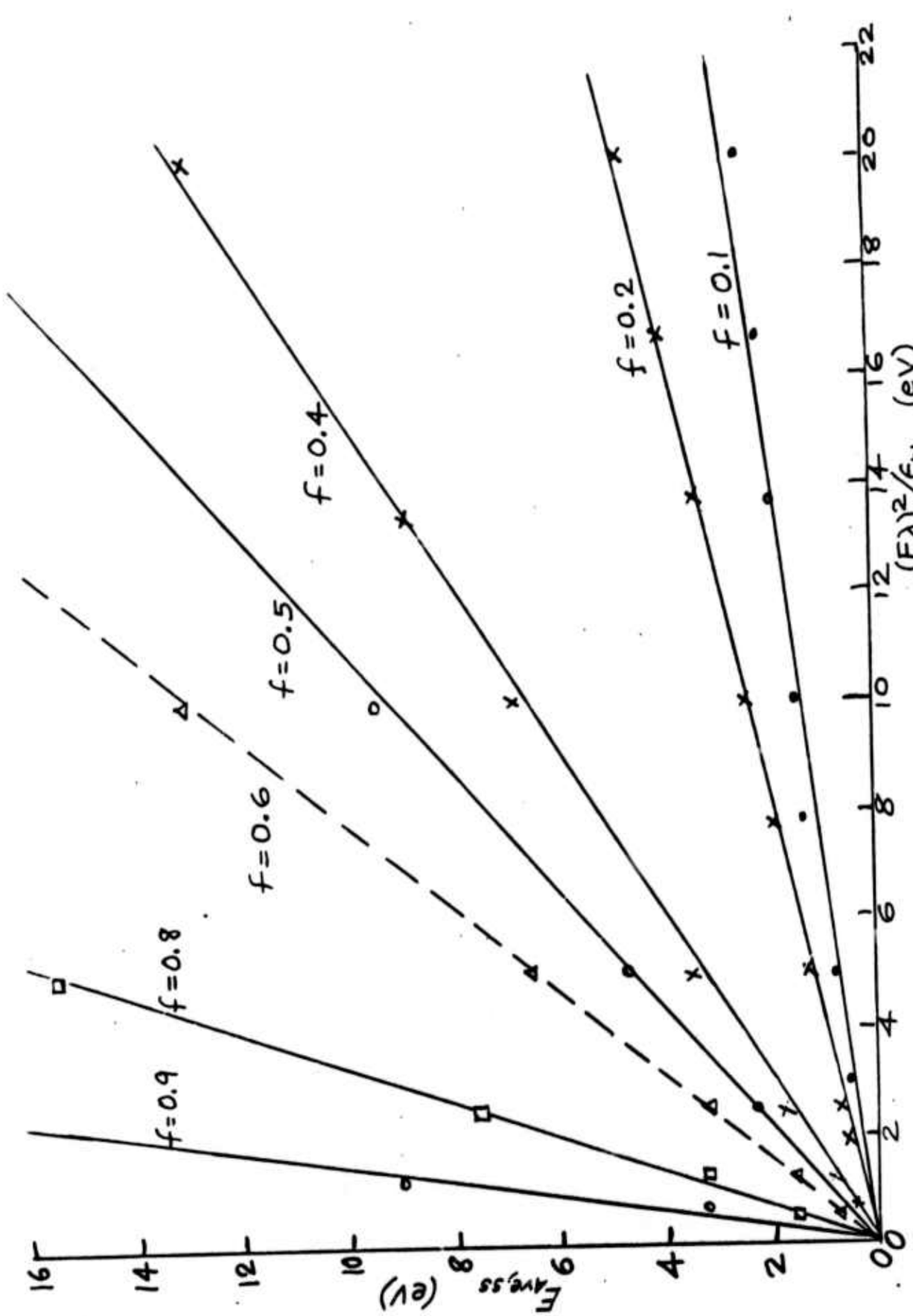

Fig. 43. Scaling-Law Curves for Anisotropic Scattering (One Dimensional simulation)

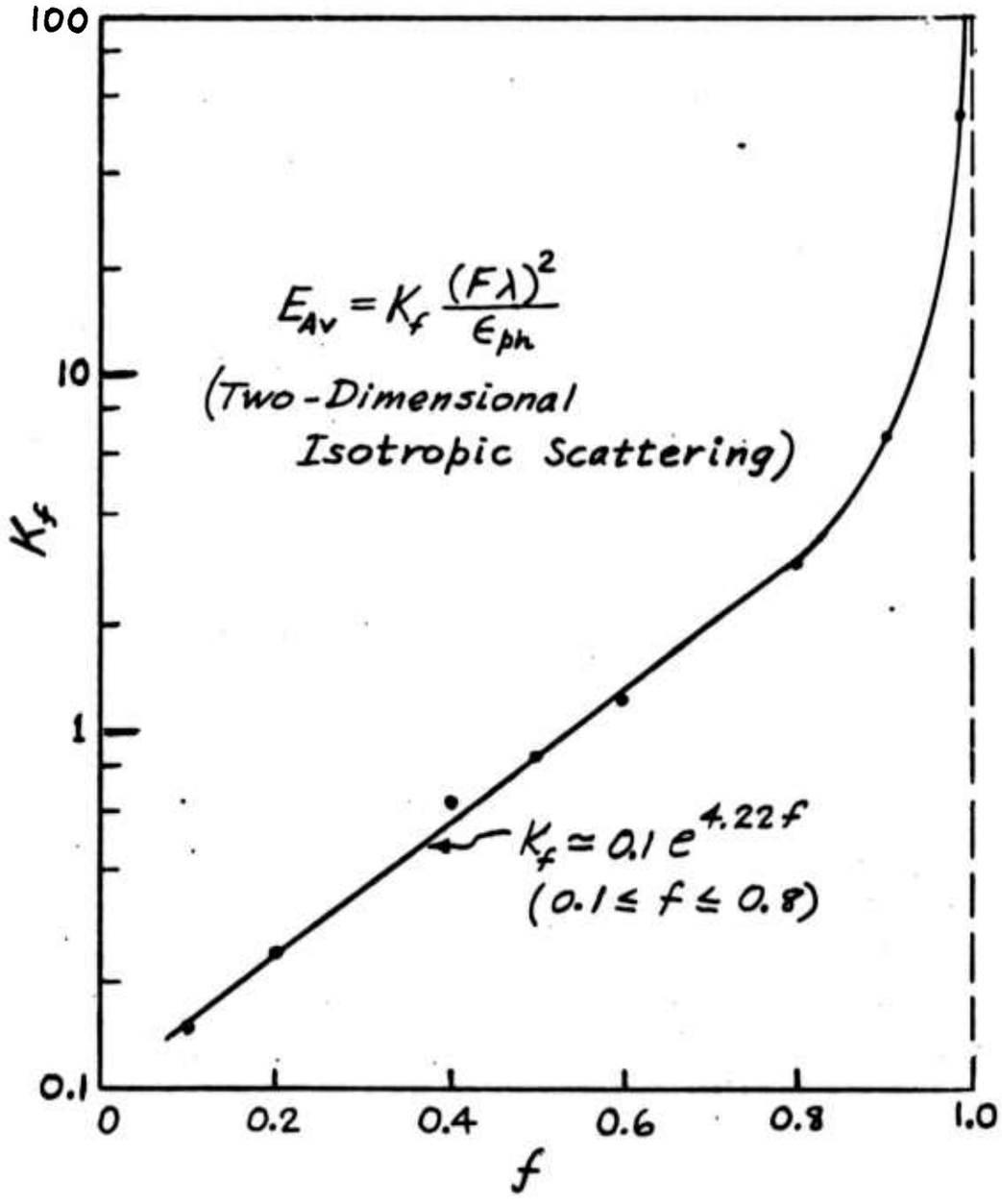

Fig. 44. f-Dependent Constant in Scaling Law.

key figure was Fig. 38 which is reproduced here, with several additional curves on it, as Fig. 45. In this Fig. the average energy E in the emerging electron distribution is plotted vs mfp λ. Seen on the Fig. are a single parabola and two families of straight lines. The parabola is the plot of $E = 0.87 (F\lambda)^2/\varepsilon_{ph}$, for $F = 10^6$ V/cm. and $\varepsilon_{ph} = 0.1$ ev; the straight lines are plots of the relations $\lambda = \lambda_o + \alpha(E/\varepsilon_{ph})$ with $\varepsilon_{ph} = 0.1$ ev. This is a particularly simple form of energy-dependence of the mfp, chosen for convenience. The parabola is the empirical relationship between the emerging, steady-state average energy $E_{ave,ss}$ and the constant (energy-independent) mfp λ, assuming isotropic scattering, previously discussed in the First Semiannual Report. The two families of straight lines correspond to $\lambda_o = 25$ Å and $\lambda_o = 40$ Å respectively. The members of each family correspond to different values of α: $\alpha = 0.5$, 0.8, 0.9, 1.0, 1.1, 1.2 and 2.0 for the '$\lambda_o = 25$ Å' family, and $\alpha = 0.5$ and 0.8 for the '$\lambda_o = 40$ Å' family. The nature of the runaway has to do with the presence or absence of intersections of the straight lines with the parabola. In the absence of intersections (the $\alpha = 2.0$ line for $\lambda_o = 25$ Å and the $\alpha = 0.8$ line for $\lambda_o = 40$ Å) there is strong runaway, as seen in the $\alpha = 1.0$ curves, for $\lambda_o = 40$ Å, in Fig. 46, and the $\alpha = 2.0$ curves in Figs. 47 and 48 (as well as in Fig. 41 of the First Semiannual Report). For the case that there are two intersections of the straight lines with the parabolas the situation had not been resolved at the time of writing of the First Semiannual Report, the available results for this situation being summarized in Fig. 39 of that Report. A more extensive study of this situation has led to a considerable understanding which we now discuss.

First consider the two $\alpha = 0.5$ curves in Fig. 46. From Fig. 45 this is clearly a case with two widely separated intersections. Yet it is clearly seen in Fig. 46 that the two $\alpha = 0.5$ curves in Fig. 46 do not converge to the same horizontal asymptote, that, in fact, the curve for $E_o = 10.0$ ev actually

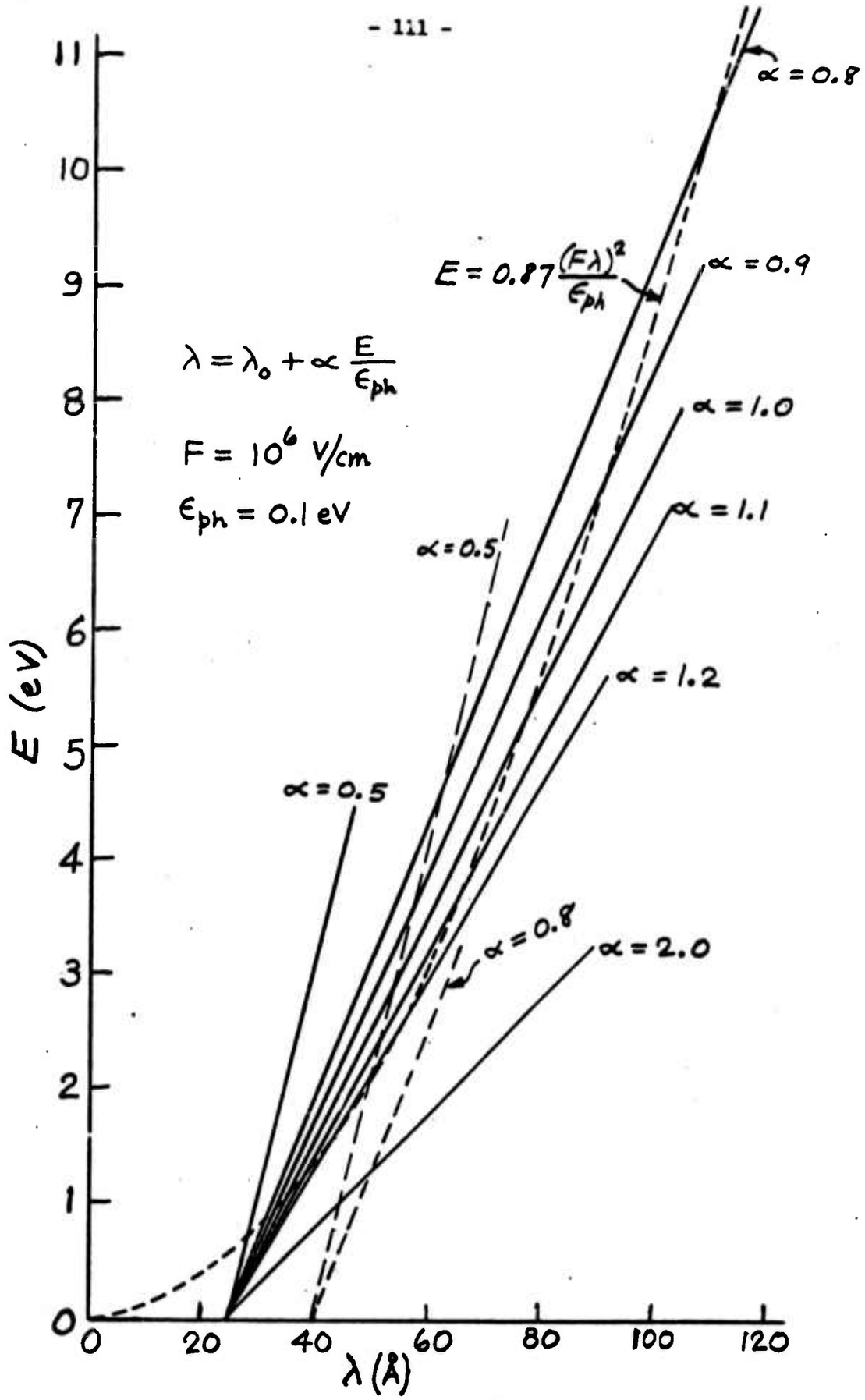

Fig. 45. Graphical Analysis for Runaway Electrons

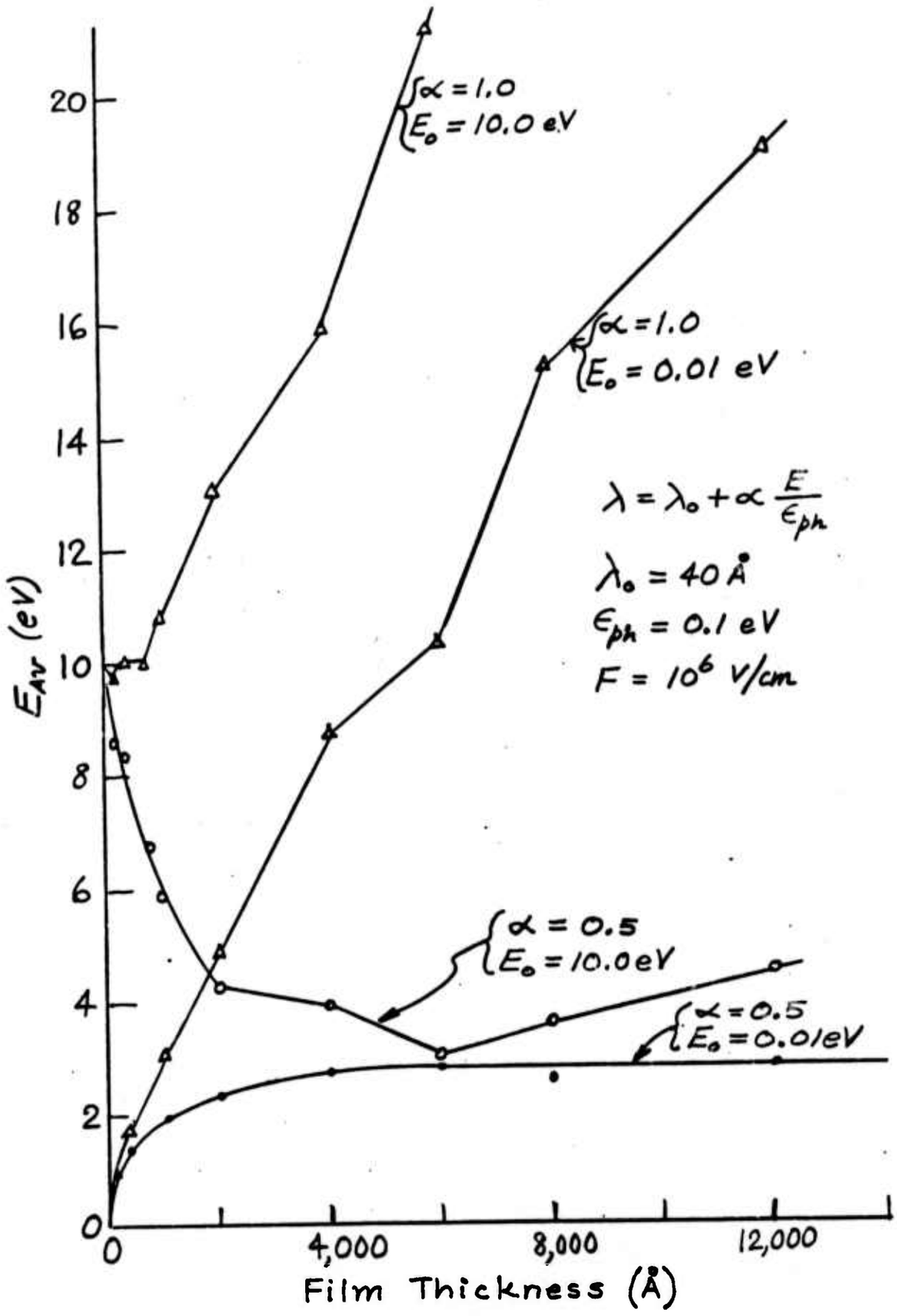

Fig. 46. Average Energy vs. Film Thickness (k)

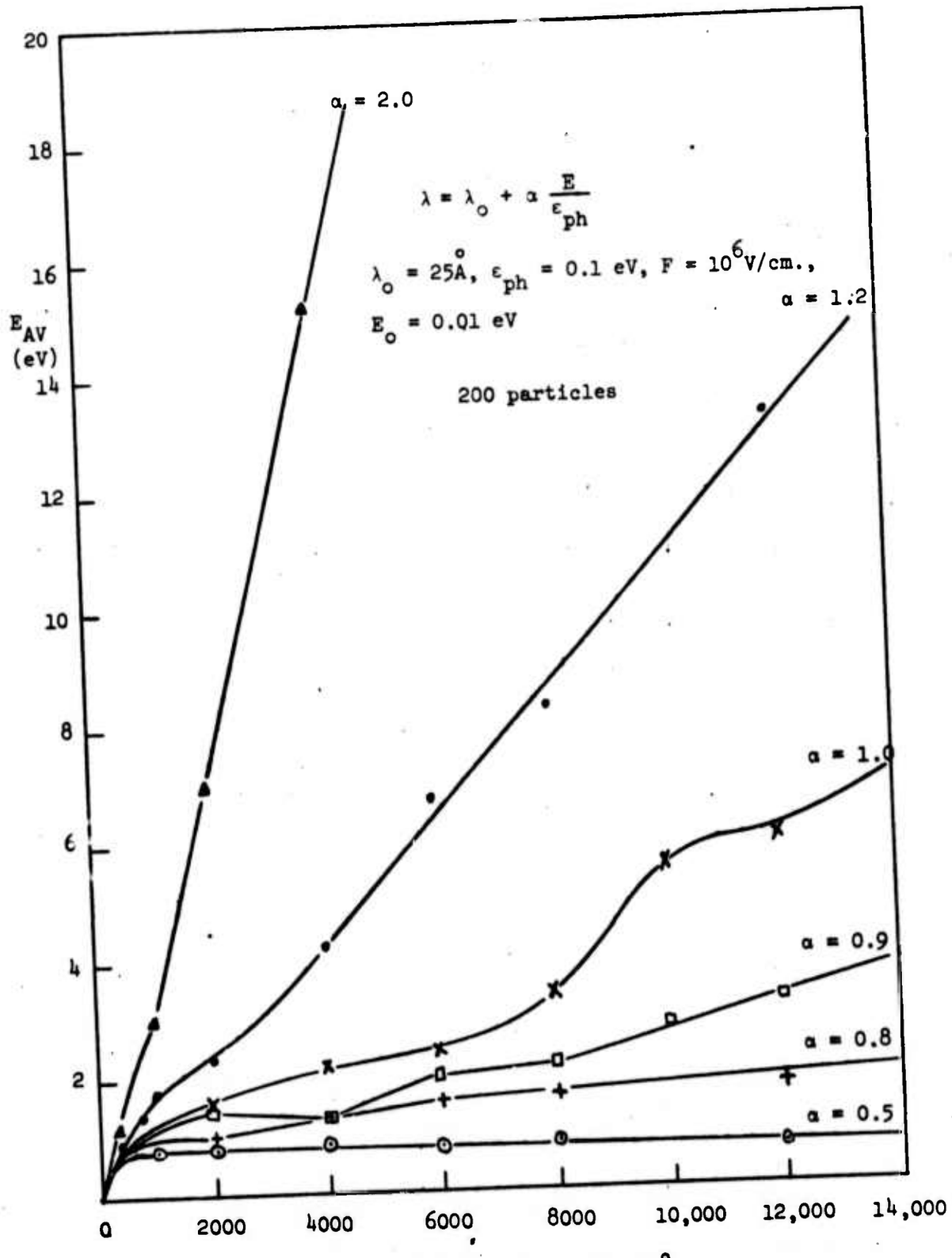

Fig. 47. Average Energy vs. Film Thickness (Å)

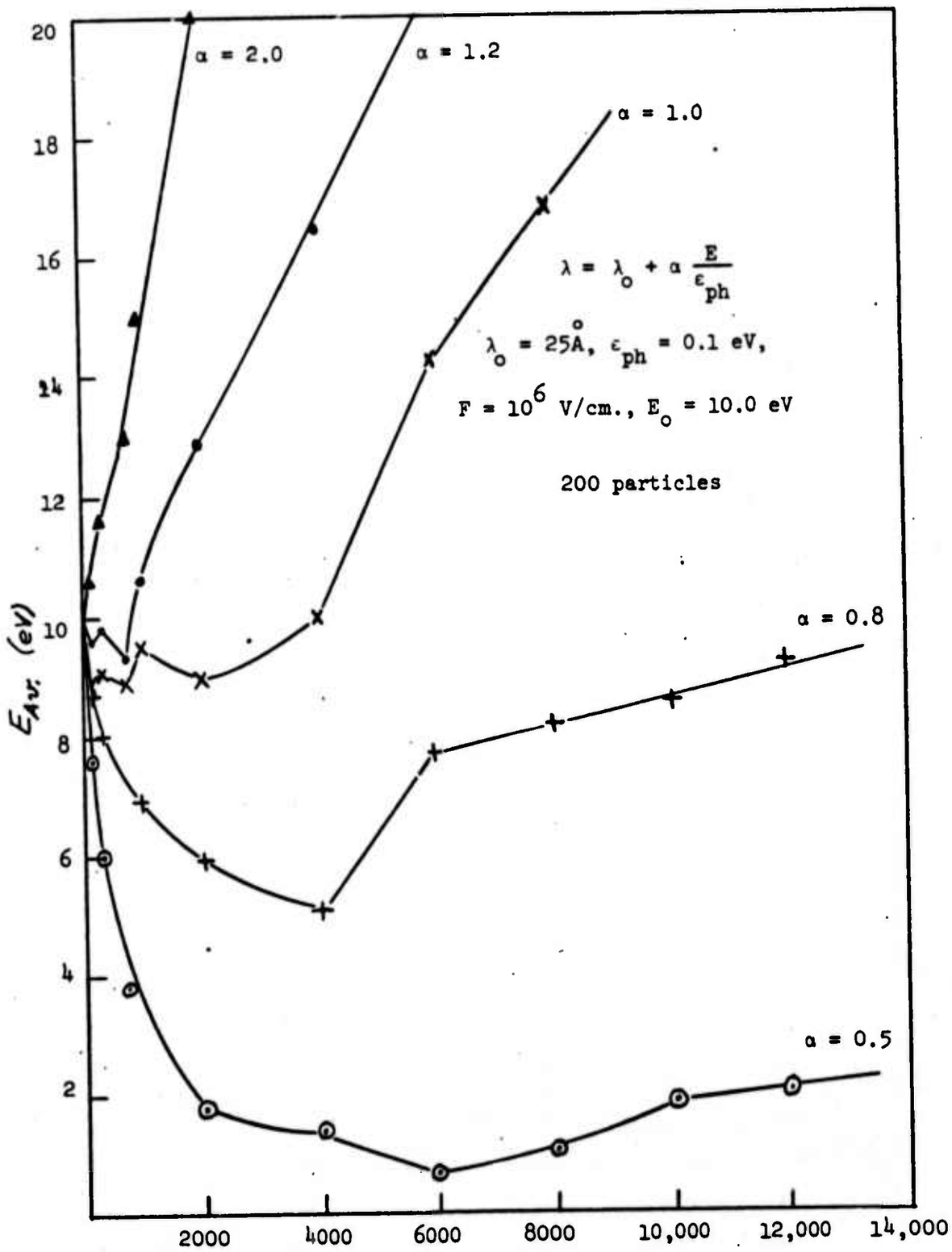

Fig. 48. Average Energy vs. Film Thickness (Å)

slowly diverges at large film thicknesses. The reason for this interesting behavior is that for a batch of particles entering at the energy E_o = 10.0 ev, a few 'escape' from the well-behaved part of the distribution. (These few 'escaped' electrons are very much like Shockley's 'lucky' electrons). A particle, once escaped to sufficiently high energy (which is just the second, higher intersection point in Fig. 45) is almost certain to continue gaining energy monotonically. A single such particle, in a finite batch of particles, is enough to push the average energy into divergence as the film thickness is taken larger and larger. The curve for α = 0.5 and E_o = 0.01 ev has not a single escaped electron in the batch of 200 particles, hence the convergence of a well-defined value of $E_{ave,ss}$. The one or two escaped particles in the α = 0.5, E_o = 10.0 ev run cause the slow divergence. Clearly the non-escaped particles are behaving 'properly', i.e. converging as expected (e.g., the point at t = 6000Å). Going to Fig. 47, we see that even for E_o = 0.01 ev, for α as low as 0.8 there are escaped particles, even though there are two well-separated intersections of the parabola by the α = 0.8, λ_o = 25Å straight line in Fig. 45. For λ_o = 25Å and E_o = 10.0 ev we see from Fig. 48 that there are escaped particles for all values of α studied, namely down to α = 0.5. Finally, in Fig. 49 we compare the divergence of the α = 0.9, λ_o = 25Å curves for E_o = 0.01 ev and E_o = 4.0 ev.

The problem of 'escaping' electrons is examined more closely in a Technical Report which will be issued in the coming months. In particular, the actual histograms of emerging particle energies will be presented in this Report. These histograms confirm in detail the 'escaping' electron picture implied by the E_{ave} vs t (film thickness) curves discussed above.

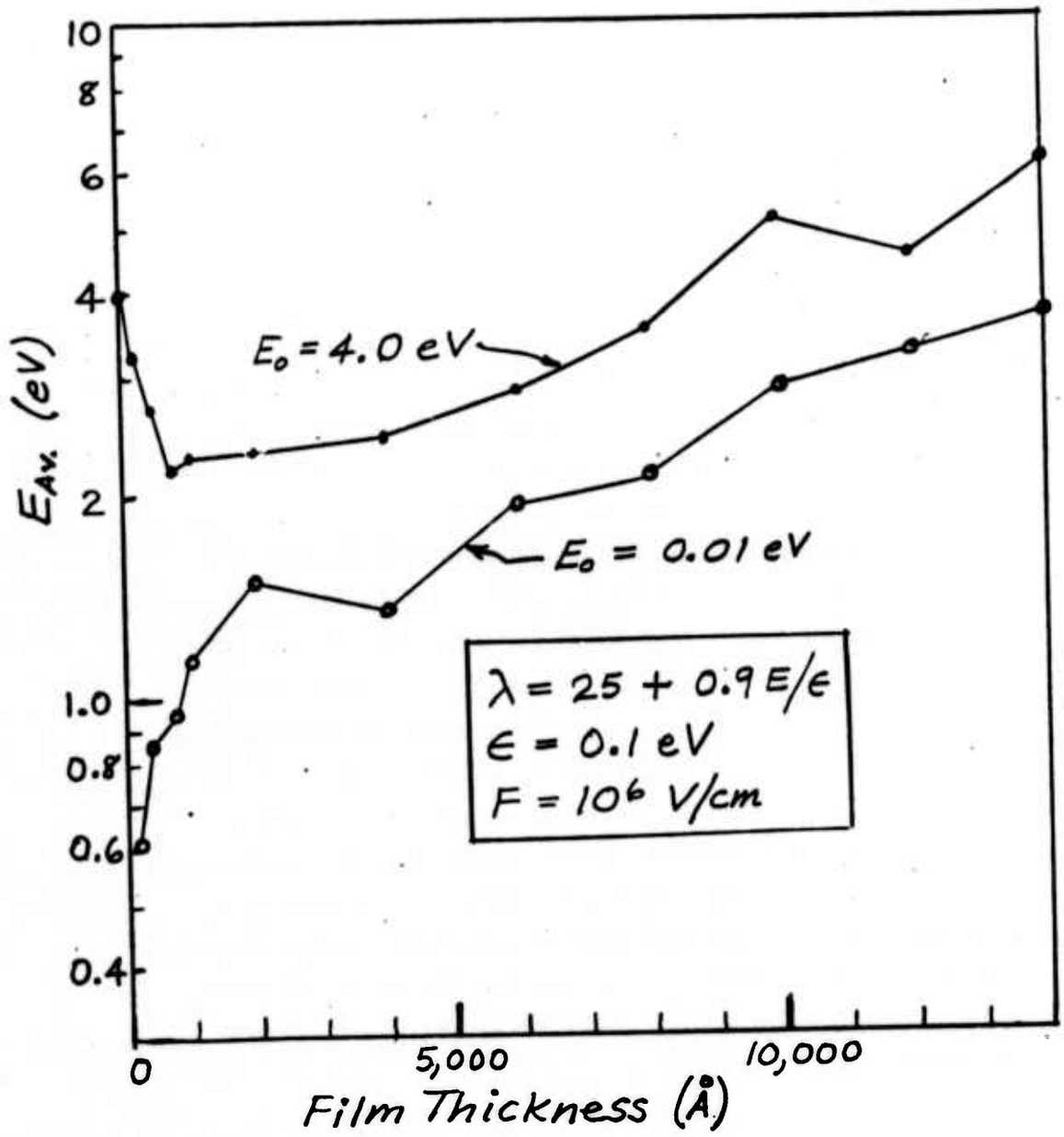

Fig. 49. Average Energy vs. Film Thickness (Divergent Case)

9. Theoretical Modeling of Local Breakdown (B. Ridley collaborating)

A model for electrical breakdown in SiO_2 films has been constructed along the following lines, illustrated schematically:

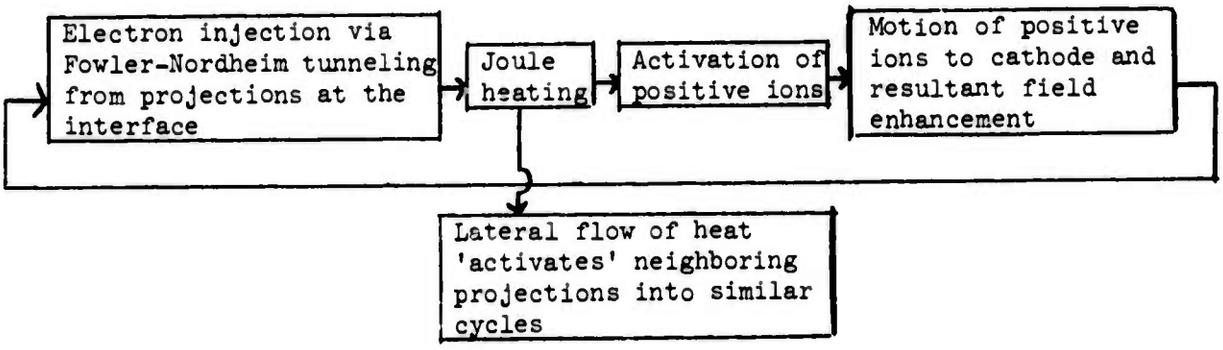

The model assumes that there are irregularities at the cathode interface which produce a geometric enhancement of the field at the irregularity. Fowler-Nordheim tunneling of electrons into the oxide at the irregularity produces a locally high current density which produces strong joulean heating. Positive ions bound in the oxide volume are thermally released and drift, in very high field, to the irregularity. The pile-up of positive ionic charge further enhances the field at the irregularity, yielding a positive feedback cycle and a thermal runaway. The lateral flow of heat activates neighboring projections into comparable positive-feedback cycles. In SiO_2 the postulated ions are very likely Na^+. The required total sheet densities of Na^+ are on the order of 10^{12} to $10^{13}/cm^2$ and are somewhat dependent on details of the model. Such densities appear reasonable, based on the recent work of Kuhn and Silversmith.[28]

The details of the above model, based on a considerable amount of work, will be presented in a Technical Report. Here we present just a single Figure, namely a comparison of the prediction of the theory for the breakdown field dependence on film thickness, $\mathcal{E}_B$ vs d, with the experimental results of Osborn and Ormond[29], Fig. 50.

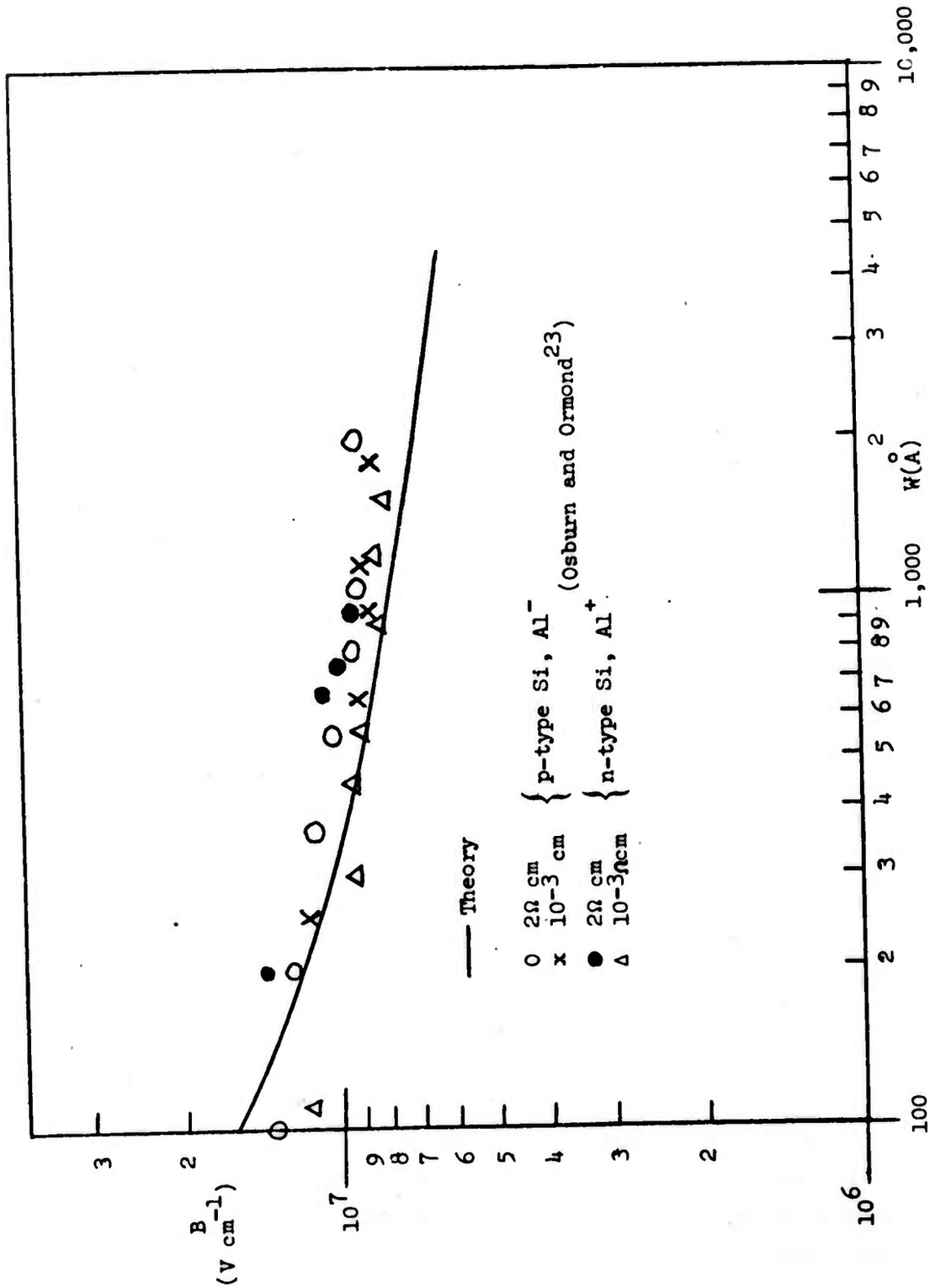

Fig. 50. Dependence of Breakdown Field on Film Thickness (Al-SiO_2-Si Structure)

References

1. D. V. McCaughan and V. T. Murphy, J. Appl. Phys. 44, 2008 (1973).
2. (a) R. Williams and A. Willis, J. Appl. Phys. 39, 3731 (1968). (b) R. Williams and M. H. Woods, J. Appl. Phys. 44, 1026 (1973).
3. M. M. Shahin, Photogr. Sci and Eng 15, 322 (1971).
4. N. Gordon and W. C. Johnson, IEEE Tr. Electron Dev. ED-20, 253 (1973).
5. J. E. Carnes and M. T. Duffy, Jour. Appl. Phys. 42, 4350 (1971).
6. This Fig. is taken from the Final Report under Contract N00019-70-C-0129, prepared by the RCA Laboratories, Princeton, N.J. for the Naval Air Systems Command (Fig. 38, p. 41).
7. R. H. Good Jr. and E. W. Müller, Hdbk. d. Phys. XXI, 176 (Springer-Verlag, Berlin 1956).
8. R. Williams and M. H. Woods, J. Appl. Phys. 44, 1026 (1973).
9. M. Lenzlinger and E. H. Snow, J. Appl. Phys. 40, 278 (1969).
10. F. Stern, Phys. Rev. B 5, 4891 (1972).
11. N. Klein, IEEE Trans. Electron Dev., ED-13, 788 (1966).
12. H. L. Hughes, R. D. Baxter, and B. Phillips, IEEE Trans. Nuc. Sci., NS-19, 256 (1972).
13. C. N. Berglund and R. J. Powell, J. Appl. Phys. 42, 573 (1971).
14. R. Williams, Phys. Rev. 140, A569 (1965).
15. J. H. Thomas and F. J. Feigl, J. Phys. Chem. Solids, 33, 2197 (1972).
16. P. V. Gray and D. M. Brown, Appl. Phys. Lett. 8, 31 (1966).
17. A. Goetzberger and E. H. Nicollian, Bell Syst. Tech. J. 46, 513 (1967).
18. J. Grosvalet and C. Jund, IEEE Trans. Electron Dev., ED-14, 777 (1967).
19. R. J. Powell and C. N. Berglund, J. Appl. Phys. 42, 4390 (1971).
20. C. N. Berglund, IEEE Trans. Electron Dev., ED-13, 701 (1966).
21. D. R. Kerr, Paper 108 presented at the meeting of the Electrochem. Soc., 1969 May 4-9, NYC, NY.
22. M. Kuhn, Sol. St. Electr. 13, 873 (1970).
23. A. J. Speth and F. F. Fang, Appl. Phys. Lett. 7, 145 (1965).
24. M. Simons, L. K. Monteith and J. R. Hauser, IEEE Trans. Electron Devices, ED-15, 966 (1968).

25. A. G. Stanley and H. C. Pao, paper presented at the Second Semiconductor Interface Specialists Conference, Las Vegas, Nevada, Mar. 1-3, 1967.

26. C. B. Duke, Tunneling in Solids, (Supplement to Solid State Physics 10), (Academic Press, N.Y. 1969), p. 25.

27. Handbook of Mathematical Functions, p. 446 (National Bureau of Standards, Applied Mathematics Series, No. 55, June 1964).

28. M. Kuhn and D. J. Silversmith, J. Electrochem. Soc. 118, 966 (1971).

29. E. M. Osburn and D. Ormond, J. Electrochem. Soc. 119 (1972).